Dynamic buckling instabilities in fluids and solids

Ousmane Kodio
Lincoln College
University of Oxford

A thesis submitted for the degree of
Doctor of Philosophy

Trinity 2019

Contents

Preface

The research described in this thesis was performed in the Mathematical Institute at the University of Oxford between January 2016 and July 2019, and was supervised by Prof. Dominic Vella and Dr Ian Griffiths.

The results presented in this thesis are believed to be original, except those of the introduction chapter §1, which constitutes a review of the literature, and elsewhere where explicit reference is made to the work of others. No part of the thesis has been submitted previously for a degree of the University or elsewhere.

Parts of the thesis discuss experiments performed by others: in particular the images of fig. 3.1 and the experimental data points of fig. 3.6 are due to Finn Box, and taken from Box *et al.* (2020). Similarly the images of fig. 4.1 are taken from a previously published paper of Vandeparre *et al.* (2010) while the experimental data points of fig. 4.11 were provided to us by Pascal Damman (University of Mons) from their previously published paper (Vandeparre *et al.*, 2010).

Some of the results of this thesis have been published or are under consideration for publication:

• O. Kodio, I. M. Griffiths and D. Vella 'Lubricated wrinkles: imposed constraints affect the dynamics of wrinkle coarsening' Physical Review Fluids 2, 014202 (2017). This corresponds to chapter 4.

• O. Kodio, A. Goriely and D. Vella 'Dynamic buckling of an inextensible elastic ring: Linear and nonlinear analyses' Physical Review E 101, 053002 (2020).
This corresponds to chapter 3.

• F. Box, O. Kodio, D. O'Kiely, V. Cantelli, A. Goriely and D. Vella 'Dynamic buckling of elastic rings in a soap film' Physical Review Letters 124, 198003 (2020). This corresponds to chapter 3.

Acknowledgements

I would like to thank very much my supervisor Dominic Vella for his invaluable guidance, and support. Dominic is a fantastic supervisor and I will always be in admiration for his acuity of writing. I also would like to thank very much my co-supervisor Ian Griffiths for his support and for reading and proof-reading this manuscript.

Je souhaite remercier du fond du coeur mon mentor Alain Goriely qui m'a tant appris pendant ces années de thèse. Merci pour sa generosité, son soutien, et de m'avoir aiguiller sur tant de sujets: elasticité, bifurcation, analyse multi-echelle, auto07p, chiralité de l'espace, juggling, ..., ce fut un privilège de rencontrer un homme de science et de culture. Merci d'avoir faciliter mon épanouissement. En Bambara, il ya un proverbe qui dit, qu'on ne peut pas semer un esprit (comme une graine) mais qu'il est surement possible de l'arroser. Donc merci d'avoir arroser le mien pendant ces trois dernières années.

I only met with Peter Howell three times during my DPhil but those three meetings had so much impact on my thesis. I am grateful for his generosity and expertise. For example, the problems studied in the second and third chapter were sparked during discussions with Peter.

I was fortunate to collaborate with such a great experimentalist that is Finn Box! Thanks for all those times you've proven my predictions wrong ;-) also thanks for the pilgrimage at the Old Trafford in Manchester!

I also would like to thank my office-mates for all the good time: Armin Krupp, Tom Chandler and Christian Goodbrake.

A special thank to Doireann O'Kiely (for all the help and support and for being a terrific running-mate), to Matteo Taffetani (for all the discussions in elasticity), to Tom Mullin (for all the discussions in fluids mechanics), to Derek Moulton (for being my alter ego at table-football), to Nick Trefethen (for the help/tips in numerics and a dedicated copy of his Exploring ODEs), to Andrew Krause and Nicolas Boulle (for all the interesting discussions about numerics).

My last thanks go to the European Union (E.U.) for the financial support without which this thesis would not have been completed.

Abstract: Many natural phenomena encountered in nature may be understood through the paradigm of buckling instability. Examples include the design of columns in structural engineering, the folding of geological formations, the collapse of blood vessels, and the fragmentation of uncooked spaghetti, to name only a few. The phenomenon of buckling has traditionally been seen only as a nuisance, but more recently it has also proven useful as a potential tool for pattern formation, particularly at small scales. Many studies have focused on the features of static buckling, particularly pattern formation.

This thesis focuses on how dynamic buckling affects the spontaneous selection of patterns in a number of canonical problems.

We first study the effect of curvature on dynamic buckling in circular geometries. We study the pattern observed when a ring made of either a viscous liquid or an elastic solid is subject to a suddenly applied external pressure. We develop numerical schemes to study the evolution of the ring's profile and compare those results to linear stability analysis. A weakly nonlinear analysis is performed to understand the behaviour of the observed shape beyond the onset of instability, with results that compare well with both numerical and experimental work.

In the late stages of instabilities, buckles merge — the wrinkle pattern coarsens. To understand this coarsening we consider the non inertial problem of a beam sitting on a viscous layer. We explain how wrinkle coarsening occurs as the result of wave dispersion and quantify coarsening by presenting an asymptotic analysis of the governing equation. We also study the effect of confinement and show that it has a crucial effect on coarsening at late times. We develop an analytical expression for the effect of confinement, which allows us to better explain previously published experimental data. Finally, our numerical solution reveals a new regime as the wavelength of wrinkles become comparable to the size of the system. In this regime the dynamics is relatively slow with the system remaining for long periods with one particular mode before rapidly switching to another. We study this regime, the so-called *temporal cascade*, in detail.

The problems we are considering have different geometries and different material constitutive relations, but highlight a number of common themes. Mathematically, those systems are described by a Partial Differential Equation with a global constraint whose numerical solution is found by framing it in the language of Differential Algebraic Equations.

Chapter 1

Introduction

1.1 Buckling

Columns have been used in architecture since antiquity. For example, the Temple of Amon in Karnak, Egypt, built under the reign of the pharaoh Seti I around 1300 BC, has columns up to 69 feet tall (Gauthier, 1969). The purpose of such columns is to support the load of other parts of a building. However, it is well known that a beam's ability to support a load is sensitive to its thickness: a beam of a very small thickness may exhibit an instability when subjected to a sufficiently large compressive load. Consider an initially straight beam that is compressed by applying a force at its two ends. When the applied force is small enough, the beam can withstand the compression and remains straight. However, if the compression reaches a threshold, then the beam bends. This is called a **buckling instability**. After the *buckling* happens, the beam is no longer a useful strengthening tool: the load required to bring the two ends of the beam closer decreases dramatically. The phenomena of bending and buckling have a long history and their early descriptions seem to date back to Leonardo da Vinci (see fig 1.1).

The question of finding the shape of the bent beam and the threshold force at which buckling occurs, was a challenge first solved by Euler in 1744 using the calculus of variations, in the appendix of his book on elastic curves (*curva elastica* hence the shortened name **elastica**; Euler, 1744). An equivalent treatment is possible using the standard Newtonian laws of mechanics, where balancing forces and torques on a rod, treated as a curvilinear continuum medium, results in Kirchhoff's equations (Goriely, 2017; Love, 1959).

Buckling of thin structures is still an active area of research: Much current research thrives to utilize buckling phenomena to provide functions to structures in engineering (Reis, 2015), or in shape recognition for computer vision (Mumford, 1994). Perhaps

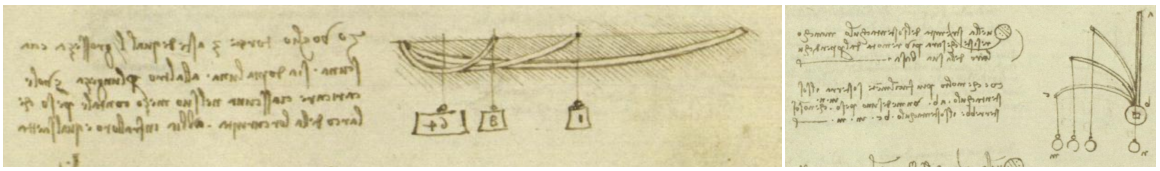

Figure 1.1: Drawings of Leonardo da Vinci related to *bending* and *buckling*. Left: an illustration of the relation between the deflection, the applied load, and the length of the beam: This shows that by halving the length and then halving again, the same beam can withstand loads $8 = 2^3$ and $64 = 4^3$ larger with the same deflection. (Note that annotations are in Leonardo's famous mirror writing). Right: weights hung on a vertical beam induce *buckling* of the beam. (Images captured from the Madrid Codices.)

the more important aspect to note here is that the mathematics developed since the early work on elastica are being used as a paradigm to study a wide variety of problems, which are described by the same underlying equations (Roman *et al.*, 2004): shape of drops, shape of leaves and tendrils, dynamic of a pendulum, sine-Gordon equation.

A classic treatment of buckling will be a useful reference point throughout the thesis and so we now give a description of this standard picture. Consider an elastic beam of length L, pinned at its two ends, and initially flat. The beam is compressed at its two ends by the application of a force P. A material point on the beam is parametrized by its arc-length, $s \in [0, L]$, and its position is denoted by $\boldsymbol{r} = (x(s), y(s), 0)$. We choose the end $s = 0$ of the beam to be the origin of the co-ordinates. The arc-length parametrization ensures that $\mathrm{d}x = \mathrm{d}s \cos\theta$, and $\mathrm{d}y = \mathrm{d}s \sin\theta$, where $\theta(s)$ denotes the angle between the abscissa and the tangent to the curve at the point of arc-length s, drawn in the sense of increasing arc-length (Love, 1959). We denote by κ the curvature of the curve at the point with arc-length s, *i.e.* $\kappa = \frac{\mathrm{d}\theta}{\mathrm{d}s} = \theta'(s)$.

The equations of equilibrium are given by the balance of forces and torque as (Goriely, 2017; Love, 1959):

$$\frac{\mathrm{d}\boldsymbol{F}}{\mathrm{d}s} = 0, \tag{1.1}$$

$$\frac{\mathrm{d}\boldsymbol{M}}{\mathrm{d}s} + \frac{\mathrm{d}\boldsymbol{r}}{\mathrm{d}s} \times \boldsymbol{F} = \boldsymbol{0}, \tag{1.2}$$

where $\boldsymbol{F}$ and $\boldsymbol{M} = M\boldsymbol{e}_3$ are the internal forces and moments at a point of arc-length s.

In order to close the equations of equilibrium, we need a constitutive relation that describes how the internal stresses are related to the deformations. For the bending of

an elastic beam, the usual constitutive assumption is a linear proportionality between the moment and curvature, *i.e.*

$$M = B\kappa, \tag{1.3}$$

where B is a constant known as the bending stiffness, $B = Eh_{\mathrm{T}}^3/12$, where E is the Young modulus of the material that it is made from, and h_{T} is the thickness. The constitutive relation is what embodies the properties of the material being studied. Therefore materials that are different from a linear elastic will possess a different constitutive relation.

Using $\boldsymbol{F}(L) = (-P, 0, 0)$, and the pinned boundary conditions, $\kappa(0) = \kappa(L) = 0$, the equilibrium equations (1.1)-(1.2) yield:

$$B\frac{\mathrm{d}^2\theta}{\mathrm{d}s^2} = -P\sin\theta, \tag{1.4}$$

subject to:

$$\frac{\mathrm{d}\theta}{\mathrm{d}s}(0) = \frac{\mathrm{d}\theta}{\mathrm{d}s}(L) = 0. \tag{1.5}$$

Equation (1.4) is a nonlinear eigenvalue problem for θ: Clearly $\theta = 0$ is one of the solutions but for certain values of P, non-trivial solutions may exist. The solution of this eigenvalue problem gives both the critical load, via the value of P, and the shape of the so-called elastic curves as the eigenfunctions. Equation (1.4) may be solved exactly using the elliptic functions of Jacobi (Love, 1959). However, as we shall see, it is possible to gain some insights into the buckling phenomena by assuming that the angle of deflection is small, $\theta \ll 1$.

For small angles, the boundary value problem (1.4) can be simplified by assuming that $\sin(\theta) \approx \theta$. Noting further that for small angles, $s \approx x$, with x the horizontal scale, there is a family of non-trivial solutions $\theta_n = A\cos(\frac{n\pi x}{L})$, where n is a natural number. Such solutions hold only when the compressive load $P = P_n = n^2\pi^2 B/L^2$ allowing us to determine the smallest applied force for which a buckled solution exists, the so-called Euler buckling load, $P_c = P_1 = \pi^2 B/L^2$. Euler buckling loads with different applied boundary conditions may be obtained readily in the same manner. While the details of the boundary conditions may lead to different buckling loads, the dimensionless quantity PL^2/B is always an $\mathcal{O}(1)$ quantity — beams buckle with smaller forces as they get longer or thinner, as should be expected. Crucially, calculation of this buckling load allow structures to be built to withstand the expected loads. While the above calculation reveals the buckling load and the shape of the buckled mode, the amplitude, A, remains an indeterminate quantity, which cannot

be resolved by this linearized theory — any amplitude, A, will do. To resolve this issue it is sufficient to extend the approximation of the sine to next order, *i.e.* for $P/P_c - 1 \ll 1$, $\sin\theta \approx \theta - \frac{1}{6}\theta^3$. A weakly non-linear analysis leads to a relation between the amplitude, A, and the compressive force P in the vicinity of buckling as (Gauthier, 1969, p.16),

$$\frac{A}{L} = \begin{cases} 0 & \text{if } P < P_c, \\ \frac{2}{\pi}\sqrt{8\left(\frac{P}{P_c} - 1\right)} & \text{if } P > P_c. \end{cases} \tag{1.6}$$

As we may noticed in (1.6) when $P > P_c$, the amplitude varies non-linearly with the compressive force P. This non-linear relationship between the cause and the effect is a signature that buckling is a non-linear phenomenon.

The dependence of amplitude on loading in (1.6) holds only when the compressive force is close to the buckling threshold. This is useful to, for example, calculate whether a structure might fracture or deform plastically if something goes wrong and it is exposed to a load that is slightly higher than the designed safety threshold.

In other settings, however, a structure may suddenly be exposed to loads $P \gg P_c$, as for example caused by an impact or explosion. One possible resolution to this problem might be to note that a given load P is the critical buckling load for the n^{th} buckling mode with $n \sim (PL^2/B)^{1/2}$, and so one might expect a length scale $\lambda = L/n \sim (B/P)^{1/2}$ to emerge.

While elements of this expectation are correct, the buckling process that leads to it, is invariably dynamic. We therefore turn from static to dynamic buckling.

1.2 Dynamic buckling

In contrast to static buckling, in **dynamic buckling** there is a time dependence in the problem, which can either come from a time-dependent compressive force or from the addition of an acceleration term. Historically, the study of dynamic buckling has focused on determining the conditions under which structures fail plastically (Karagiozova and Alves, 2008; Lindberg, 2003). A popular illustration of dynamic buckling is the fragmentation of dry spaghetti. An example of such studies is experiments upon impact by Gladden *et al.* (2005) who impacted a weight on dry spaghetti. This led first to dynamic buckling and then fracture as shown in an illustration from their work reproduced in fig 1.2.

However, in this setup the details of impact complicate the calculation of the compressive force. Firstly, the impacting weight leads to non-uniform tension. Secondly,

given the brittle nature of uncooked pasta, fracture occurred soon after the onset of instability, meaning that the development of the instability itself cannot be followed and understood. To bypass these limitations, we will be studying (in the third chapter) dynamic buckling of a pressurized elastic hoop. This will allows us to understand the emergence of wavelength in the dynamic buckling.

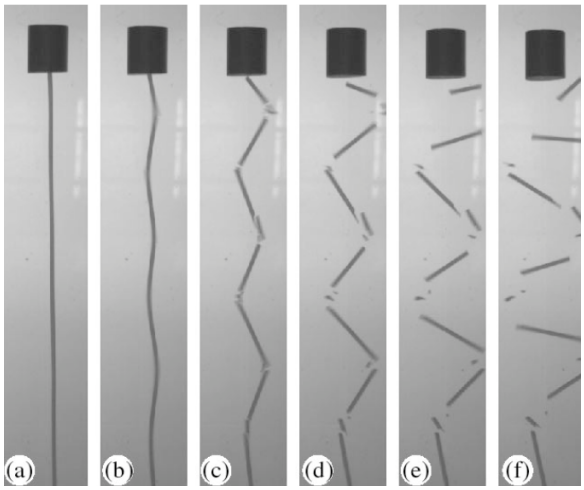

Figure 1.2: Dynamic buckling: Demonstration of emergence of new length scale which is different from the length scale of the beam. However in this setup it is really not clear how the compressive force is controlled in time. Reprinted figure with permission from [J. R. Gladden, N. Z. Handzy, A. Belmonte, and E. Villermaux, *Physical Review Letters*, 94, 035503 (2005).] DOI: `https://doi.org/10.1103/PhysRevLett.94.035503`. Copyright 2005 by the Americal Physical Society.

1.3 Viscous buckling

The buckling of an elastic beam is a geometrical manifestation characterizing the response of the beam to the compression that is applied on it. This begs the question whether other substances might exhibit buckling — the most obvious being liquids.

The basic difference between liquids and solids is that liquids cannot withstand shearing whereas solids can. On the face of it, this would seem to preclude the possibility that liquids can buckle — buckling requires anisotropic stresses that a liquid cannot sustain in equilibrium. But this distinction is very narrow: "when enough time is given to a viscous fluid then a small force can produce a great effect" (see Maxwell, 1899), also discussed in Teichman (2002, p.18). However, the converse of Maxwell's idea is that if you strike a viscous liquid quick enough, it may behave like a solid.

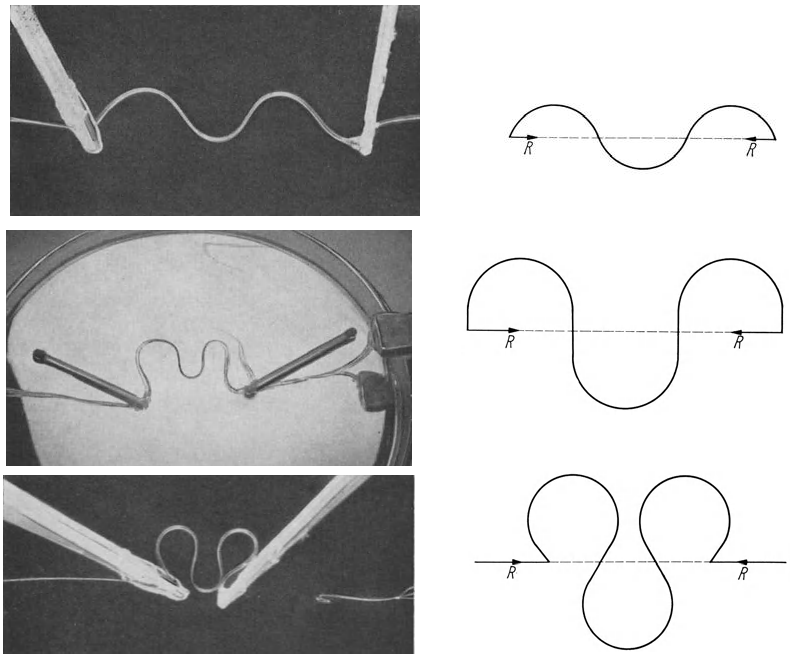

Fig. 12. Threads of SAIB floating on mercury compared with Love's calculated elasticas.

Figure 1.3: Left: the shape of a highly compressed liquid thread observed by Taylor (1969). Right: the shape of the elastica as computed by Love (1959). This shows the striking analogy in morphology between a buckled viscous liquid thread and an elastic beam. Reprinted by permission from Springer Nature Customer Service Centre GmbH: Springer-Verlag. Applied Mechanics, *Proceedings of the Twelfth International Congress of Applied Mechanics*. 'Instability of jets, threads, and sheets of viscous fluid', G. I. Taylor (1969). DOI: `https://doi.org/10.1007/978-3-642-85640-2_30`. ©Springer-Verlag Berlin Heidelberg 1969.

For a given geometry there is an intrinsic characteristic time scale of buckling of a liquid, τ; when τ is larger than the time scale of compression, buckling may be observed. The existence of this time scale has been studied experimentally by Le Merrer *et al.* (2012) for a liquid filament of viscosity μ, diameter D, and whose ends are compressed at a velocity U. The characteristic time scale of buckling discussed above is found by Le Merrer *et al.* (2012) as $\tau = D^2/LU$; comparing τ with the time scale of their experiment, shows that only slender filaments are susceptible to buckling. The '*susceptibility*' of a given filament to buckle thus depends on the ratio of the diameter to the length of the filament, D/L.

The phenomenon of viscous buckling was first establish experimentally by Taylor (1969) who reported the striking similarities between the buckling of an elastic beam and the buckling of a highly viscous liquid thread (Taylor, 1969). This close similarity

between the buckled shape of a highly viscous liquid and the buckled shape of an elastic beam is reproduced from Taylor (1969), in fig. 1.3.

The buckling of thin viscous thread has been investigated theoretically by Buckmaster *et al.* (1975) who first derived the governing equations describing the shape of a thin viscous thread, which they termed the *viscida*. Buckmaster *et al.* (1975) establish the governing equations by performing a dimensional reduction of the Stokes equations for a thin liquid thread, expressed in curvilinear co-ordinates. Their work tries to account for the experimental work derived by Taylor (1969). A more systematic approach, to obtain the governing equations including the effect of inertia was performed by Howell (1994) and O'Kiely (2017). In the absence of inertia, the equations describing the shape of a viscous ring in a circular geometry, was derived by Griffiths (2007), Griffiths and Howell (2009) and Howell (1994), based on the asymptotic expansion of the Stokes equations.

The main result from Buckmaster *et al.* (1975) is that the analogue of the constitutive relation (1.3) is that the moment, M, is proportional to the temporal derivative of the curvature, *i.e.*

$$M = B\frac{\partial \kappa}{\partial t}, \tag{1.7}$$

where now $B = \mu h_{\mathrm{T}}^3/12$, with μ the viscosity of liquid and h_{T} the thickness of the thread. With this constitutive relation, the arguments that lead to the elastica equation may be followed through. This establishes the link between elastic and viscous buckling. Many recent experiments in fluid systems with no apparent elasticity are reminiscent of elastic buckling (O'Kiely, 2017; Slim *et al.*, 2012). For example, when a viscous bubble is emptied very quickly, it is observed that the surface of the bubble exhibits some undulations reminiscent of elastic instabilities (see fig. 1.4). A similar undulation in circular geometry is observed in the splash jets formed during the water entry of a sphere (see Marston *et al.*, 2015, 2016, and fig. 1.3). As described by Marston *et al.* (2015): *"The crown wall collapses inward due to the pressure differential across the wall created by the moving air in the wake of the sphere and surface tension within the crown"*.

We shall see in this thesis that these systems pose questions about the analogue elastic systems already described. We therefore return now to describe some more complex examples of pattern formation in purely elastic systems.

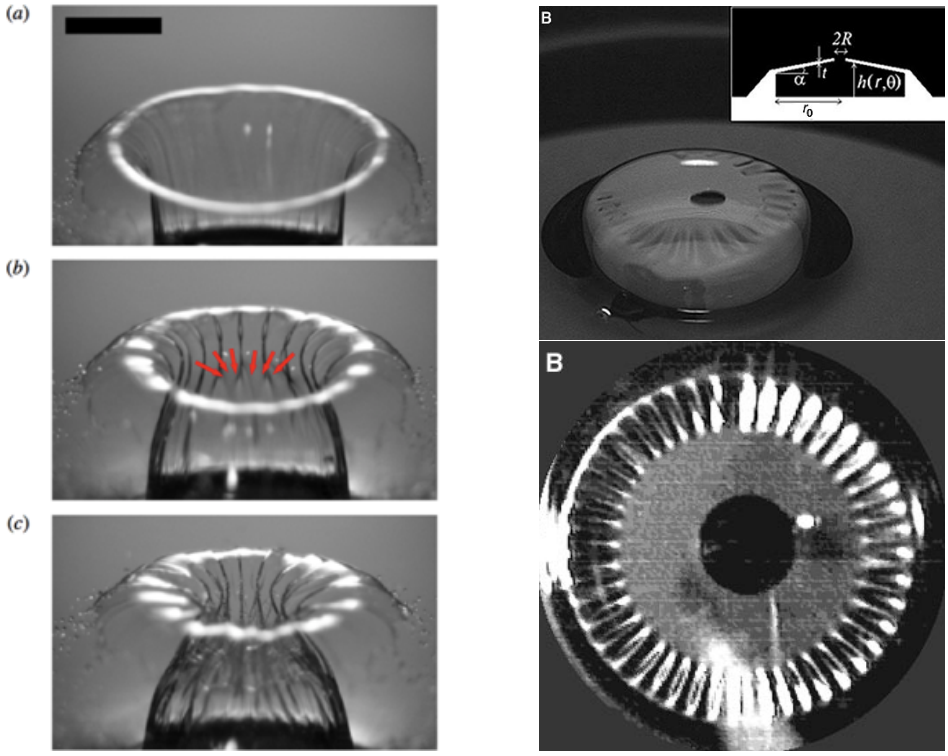

Figure 1.4: Left: Buckling of a splash jet (or crown) formed during water entry of spheres. Reprinted from Marston *et al.* (2016). ©2016 Cambridge University Press. Right: Rippling instability of a collapsing bubble. Fom R. da Silveira, S. Chaieb and L. Mahadevan (2000). 'Rippling Instability of a Collapsing Bubble'. *Science* 287. DOI: 10.1126/science.287.5457.1468. Copyright ©2000, The American Association for the Advancement of Science.

1.4 Pattern formation via buckling

Our primary motivation for studying buckling in liquids or solids is to understand the striking pattern formation. Indeed, patterns formed in dynamic buckling are reminiscent of wrinkle patterns in static scenarios. An illustration of these similarities is shown in fig 1.5: On the left is shown a picture of a beach ball that is poked, in which wrinkles appear. On the right of fig 1.5, is shown an archetypical example of dynamical buckling where an annulus is collapsing under an inbalance of surface tension. Note the similarities between the images of fig 1.5. This is an illustration that patterns formed in dynamic buckling are reminiscent of wrinkle patterns.

The current study of buckling falls into the dichotomy: 'buckliphobia' and 'buckliphilia' (Reis, 2015). In buckliphobia, the interest is finding the critical load over which a given structure can hold; whereas in buckliphilia, it is the overall shape of this mechanical instability that is exploited to induce novel function. An example of

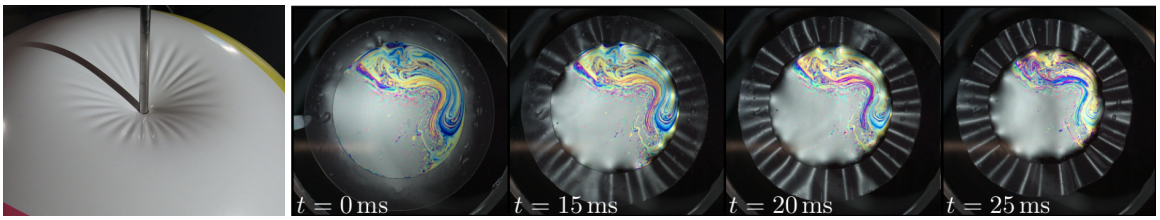

Figure 1.5: Dynamic buckling: The left picture illustrates the appearance of static wrinkles in a pressurized shell. Reprinted figure with permission from D. Vella, A. Ajdari, A. Vaziri and A. Boudaoud (2011). 'Wrinkling of pressurized elastic shells'. *Physical Review Letters* 107.17. DOI: 10.1103/PhysRevLett.107.174301. Copyright 2011 by the American Physical Society. The right picture is one frame during the coarsening of wrinkles after impact of an object on the floating membrane. Reprinted figure with permission from F. Box, O. Kodio, D. O'Kiely, V. Cantelli, A. Goriely and D. Vella (2020). 'Dynamic Buckling of an Elastic Ring in a Soap Film'. *Physical Review Letters* 124.19. DOI: 10.1103/physrevlett.124.198003. Copyright 2020 by the American Physical Society.

buckiphilia is *Smorph* (smart morphable surfaces), that have the remarkable property that their aerodynamic drag can be actively reduced (see Reis, 2015). In the latter case of buckliphila, the focus has mainly been on the static scenario where pattern formation is understood using energy minimization.

Moreover, it transpires that in this static scenario the selected length scale of buckling is comparable to the system size. However, to select other length scales it is necessary to add additional physics, and one such widely studied case in the literature is to put the beam in contact with a substrate, for example an elastic foundation (Biot, 1965). The mechanism of formed patterns in static scenarios can be understood quite easily using energy minimization: In the absence of a substrate the compressed beam will buckle with a wavelength comparable to the system size (large wavelength). However, in the absence of the beam the substrate will prefer to have a flat surface (small wavelength). When the two effects are combined there must be a compromise which minimizes the total energy. The corresponding selected wavelength is given by:

$$\lambda = 2\pi(B/K)^{1/4}, \tag{1.8}$$

where B is the bending stiffness of the beam and K is the stiffness of the substrate. We see that the wavelength is selected by the contrast between the two stiffnesses.

In (1.8), an additional source of stiffness (*e.g.* a substrate) is needed for the selection of a new length other than the system size. However, in dynamic buckling there can be an emergence of a new length scale under the influence of inertia alone

(without a substrate). Furthermore, the selected wavelength can be dependent on time. So in the situation of dynamic buckling, the simple energy minimization to find the selected wavelength is no longer applicable, mainly because the system will be in general in non-equilibrium. The goal of this thesis is to try understand the pattern formation in dynamic buckling, and then relate things back to static buckling, if and when possible.

Chapter 2

Dynamic buckling of a viscous ring

2.1 Introduction

In this chapter, we study the buckling of a circular viscous ring. This serves as a canonical problem of dynamical buckling as we are interested in finding out whether a ring made of a viscous liquid could actually buckle under the action of an imposed pressure; and if so, what would be the fastest growing mode? We consider this problem of dynamic buckling, of a viscous ring, to be interesting on its own right. However, it might also be used as a paradigm for studying more complicated problems involving thin viscous film under sudden compression. Two examples of such potential applications are:

First, the formation of glass tubing in an extrusion process. Here, internal suction is applied to reduce the radius of the tube that is fabricated. If the suction is too large then the tube cross-section can buckle.

Second, the crown sealing phenomena (observed in jets formed by the water entry of spheres Marston *et al.* (2016)). In these experiments a cylindrical splash sheet (the crown) is formed, which subsequently collapses when the neck of the crown collapses and appears to form a wrinkling pattern (see fig. 1.4left). Here the negative internal pressure of the ring mimics the Bernoulli pressure drop due to motion of spheres.

Marston *et al.* (2016) note that Gillbarg & Anderson (1948) "state that the crown splash is subject to two chief forces: an under-pressure caused by the air flow behind the sphere and surface tension". Also from Marston *et al.* (2016) it seems that the apparent Weber number is around 10, suggesting that surface tension is negligible in comparison to the Bernoulli pressure (though there is also some uncertainty about the right value of the Weber number). This makes it sensible to consider the problem of a viscous ring subject to a negative internal pressure (mimicking the Bernoulli pressure drop due to motion). In the problem treated here, we will neglect surface tension.

In particular, we are concerned with the question of determining the possibility of a circular viscous ring buckling under the influence of an external pressure (or, equivalently, a negative internal pressure). The equations governing the evolution of a viscida were established by Buckmaster *et al.* (1975) in the absence of inertia; its generalization to include inertia, together with a more rigorous treatment can be found in Howell (1994). Here, we generalize the equations provided by Buckmaster *et al.* (1975), Griffiths (2007), Howell (1994) and O'Kiely (2017) to combine both inertia and the effect of an externally applied pressure.

2.2 Theoretical formulation

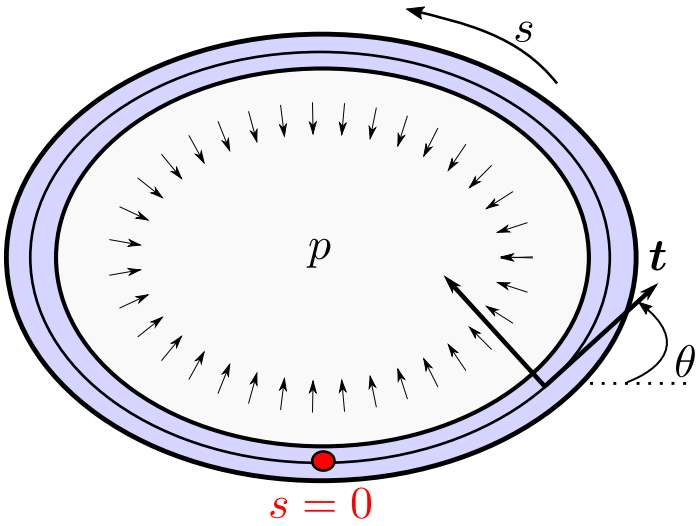

Figure 2.1: Schematic of a viscous ring subject to a negative internal pressure p (indicated by the arrows). The shape of the ring is described by its centreline with arclength s measured with respect to a point 0. At each point s, the normal and tangent vectors $\boldsymbol{n}$ and $\boldsymbol{t}$ are defined; together with the angle θ between the abscissa and the tangent vector $\boldsymbol{t}$.

We consider a viscida parametrized by its arc-length, $s \in [0, L]$, with L the length of its centreline with its ends closed. This ring is subject to an externally applied pressure p (or equivalently to an internally negative pressure). Even though the length of the ring may change during the dynamics, we assume it to be constant during the short time scales of the pressure-induced instability. Also for simplicity we assume the thickness, h_{T}, and the density, ρ, of the fluid to be uniform. We denote by $\theta(s,t)$ the angle between the abscissa and the tangent to the centreline. The bending moment, M, is given by the constitutive relation (Howell, 1994):

$$M = B\frac{\partial^2\theta}{\partial t\partial s}, \tag{2.1}$$

where $B = \frac{1}{3}\mu h_{\mathrm{T}}^3$ with μ the viscosity of the liquid. Note that B is like a bending stiffness, as it characterizes the local response of the ring to a local torque.

We denote by $\boldsymbol{F} = (F_x, F_y)$ the internal forces on the film, decomposed in the x and y directions. We also denote by $\boldsymbol{t}$, $\boldsymbol{n}$ and $\boldsymbol{k}$ the unit tangent, normal, and binormal vectors attached to the curve describing the centreline. These vector satisfy the relation $\partial_s\boldsymbol{r}(s,t) = \boldsymbol{t}$ and $\partial_s\boldsymbol{t} = \kappa\boldsymbol{n}$, where κ is the curvature. We denote by θ the angle between the x-axis and the tangent $\boldsymbol{t}$, so that $\boldsymbol{t} = (\cos\theta, \sin\theta)$. The equations governing the dynamics of the viscida are then found using force and moment balances (Howell *et al.*, 2009):

$$\frac{\partial\boldsymbol{F}}{\partial s} + p\boldsymbol{n} = \rho h\frac{\partial^2\boldsymbol{r}}{\partial t^2}, \tag{2.2}$$

$$\frac{\partial\boldsymbol{M}}{\partial s} + \boldsymbol{t}\times\boldsymbol{F} = \boldsymbol{0}, \tag{2.3}$$

Plugging (2.1) into (2.3), and projecting (2.2) – (2.3) into x and y directions, we obtain:

$$\frac{\partial F_x}{\partial s} - p\sin\theta = \rho h\frac{\partial^2 x}{\partial t^2}, \tag{2.4}$$

$$\frac{\partial F_y}{\partial s} + p\cos\theta = \rho h\frac{\partial^2 y}{\partial t^2}, \tag{2.5}$$

$$B\frac{\partial^3\theta}{\partial s^2\partial t} = F_x\sin\theta - F_y\cos\theta. \tag{2.6}$$

The inextensibility of the film's centerline is expressed by the geometrical relationships

$$\frac{\partial x}{\partial s} = \cos\theta, \tag{2.7}$$

$$\frac{\partial y}{\partial s} = \sin\theta. \tag{2.8}$$

Since we consider a ring, we make use of periodic boundary conditions

$$\theta(L,t) = \theta(0,t) + 2\pi, \quad \frac{\partial}{\partial s}\theta(L,t) = \frac{\partial}{\partial s}\theta(0,t), \quad x(L,t) = x(0,t), \tag{2.9}$$

$$y(L,t) = y(0,t), \quad F_x(L,t) = F_x(0,t), \quad F_y(L,t) = F_y(0,t), \tag{2.10}$$

where we recall that L is the total length of the centreline of the ring, and consider an initial condition of a circular ring of radius a, *i.e.* $\theta(s,0) = s/a$, where $a = L/2\pi$.

2.3 Small curvature limit

Before performing a more formal analysis, we try to gain some intuition by considering the limit of large rings (small curvature). This intuitive understanding of the dynamics will also be useful to understand more detailed calculations.

The equations (2.4)–(2.10) admit a stationary circular solution under uniform pressure:

$$\theta_0 = s/a, \tag{2.11}$$
$$x_0 = a \sin\theta_0, \tag{2.12}$$
$$y_0 = -a \cos\theta_0, \tag{2.13}$$
$$F_x^{(0)} = -p\, a \cos\theta_0, \tag{2.14}$$
$$F_y^{(0)} = -p\, a \sin\theta_0. \tag{2.15}$$

We linearize around this base state, therefore let:

$$x(s,t) = x_0(s) + \epsilon x_1(s,t), \tag{2.16}$$
$$y(s,t) = y_0(s) + \epsilon y_1(s,t), \tag{2.17}$$
$$\theta(s,t) = \theta_0(s) + \epsilon \theta_1(s,t), \tag{2.18}$$
$$F_x(s,t) = F_x^{(0)}(s) + \epsilon F_x^{(1)}(s,t), \tag{2.19}$$
$$F_y(s,t) = F_y^{(0)}(s) + \epsilon F_y^{(1)}(s,t), \tag{2.20}$$

with $\epsilon \ll 1$ an arbitrary, but small number. Here the linearized model will be valid for small deformations, the size of which is given by ϵ. Expanding (2.4)–(2.10) to first order in ϵ we obtain:

$$\frac{\partial x_1}{\partial s} = -\theta_1 \sin\theta_0, \tag{2.21}$$
$$\frac{\partial y_1}{\partial s} = \theta_1 \cos\theta_0, \tag{2.22}$$
$$B\frac{\partial^3 \theta_1}{\partial s^2 \partial t} + pa\theta_1 - F_x^{(1)} \sin\theta_0 + F_y^{(1)} \cos\theta_0 = 0, \tag{2.23}$$
$$\frac{\partial F_x^{(1)}}{\partial s} - p\theta_1 \cos\theta_0 = \rho h \frac{\partial^2 x_1}{\partial t^2}, \tag{2.24}$$
$$\frac{\partial F_y^{(1)}}{\partial s} - p\theta_1 \sin\theta_0 = \rho h \frac{\partial^2 y_1}{\partial t^2}. \tag{2.25}$$

Now we take the limit $a \to \infty$, which is to be understood in the sense that $\frac{\ell}{a} \ll 1$ where ℓ is the extent of the arc-length being considered, $\ell \ll L$. In this limit we re-evaluate the expression of the base solution, for example we compute x_0 in the following way: Noting that $0 \leq s \leq \ell$ then $\bar{s} = \frac{s}{\ell} \in [0, 1]$ therefore

$$x_0 = a \sin\left(\frac{s}{a}\right) = \ell \frac{\sin\left(\bar{s}\frac{\ell}{a}\right)}{\frac{\ell}{a}} \to \bar{s}\ell = s. \tag{2.26}$$

We proceed by taking the limit $a \to \infty$, and a straightforward calculation allows us to reduce (2.21)–(2.25) to

$$B\frac{\partial^5 y_1}{\partial x^4 \partial t} + pa\frac{\partial^2 y_1}{\partial x^2} + \rho h \frac{\partial^2 y_1}{\partial t^2} = 0. \tag{2.27}$$

It is to be noted that equation (2.27) describes the inertial dynamics of a viscous beam.

Since we consider only a small portion of the ring, we cannot apply the same boundary conditions; instead we seek normal mode $y_1(x, t) \propto \mathrm{e}^{\sigma t + ikx}$ of (2.27). These normal-mode solutions must have growth rate σ, and wavenumber k, related by the dispersion relation

$$\rho h \sigma^2 + Dk^4\sigma - pak^2 = 0. \tag{2.28}$$

Maximizing the growth rate (2.28) with respect to k, we find that the mode with largest growth rate has wavenumber

$$k_{\text{fast}} \sim \left(\frac{pa}{\mu\nu h^5}\right)^{1/6}. \tag{2.29}$$

Here we see that the fastest growing wavenumber number depends not only on the imposed pressure (which is the control parameter for this instability) but also on the density of the viscous fluid, which comes into play via inertia. Also (2.29) informs us how the selected wavelength may be tuned experimentally: for example to increase the most unstable wavenumber we can decrease either the viscosity of the fluid or the film thickness. Furthermore, we anticipate that qualitatively the dependence of the wavenumber on the pressure is relatively weak (exponent 1/6).

Having performed this relatively simple calculation, we now return to the complete ring problem. This will allow us to investigate more precisely how a given mode will be selected by an imposed pressure. We will perform a linear stability analysis of the full governing equations without the assumption of a small ring curvature.

2.4 Linear Stability Analysis

In the following we non-dimensionalize arc-length by the initial circle radius a, time by $t_* = \frac{3\rho a^4}{\mu h^2}$, forces by $F_* = \frac{\mu^2 h^5}{9\rho a^6}$ and the imposed pressure by $p_* = \frac{\mu^2 h^5}{9\rho a^7}$. The new dimensionless variables are then $\bar{s} = s/a$, $\bar{t} = t/t_*$, $\bar{F} = F/F_*$, $P = p/p_*$. Note that the choice of the pressure scale p_* is informed by the simplified analysis presented in §2.3 — we expect to recover the result (2.29) in the limit $P \gg 1$. We drop the bars, and henceforth rewrite the system (2.4)–(2.10) as:

$$\frac{\partial x}{\partial s} = \cos\theta, \tag{2.30}$$

$$\frac{\partial y}{\partial s} = \sin\theta, \tag{2.31}$$

$$\frac{\partial^3 \theta}{\partial s^2 \partial t} = F_x \sin\theta - F_y \cos\theta, \tag{2.32}$$

$$\frac{\partial F_x}{\partial s} - P\sin\theta = \frac{\partial^2 x}{\partial t^2}, \tag{2.33}$$

$$\frac{\partial F_y}{\partial s} + P\cos\theta = \frac{\partial^2 y}{\partial t^2}. \tag{2.34}$$

In the following we proceed by performing a linear stability analysis of (2.30)–(2.34). Since the geometry is circular, the mode numbers must be integers, which we denote by n; the associated growth rate is σ.

Using standard methods, we expand the equations (2.30)–(2.34) in first order and obtain a system of linear homogeneous equations that has a solution if and only the determinant vanishes, from which we obtain the dispersion relation:

$$\sigma^2(1+n^2) + (n^2 - 2n^4 + n^6)\sigma + n^2 P(1-n^2) = 0. \tag{2.35}$$

Maximizing the growth rate, σ, as the solution of (2.35) gives a relation between the selected mode and the imposed dimensionless pressure P:

$$P = \frac{n^4(n^2-1)^3(-1+3n^2+2n^4)}{(n^4+2n^2-1)^2}. \tag{2.36}$$

Note that that for large n, equation (2.36) implies that $n \sim (P/2)^{1/6}$ (so that large n corresponds to large pressure). This relationship recovers the results of the earlier analysis (2.29).

We now turn to the numerical solution of the full governing equations (2.30)–(2.34) to test whether the prediction of unstable modes, and a fastest growing mode is in agreement with the full system, see fig 2.2.

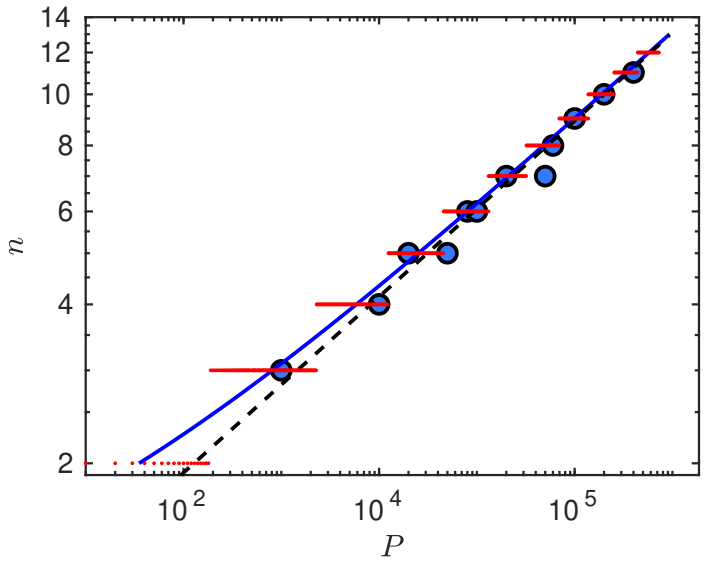

Figure 2.2: The mode number n observed for different imposed external pressures, P: large blue dots correspond to the mode observed in numerical solutions of the full system (2.30)–(2.34) at the onset of instability. The mode number observed numerically agrees well with the most unstable (integer) mode predicted from a linear stability analysis (small red points). This analytical result is itself well approximated by the continuous prediction (solid black curve) in which n is treated as a continuous variable (see (2.36)); while for $P \gg 1$, recovers the asymptotic scaling $n_c \sim (P/2)^{1/6}$, which is shown as the dashed line.

2.5 Numerical integration

We use a finite difference method to solve the system (2.30)–(2.34): The equations are discretized in time, t, and arc length, s, resulting in a system of nonlinear equations that are solved using Newton's method.

This discretization for the variables at spatial location $s_i = (i-1)\Delta s$, and time $t_j = (j-1)\Delta t$ (with Δs and Δt the spatial and temporal grid spacings, respectively.) For any function $f(s,t)$, we define $f_i^j = f(s_i, t_j)$ so that the system (2.30)–(2.34)

becomes:

$$\frac{x_{i+1}^j - x_i^j}{\Delta s} = \cos\theta_{i+1/2}, \tag{2.37}$$

$$\frac{y_{i+1}^j - y_i^j}{\Delta s} = \sin\theta_{i+1/2}^j, \tag{2.38}$$

$$\frac{\theta_{i+1}^j - \theta_i^j}{\Delta s} = \kappa_{i+1/2}^j, \tag{2.39}$$

$$\frac{\omega_{i+1}^j - \omega_i^j}{\Delta s} = F_{x,\,i+1/2}^j \sin\theta_{i+1/2}^j - F_{y,\,i+1/2}^j \cos\theta_{i+1/2}^j, \tag{2.40}$$

$$\omega_i^j = \frac{3\kappa_i^j - 4\kappa_i^{j-1} + \kappa_i^{j-2}}{2\Delta t}, \tag{2.41}$$

$$v_{x,\,i}^j = \frac{3x_i^j - 4x_i^{j-1} + x_i^{j-2}}{2\Delta t}, \tag{2.42}$$

$$v_{y,\,i}^j = \frac{3y_i^j - 4y_i^{j-1} + y_i^{j-2}}{2\Delta t}, \tag{2.43}$$

$$\frac{F_{x,\,i+1}^j - F_{x,\,i}^j}{\Delta s} - P\sin\theta_{i+1/2}^j = \frac{3v_{x,\,i+1/2}^j - 4v_{x,\,i+1/2}^{j-1} + v_{x,\,i+1/2}^{j-2}}{2\Delta t}, \tag{2.44}$$

$$\frac{F_{y,\,i+1}^j - F_{y,\,i}^j}{\Delta s} + P\cos\theta_{i+1/2}^j = \frac{3v_{y,\,i+1/2}^j - 4v_{y\,i+1/2}^{j-1} + v_{y,\,i+1/2}^{j-2}}{2\Delta t}. \tag{2.45}$$

Where $\omega = \frac{\partial\kappa}{\partial t}$, $v_x = \frac{\partial x}{\partial t}$, and $v_y = \frac{\partial y}{\partial t}$. Note that here and elsewhere we use the convention that $f_{i+1/2} = (f_i + f_{i+1})/2$ for $f \in \{v_x, v_y, \theta, \kappa, \omega, F_x, F_y\}$. The nonlinear equations generated by this discretization was solved numerically using Newton's method.

Initially the ring velocity is equal to zero, and the shape of the ring is circular with a uniformly distributed random number $\mathcal{R}_i \in [-\varepsilon, \varepsilon]$, with $\varepsilon \ll 1$, added to the local radius of curvature at each point. More specifically the initial data at arc-length $s_i = (i-1)\Delta s$ is

$$\theta(s_i, 0) = s_i, \quad x(s_i, 0) = (1 + \mathcal{R}_i)\sin(s_i), \quad y(s_i, 0) = -(1 + \mathcal{R}_i)\cos(s_i). \tag{2.46}$$

Given the values of the variables at times t_{j-2} and t_{j-1}, the system (2.37) – (2.45) can be solved at time t_j using a Newton solver; we use the MATLAB routine `fsolve` to find these solutions. Typically we use $\Delta t = 10^{-4}$ and $N = 256$ grid points.

Fig. 2.3 illustrates snapshots of the evolution of the profile for a viscous ring for several imposed pressures. We note that higher values of imposed pressure select higher mode numbers and that the instability grows more quickly for larger pressures. The relation between the selected mode number and the imposed pressure is in good agreement with the theory from linear stability (see fig. 2.2).

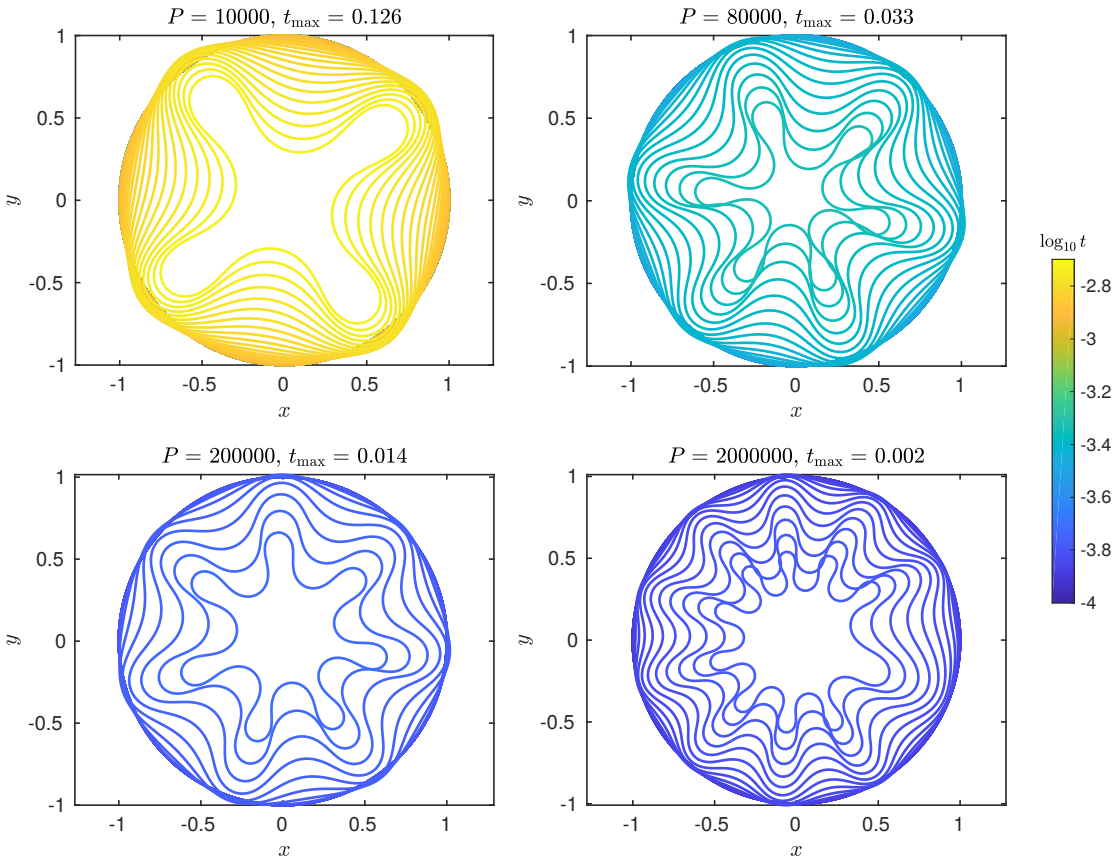

Figure 2.3: Dynamic evolution of a viscous ring subject to a dimensionless pressure, P for $t > 0$. For each pressure, ring profiles are shown at different times (with the time coded by its colour). These profiles are obtained by numerically solving the governing equations (2.30)–(2.34) starting with a circular initial condition with a random perturbation to the initial circular state of $\varepsilon = 5 \times 10^{-8}$. The initial velocity is zeros. These simulations use $N = 256$ grid points, a time step $\Delta t = 10^{-4}$.

2.6 Conclusion and discussion

In this chapter, we have shown that a viscous ring subject to a sudden external pressure can exhibit a spontaneous selection of mode. This is chiefly a feature of dynamic buckling as inertia is need here for selection of pattern.

Having established the existence of instability and the relation between the fastest growing mode and the applied pressure, we now turn to the experiment of Marston *et al.* (2016). Recalling that the dimensional pressure $p = Pp_*$ we find that selected mode number scales like

$$n \sim a^{7/6} \left(\frac{\rho p}{\mu^2 h^5} \right). \tag{2.47}$$

Here we can estimate the pressure by the Bernoulli pressure drop behind the impact-

ing sphere, $p = \frac{1}{2}\rho V_0^2$ where V_0 is the velocity of the sphere. Since we do not have access to the radius of the ring, a, when wrinkling initially starts, we assume that this radius scales as the diameter of the impacting spheres D_0. With these assumptions, our theory predicts that the number of wrinkles scales as $n \sim D_0^{7/6}$. However, experimentally Marston *et al.* (2016) found that for water the observed number of wrinkles behaves as $n \sim D_0^{3/4}$ rather than $D_0^{7/6}$ as predicted by our theory. A possible reason of discrepancy between this prediction and the experimental data is that the pressure induced by the Bernoulli pressure drop behind the sphere would lead to a much larger number of wrinkles than we see. From there one might initially anticipate that this Bernoulli pressure might not be the right mechanism. The other alternative mechanism is whether surface tension would help resolve the problem. Experimental uncertainties are the thickness of the film and the pressure within the cavity. Some more experiments are needed to determine precisely the value of the thickness as our prediction is quite sensitive to the thickness to the film.

Given these uncertainties in the pressure p and the thickness h_T, we focus instead in the next chapter on a problem where these are known — the dynamic buckling of an elastic ring.

This chapter has served to exemplify the qualitative observations of buckling of a viscous ring. We would expect the simpler tube-drawing process mentioned in the introduction to behave in a way that is more predictable by our mathematical model. Not only does this fix many of the features that are unknown in the crown-jet experiment, the tube-drawing process also isolates the key elements of interest of the buckling of a viscous ring that we studied in this chapter from other dynamic fluid aspects. It would be interesting to compare the findings of this chapter with studies performed in the glass-tube manufacturing industry.

Chapter 3

Dynamic buckling of an elastic ring

3.1 Introduction

In this chapter, we shall consider the dynamical evolution of an elastic ring subject to an external pressure. It is well known that when an elastic ring is subject to a quasi-statically increasing external pressure, it buckles into an ellipse. We shall focus in understanding how this example of mode-2 buckling changes under a truly dynamic loading. In particular, we show that the presence of inertia means that higher modes are observed at the onset of instability, and present results for the observed mode number as a function of the driving pressure. Our results are in accord with experiments in which an elastic ring is rapidly pulled inwards by surface tension (see fig. 3.1). This is mathematically equivalent to a rapidly applied external compressive load. Surprisingly, we find that while inertia is required to observe higher modes, the actual mode selected does not depend on inertia. This independence of the selected mode on inertia is explained as the result of the step loading that is applied; we reconcile our observation of higher modes with the static observation of mode 2, by understanding the interaction between the growth rate of instability and the rate of loading.

3.2 Experimental background and heuristic theory

Experiment by Box *et al.* (2020) considered an elastic ring placed within a soap film. While the soap film remains intact, the ring remains in equilibrium. At time $t = 0$ the outer film is burst leading to an imbalanced surface tension thence that causes the ring to buckle in the plane. While the system remains two dimensional this is equivalent to an external pressure $p = \gamma/h$ acting on the ring, with h the cross-sectional diameter. As the relative strength of surface tension is increased, higher

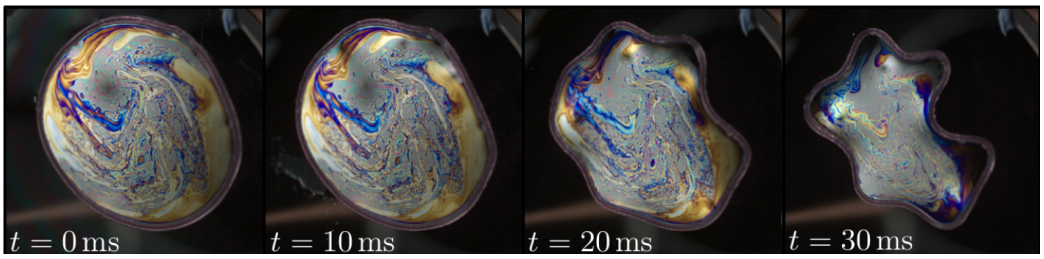

Figure 3.1: Experimental snap-shots from the dynamic buckling of an elastic ring under the action of an unbalanced surface tension. The ring is initially trapped within a soap film so that surface tension forces balance on either side. The outer film ruptures at $t = 0$ leading to an imbalanced of surface tension equivalent to a pressure $p = \gamma/h$. Here the effective pressure $P = pa^3/B = 56$ is much higher than the critical pressure $P_c = 3$. Reprinted figure with permission from F. Box, O. Kodio, D. O'Kiely, V. Cantelli, A. Goriely and D. Vella (2020). 'Dynamic Buckling of an Elastic Ring in a Soap Film'. *Physical Review Letters* 124.19. DOI: `10.1103/physrevlett.124.198003`. Copyright 2020 by the American Physical Society.

modes are dynamically selected(see fig 3.1). To gain a heuristic insight into these experiments, we start with a simple toy model of an elastic beam, rather than a ring, in which we assume that the important effect of the applied pressure p on the ring is to induce an in-plane compressive force $\mathcal{F} = p\,a$ where a is the radius of the ring. The pressure p is ultimately due to surface tension, but we discuss the precise mechanism for this later.

In linear beam theory the governing equation for the vertical deflection $w(x,t)$ of a beam of length L is (Lange and Newell, 1971):

$$\rho h \frac{\partial^2 w}{\partial t^2} + B\frac{\partial^4 w}{\partial x^4} + \mathcal{F}\frac{\partial^2 w}{\partial x^2} = 0, \tag{3.1}$$

where ρ is the density, B the bending stiffness, and h the cross-sectional diameter of the beam, and we recall that $\mathcal{F}$ is the compressive force. For simplicity we consider a pinned-pinned boundary condition. This equation exhibits growing buckled solutions of the form $w(x,t) = K\exp(\sigma t)\sin(2n\pi x/L)$ if

$$\left(\frac{\rho h L^4}{(2\pi)^4 B}\right)\sigma^2 = n^2\left(\frac{\mathcal{F}L^2}{4\pi^2 B} - n^2\right). \tag{3.2}$$

By examining the maximum value of the growth rate, σ, as a function of n in (3.2), we see that the n^{th} mode is the fastest growing mode (and hence expected to be selected) if the compressive force is suddenly raised to $\mathcal{F}_n = 8n^2\pi^2 B/L^2$, see fig. 3.2. Alternatively, if a particular force $\mathcal{F}$ is imposed then we might expect that

the observed mode would be

$$n \approx \frac{1}{2^{3/2}\pi}\left(\frac{\mathcal{F}L^2}{B}\right)^{1/2}, \tag{3.3}$$

since it will be close to the fastest growing mode. This selection of a mode other than the lowest Euler mode (which corresponds to $n = 1$) is made possible by the presence of the inertia term $\rho h \frac{\partial^2 w}{\partial t^2}$ in (3.1). However, the object's density, ρ, does not appear in (3.3).

Although the above calculation gives us an intuitive feel for the problem of dynamic buckling, it is expected to be only quantitatively accurate for an elastic beam subject to a controlled compressive force $\mathcal{F}$. Achieving such a condition experimentally is difficult and is perhaps closest to being achieved by an impactor with a known weight, see Gladden *et al.* (2005), though then the imposed force becomes dependent on the imposed boundary conditions. The case of an elastic ring embedded in a soap film comes closer to a truly controlled force, but the question then becomes how the calculation that leads to (3.3) is modified by the curvature of the ring $\kappa = 1/a$, with a the ring radius. Moreover, we are interested in how instability develops beyond onset. These are the questions that are addressed in this chapter.

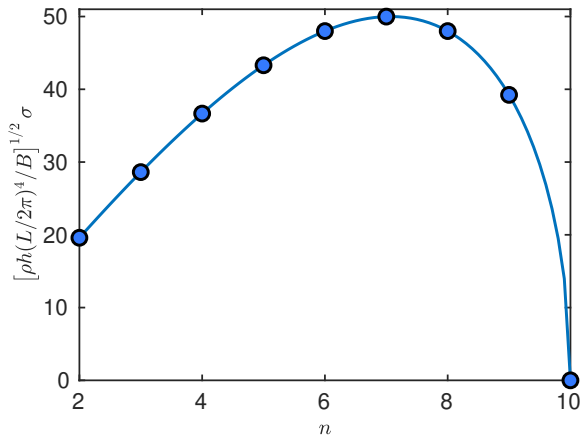

Figure 3.2: Growth rate as a function of the mode number n. Here we plot eq (3.2) for $\mathcal{F}L^2/(4\pi^2 B) = 100$. The blue points are for integer values of n, and the solid curve is obtained by treating n as continuous. We note that the growth rate σ has a maximum at $n = 7$ which corresponds to the fastest growing mode.

3.3 Theoretical formulation

3.3.1 Model problem

We consider a circular elastic ring of radius, a, subject to an externally applied pressure p. We model the elastic ring as an inextensible rod of length $L = 2\pi a$, parametrized by its arclength $s \in [0, L]$. The ring is composed of a material of density ρ, Young's modulus E, and its circular cross section has cross sectional area $A_\times$ and second moment of area $I = A_\times^2/(4\pi)$ which gives a bending stiffness $B = EI = EA_\times^2/(4\pi)$.

The position of a material point on the ring centreline at a time t is denoted by the vector $\boldsymbol{r}(s,t) = x\boldsymbol{e}_x + y\boldsymbol{e}_y + z\boldsymbol{e}_z \in \mathbb{R}^3$ (Fig. 3.3). Previous studies have shown that the static equilibrium of a ring with an internal soap film may take a saddle shape (see Chen and Tsao, 2014; Giomi and Mahadevan, 2012). Indeed the ring may buckle out of the plane, in three dimension. In particular this will be the case when the ring has a large width, or, for circular rings with twist. The onset of the out of the plane buckling for wider rings has been investigated by Box *et al.* (2020). Furthermore, it is has been pointed out by Wah (1970), that the out of the plane motion is coupled to the torsional motion. However, in our problem the ring is observed experimentally to remain in the plane planar and so we restrict our attention to planar deformations. With the assumption of planarity, we denote by $\boldsymbol{t}$, $\boldsymbol{n}$ and $\boldsymbol{k}$ the unit tangent, normal, and binormal vectors attached to the curve describing the centreline. These vector satisfy the relation $\partial_s \boldsymbol{r}(s,t) = \boldsymbol{t}$ and $\partial_s \boldsymbol{t} = \kappa \boldsymbol{n}$, where κ is the curvature. We denote by θ the angle between the x-axis and the tangent $\boldsymbol{t}$, so that $\boldsymbol{t} = (\cos\theta, \sin\theta)$.

The motion of the elastic ring is governed by Kirchhoff's equations, see Love (1959), or Audoly and Pomeau (2010). Let $p\boldsymbol{n}$ be the external body force per unit length due to the applied pressure and denote by $\boldsymbol{F}$, $\boldsymbol{M}$ the resultant force and moment, respectively, acting on the centreline. The balances of linear and angular momenta then lead to (Antman, 2005; Goriely, 2017):

$$\frac{\partial \boldsymbol{F}}{\partial s} + p\boldsymbol{n} = \rho A_\times \frac{\partial^2 \boldsymbol{r}}{\partial t^2}, \tag{3.4}$$

$$\frac{\partial \boldsymbol{M}}{\partial s} + \boldsymbol{t} \times \boldsymbol{F} = \boldsymbol{0}, \tag{3.5}$$

where, in the last equation, we have ignored the rotational inertia terms (see Goriely, 2017, p.115). Indeed, the relative magnitude of the rotational inertia scales as $\eta = \frac{h^2}{12L^2}$, (see Neukirch *et al.*, 2012). In the experiment of Box *et al.* (2020) which motivated this chapter, we typically have $\eta \approx 10^{-4}$.

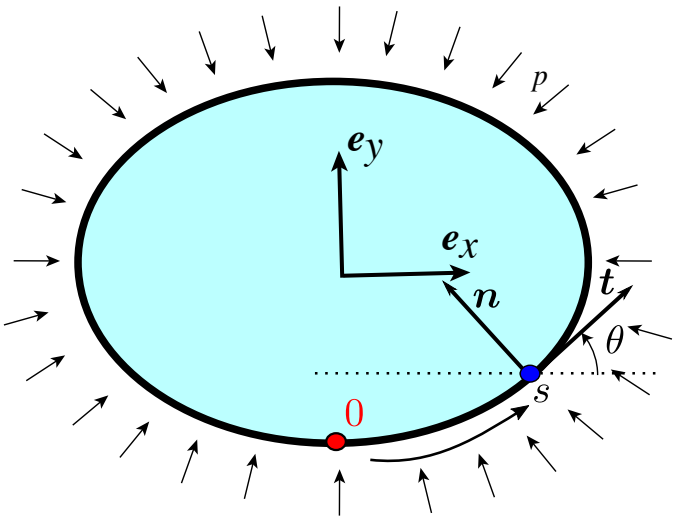

Figure 3.3: Schematic of an elastic ring subject to an external pressure p (indicated by the arrows). The shape of the ring is described by its centreline with arclength s measured with respect to a point 0. At each point s, the normal and tangent vectors $\boldsymbol{n}$ and $\boldsymbol{t}$ are defined together with the angle θ between the horizontal x-axis and the tangent vector $\boldsymbol{t}$. Reprinted figure with permission from O. Kodio, A. Goriely and D. Vella (2020). 'Dynamic buckling of an inextensible elastic ring: Linear and nonlinear analyses'. *Physical Review E* 101.5. DOI: 10.1103/physreve.101.053002. Copyright 2020 by the American Physical Society.

The governing equations are closed by the constitutive relation $\boldsymbol{M} = B\kappa(s,t)\boldsymbol{k}$ and the constraint that the ring is unshearable and inextensible.

We rescale all lengths by the radius of the initial unstressed ring a, pressure by $p_* = B/a^3$, and time by the inertial time scale $t_* = a^2\left(\rho A_\times/B\right)^{1/2}$.

In the new dimensionless variables, the governing equations projected on $\boldsymbol{e}_x$ and $\boldsymbol{e}_y$, are

$$\frac{\partial x}{\partial s} = \cos\theta, \tag{3.6}$$

$$\frac{\partial y}{\partial s} = \sin\theta, \tag{3.7}$$

$$\frac{\partial^2\theta}{\partial s^2} = F_x\sin\theta - F_y\cos\theta, \tag{3.8}$$

$$\frac{\partial F_x}{\partial s} - P\sin\theta = \frac{\partial^2 x}{\partial t^2}, \tag{3.9}$$

$$\frac{\partial F_y}{\partial s} + P\cos\theta = \frac{\partial^2 y}{\partial t^2}. \tag{3.10}$$

This non-dimensionalization introduces the dimensionless parameter

$$P = \frac{pa^3}{B}, \tag{3.11}$$

which is the control parameter in the problem. The parameter P measures the importance of the work done by the external pressure compared to the bending energy of the ring, as described by Chen and Fried (2014). Alternatively, P, measures the effective compressive pa to the typical buckling load B/a^2.

The system of equations (3.6)–(3.10) is closed by the boundary conditions

$$\theta(2\pi,t) = \theta(0,t) + 2\pi, \quad \partial_s\theta(2\pi,t) = \partial_s\theta(0,t), \quad x(2\pi,t) = x(0,t), \tag{3.12}$$

$$y(2\pi,t) = y(0,t), \quad F_x(2\pi,t) = F_x(0,t), \quad F_y(2\pi,t) = F_y(0,t), \tag{3.13}$$

and the initial condition that the ring is stationary and is a circle of radius 1 (though a small amount of noise is added to initiate instability in our numerical simulations). More specifically the initial condition is given by:

$$\theta(s,0) = s, \quad x(s,0) = (1+\mathcal{R}(s))\sin(s), \quad y(s,0) = -(1+\mathcal{R}(s))\cos(s), \tag{3.14}$$

where $\mathcal{R}(s)$ is a uniformly distributed random number $\mathcal{R} \in [-\varepsilon, \varepsilon]$, with $\varepsilon \ll 1$

3.3.2 Numerical simulations

Before looking for asymptotic solutions, we present numerical solutions for the evolution of this elastic ring under imposed pressure.

Following Santillan (2007) we discretize (3.6)–(3.13) in time t *and* in arclength s; this results in a system of nonlinear equations that are solved using Newton's method. In particular, we consider discrete time points $t_j = (j-1)\Delta t$, where typically $\Delta t = 5 \times 10^{-3}$ in the simulations reported in this chapter. The arclength along the ring is discretized to $N+1$ grid-points at $s_i = (i-1)\Delta s$ where $\Delta s = 2\pi/N$, and $i \in [1, N+1]$.

The system (3.6)–(3.13) does not involve any time derivative of the forces F_x and F_y; we therefore cannot use a simple forward time stepping scheme. Instead, we need to solve for these forces and the rest of the equations together, in a single time step. To do this we use a second order accurate, one-sided time derivative, (Chung, 2002) accurate to $\mathcal{O}(\Delta t^2)$.

$$\frac{\partial x}{\partial t} := \frac{3x^j - 4x^{j-1} + x^{j-2}}{2\Delta t} = v_x(t_j, s), \tag{3.15}$$

where we define the velocity v_x and similarly $v_y = \frac{\partial y}{\partial t}$ for later notational convenience. Derivatives with respect to arclength are discretized using central differences. The

discretized versions of (3.6)–(3.10) read:

$$\frac{x_{i+1}^j - x_i^j}{\Delta s} = \cos\theta_{i+1/2}^j, \tag{3.16}$$

$$\frac{y_{i+1}^j - y_i^j}{\Delta s} = \sin\theta_{i+1/2}^j, \tag{3.17}$$

$$\frac{\theta_{i+1}^j - \theta_i^j}{\Delta s} = \kappa_{i+1/2}^j, \tag{3.18}$$

$$\frac{\kappa_{i+1}^j - \kappa_i^j}{\Delta s} = F_{x,\,i+1/2}^j \sin\theta_{i+1/2}^j - F_{y,\,i+1/2}^j \cos\theta_{i+1/2}^j, \tag{3.19}$$

$$v_{x,\,i}^j = \frac{3x_i^j - 4x_i^{j-1} + x_i^{j-2}}{2\Delta t}, \tag{3.20}$$

$$v_{y,\,i}^j = \frac{3y_i^j - 4y_i^{j-1} + y_i^{j-2}}{2\Delta t}, \tag{3.21}$$

$$\frac{F_{x,\,i+1}^j - F_{x,\,i}^j}{\Delta s} - P\sin\theta_{i+1/2}^j = \frac{3v_{x,\,i+1/2}^j - 4v_{x,\,i+1/2}^{j-1} + v_{x,\,i+1/2}^{j-2}}{2\Delta t}, \tag{3.22}$$

$$\frac{F_{y,\,i+1}^j - F_{y,\,i}^j}{\Delta s} + P\cos\theta_{i+1/2}^j = \frac{3v_{y,\,i+1/2}^j - 4v_{y\,i+1/2}^{j-1} + v_{y,\,i+1/2}^{j-2}}{2\Delta t}. \tag{3.23}$$

Note that here we use the notational convention that $f_{i+1/2} = (f_i + f_{i+1})/2$ for $f \in \{v_x, v_y, \theta, \kappa, F_x, F_y\}$.

The initial velocity is zero, and the initial shape of the ring is circular with a uniformly distributed random number $\mathcal{R}_i \in [-\varepsilon, \varepsilon]$, with $\varepsilon \ll 1$, added to the local radius of curvature at each point; in particular, the discretized initial state at arclength $s_i = (i-1)\Delta s$ is

$$\theta(s_i, 0) = s_i, \quad x(s_i, 0) = (1 + \mathcal{R}_i)\sin(s_i), \quad y(s_i, 0) = -(1 + \mathcal{R}_i)\cos(s_i). \tag{3.24}$$

Given the values of the variables at times t_{j-2} and t_{j-1}, the system (3.16) – (3.23) can be solved at time t_j using a Newton solver; we use the MATLAB routine `fsolve` to find these solutions. The accuracy of our numerical scheme is discussed in appendix 3.A.

Snapshots of the evolution of the ring profile for different values of the imposed pressure, P, are shown in Fig. 3.4. These show two trends: First, the selected mode number of the instability (defined as the number of lobes) increases with the imposed pressure P. Second, the instability develops notably faster for larger values of P. Furthermore, note that for late time the shape of the solutions become non symmetric which may be due to the excitation of neighboring modes. These initial observations motivate asymptotic analyses of the problem, to which we now turn.

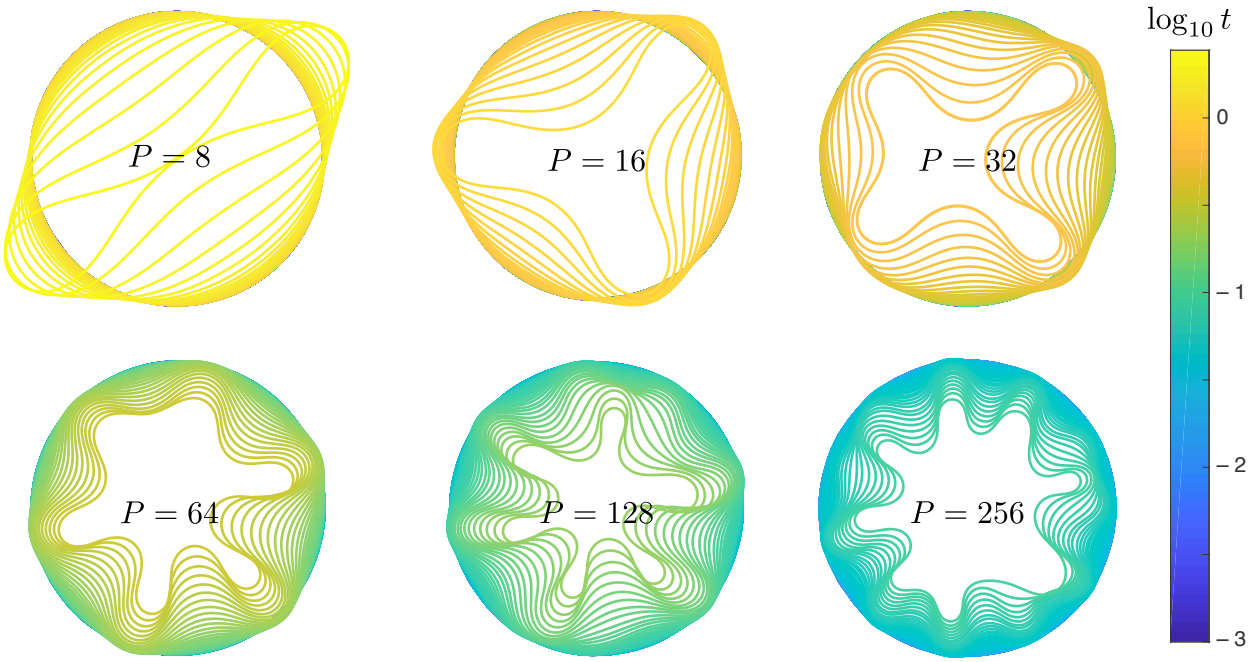

Figure 3.4: Dynamic evolution of an elastic ring subject to a constant, externally-applied, pressure for $t > 0$. Results are shown for different values of the dimensionless pressure, P, defined in (3.11). For each pressure, profiles of the ring are shown at different times (with the time coded by its colour as indicated in the colour bar to the right). Note that as the pressure increases (i) the observed mode number (the number of lobes) increases and (ii) the instability progresses more quickly (for the highest pressure, the instability has progressed further, despite profiles being shown for earlier times). Also, note that for late times the solutions become non symmetric; this may be due to the excitation of neighboring modes. These profiles are obtained by numerically solving the governing equations (3.6)–(3.10) starting with a circular initial condition and zero initial velocity. The simulations shown here use $N = 256$ grid points, a time step $\Delta t = 10^{-3}$, and a random perturbation to the initial circular state as in (3.24) with perturbation size $\varepsilon = 5 \times 10^{-3}$. Reprinted figure with permission from O. Kodio *et al.* (2020). 'Dynamic buckling of an inextensible elastic ring: Linear and nonlinear analyses'. *Physical Review E* 101.5. DOI: `10.1103/physreve.101.053002`. Copyright 2020 by the American Physical Society.

3.4 Analysis

While the formulation of Newton's second law (3.6) –(3.10) is convenient for numerics, it is somewhat cumbersome for analytical progress. To facilitate the subsequent analysis, we therefore first express the governing equations in the moving frame of the ring $(\boldsymbol{t}, \boldsymbol{n}, \boldsymbol{k})$, which is a right-handed orthonormal frame attached to the centreline of the ring at arclength position s. We start by eliminating the force $\boldsymbol{F}$ from equation

(3.4) to obtain a single equation for the vector position $\boldsymbol{r}$ together with the inextensibility constraint. The (dimensionless) bending moment is given by the constitutive equation $\boldsymbol{M} = \kappa(s,t)\boldsymbol{k}$. Here, and henceforth, we use a prime to denote derivatives with respect to the arclength s and an overdot for derivatives with respect to time t. Since $\kappa\boldsymbol{k} = \boldsymbol{r}' \times \boldsymbol{r}''$, the resultant moment can be written

$$\boldsymbol{M} = \boldsymbol{r}' \times \boldsymbol{r}''. \tag{3.25}$$

Substituting (3.25) into the dimensionless version of (3.5) then gives

$$\boldsymbol{r}' \times (\boldsymbol{r}''' + \boldsymbol{F}) = \boldsymbol{0}, \tag{3.26}$$

which immediately implies that

$$\boldsymbol{r}''' + \boldsymbol{F} = \lambda \boldsymbol{r}' + \beta \boldsymbol{k}, \tag{3.27}$$

for some unknown functions $\lambda(s,t)$ and $\beta(s,t)$. However, since we consider only planar deformations, we have $\beta = 0$ and

$$\boldsymbol{F} = -\boldsymbol{r}''' + \lambda \boldsymbol{r}'. \tag{3.28}$$

We note that, if redimensionalized, the term involving λ in (3.28) would have the units of force and contributes to the tangential component of the internal force (Singh and Hanna, 2019). Using the expression for the force (3.28) in (3.4) gives

$$\ddot{\boldsymbol{r}} = -\boldsymbol{r}^{(4)} + (\lambda \boldsymbol{r}')' + P\boldsymbol{n}, \tag{3.29}$$

subject to the local inextensibility constraint

$$\boldsymbol{r}'^2 = 1. \tag{3.30}$$

The two equations (3.29)–(3.30) form a system for the two unknowns $\boldsymbol{r}(s,t)$ and $\lambda(s,t)$.

Since we are interested in the evolution of the ring away from its initially circular configuration, we take advantage of the circular geometry to consider arbitrary displacements from this shape with respect to the polar vectors associated with the circle. The curvature of the ring in its initial configuration, together with the tangential and normal vectors, are:

$$\kappa_0 = 1, \tag{3.31}$$

$$\boldsymbol{t}_0 = \cos(s)\boldsymbol{e}_x + \sin(s)\boldsymbol{e}_y, \tag{3.32}$$

$$\boldsymbol{n}_0 = -\sin(s)\boldsymbol{e}_x + \cos(s)\boldsymbol{e}_y. \tag{3.33}$$

Note that $\boldsymbol{t}_0' = \boldsymbol{n}_0$, $\boldsymbol{n}_0' = -\boldsymbol{t}_0$ and the undeformed ring is parametrized by $\boldsymbol{r}_0 = -\boldsymbol{n}_0$.

We denote the displacements in the normal and tangential directions from the initial shape by $u(s,t)$ and $v(s,t)$, respectively. Note that these displacements are not assumed small. The shape of the ring may then be written as

$$\boldsymbol{r} = \boldsymbol{r}_0 + u\boldsymbol{n}_0 + v\boldsymbol{t}_0. \tag{3.34}$$

We introduce the angle $\phi(s,t)$ between the tangent of the deformed state and the tangent of the undeformed state by $\boldsymbol{t} = \cos(\phi)\,\boldsymbol{t}_0 + \sin(\phi)\,\boldsymbol{n}_0$. Taking the derivative of (3.34) gives

$$\boldsymbol{r}' = \boldsymbol{t} = \cos(\phi)\,\boldsymbol{t}_0 + \sin(\phi)\,\boldsymbol{n}_0 = [1 - u + v']\,\boldsymbol{t}_0 + [u' + v]\,\boldsymbol{n}_0. \tag{3.35}$$

Hence, we have:

$$\cos(\phi) = 1 - u + v', \quad \sin(\phi) = u' + v. \tag{3.36}$$

To relate the curvature to the angle ϕ we use $\boldsymbol{t}' = \kappa\boldsymbol{n}$, where $\boldsymbol{n} = -\sin(\phi)\boldsymbol{t}_0 + \cos(\phi)\boldsymbol{n}_0$ so that

$$\kappa = 1 + \phi'. \tag{3.37}$$

We see that the curvature has two components: a contribution, $\kappa_0 = 1$, coming from the fact that the ring is initially curved, and a contribution from the deformation of the ring relative to this initial circular shape. Now taking the derivative of (3.29) with respect to arclength gives

$$\ddot{\boldsymbol{t}} = -\boldsymbol{t}^{(4)} + (\lambda\boldsymbol{t})'' - P\kappa\boldsymbol{t}. \tag{3.38}$$

In the absence of pressure, namely $P = 0$, we recover the equation obtained by (Burchard and Thomas, 2003) for a closed loop elastica. We can resolve equation (3.38) into tangential and normal components giving a complete system of five equations for the five variables $(u, v, \lambda, \kappa, \phi)$ for the shape of an elastic ring subject to a normal pressure P.

$$\cos\phi = 1 - u + \frac{\partial v}{\partial s}, \tag{3.39}$$

$$\sin\phi = \frac{\partial u}{\partial s} + v, \tag{3.40}$$

$$\kappa = 1 + \frac{\partial \phi}{\partial s}, \tag{3.41}$$

$$\frac{\partial^2\phi}{\partial t^2} = -\left(\frac{\partial^3\kappa}{\partial s^3} - 6\kappa^2\frac{\partial\kappa}{\partial s}\right) + 2\frac{\partial\lambda}{\partial s}\kappa + \lambda\frac{\partial\kappa}{\partial s} \tag{3.42}$$

$$\left(\frac{\partial\phi}{\partial t}\right)^2 = \left[\kappa^4 - 3\left(\frac{\partial\kappa}{\partial s}\right)^2 - 4\kappa\frac{\partial^2\kappa}{\partial s^2}\right] - \frac{\partial^2\lambda}{\partial s^2} + \lambda\kappa^2 + P\kappa. \tag{3.43}$$

We now make use of the formulation presented in eqns (3.39–3.43) to perform a linear stability analysis of the problem; this is followed by a multiple scales analysis that allows us to examine the development of the instability beyond infinitesimal deformations (linear stability).

3.4.1 Linear stability analysis

We begin by noting that the system (3.39)–(3.43) admits as a solution the undeformed circle:, $v_0 = u_0 = \phi_0 = 0$, $\kappa_0 = 1$, provided that $\lambda_0 = -P - 1$. Physically, this corresponds to the ring having an internal compressive force, $\lambda_0 = -P - 1$, which, combined with its initial curvature, balances the external pressure (via Laplace's law). Our first question is the to determine the stability of this equilibrium state. Letting $u = u_0 + \epsilon u_1$, $v = v_0 + \epsilon v_1$, $\phi = \phi_0 + \epsilon\phi_1$, $\kappa = \kappa_0 + \epsilon\kappa_1$, $\lambda = \lambda_0 + \epsilon\lambda_1$, with $\epsilon \ll 1$ arbitrary, we expand (3.39–3.43) to first order in ϵ to obtain:

$$\frac{\partial v_1}{\partial s} = u_1, \tag{3.44}$$

$$\phi_1 = v_1 + \frac{\partial u_1}{\partial s}, \tag{3.45}$$

$$\kappa_1 = \frac{\partial \phi_1}{\partial s}, \tag{3.46}$$

$$\frac{\partial^2 \phi_1}{\partial t^2} = (5 - P)\frac{\partial \kappa_1}{\partial s} + 2\frac{\partial \lambda_1}{\partial s} - \frac{\partial^3 \kappa_1}{\partial s^3}, \tag{3.47}$$

$$0 = (P - 2)\kappa_1 + \lambda_1 + 4\frac{\partial^2 \kappa_1}{\partial s^2} + \frac{\partial^2 \lambda_1}{\partial s^2}. \tag{3.48}$$

Seeking solutions of the form $u_1 = a_1 \exp(\sigma t + \mathrm{i}n\theta)$, $v_1 = b_1 \exp(\sigma t + \mathrm{i}n\theta)$, $\kappa_1 = c_1 \exp(\sigma t + \mathrm{i}n\theta)$, $\phi_1 = d_1 \exp(\sigma t + \mathrm{i}n\theta)$, $\lambda_1 = e_1 \exp(\sigma t + \mathrm{i}n\theta)$, we obtain a homogeneous linear system that has a non-trivial solution if, and only if, the associated determinant vanishes. This happens when

$$\sigma^2 = \frac{n^2(n^2 - 1)}{n^2 + 1}\left[P - (n^2 - 1)\right]. \tag{3.49}$$

This dispersion relation may be recovered from that obtained previously by Wah (1970) if one neglects rotational inertia in their formulation (corresponding to the limit in which their parameter $\mu \propto a^2/A_\times \to \infty$). We also note that if $P = 0$ then σ^2 is negative so that σ is imaginary; the modes oscillate with a frequency given by the imaginary part of σ, in which case (3.49) reproduces a result first obtained by Hoppe (1871). However, in the following we will derive a relation between the fastest growing mode, n and the applied pressure, P, (which will be relevant for the observed mode); this has not been considered by neither Wah (1970) nor Hoppe (1871).

Indeed our main interest lies in the features of instability that may be observed with positive external pressure, $P > 0$. In this regard, note that $\sigma = 0$ when $P = p_n = n^2 - 1$, giving another perspective on the n^{th} static buckling load of a ring under normal pressure, (Flaherty *et al.*, 1972; Tadjbakhsh and Odeh, 1967). For a given $P > 0$, all modes with $n \leq (P+1)^{1/2}$ are unstable. However, the mode that is expected to be most relevant in the development of instability from arbitrary initial conditions is the most unstable mode (the mode with the largest value of σ) for a given P. Since the mode number n is an integer, a particular n will be the most unstable mode number for a range of pressures as shown in fig. 3.5 (see red dots). This value agrees well with the mode number observed in numerical simulations[1] (blue dots in fig. 3.5). An alternative, if approximate, approach is to treat n as a continuous variable and obtain the value of n that maximizes σ in (3.49) using standard methods. This calculation reveals that the most unstable mode, n_c, is a solution of

$$P = \frac{(n_c^2 - 1)(2n_c^4 + 3n_c^2 - 1)}{n_c^4 + 2n_c^2 - 1}. \tag{3.50}$$

The prediction, (3.50), gives a very good account of both numerical results (see fig. 3.5), and experimental data (see fig 3.6). For $P \gg 1$, we find $n_c \sim (P/2)^{1/2}$. Note further that this result is precisely that obtained by letting $L = 2\pi a$ and $\mathcal{F} = pa$ in (3.3): for large mode numbers (large dimensionless pressures) the most important role of the ring's curvature is to convert the externally applied pressure P into an in-plane compression $\lambda = -(P+1)$ within the ring (corresponding to $\mathcal{F}$ in the heuristic analysis of §3.2).

3.4.2 Weakly nonlinear analysis

The predictions of the linear stability analysis hold only for early times, $t \ll 1$. As the amplitude of the perturbation to the circular state grows, various nonlinear terms compete with the exponentially growing terms found by solving the linear system; eventually, these nonlinearities can no longer be ignored. As a simple illustration of the importance of nonlinear effects, note that the linear theory predicts that the area enclosed by the ring is constant to leading order: $A(t) \approx \frac{1}{2}\int_0^{2\pi}(1-u)^2\,\mathrm{d}s = \pi + \mathcal{O}(\epsilon^2)$. Moreover, if one naively calculates the correction at $\mathcal{O}(\epsilon^2)$ using the linear expansion, one finds that the area enclosed should increase with time, in clear contradiction

[1]Note that the numerically determined mode number is determined from the simulations at the point at which the instability is first visible in the shape. For large n this appears to introduce an error in n of 1, perhaps because one lobe disappears before instability has become numerically observable

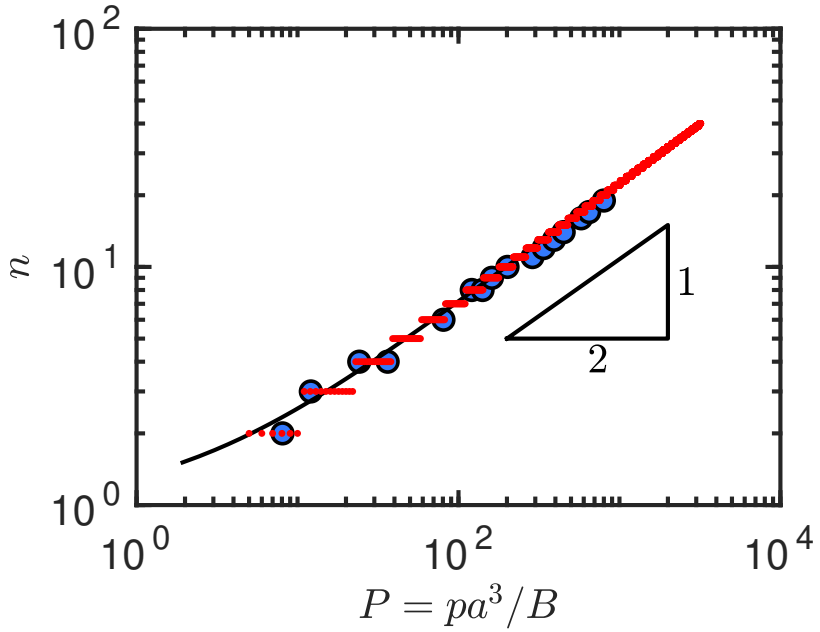

Figure 3.5: The mode number n selected for different imposed external pressures, P: large blue dots correspond to the mode observed in numerical solutions of the full system (3.6)–(3.10). The mode number observed numerically agrees well with the most unstable (integer) mode predicted from a linear stability analysis (small red dots). This analytical result is itself well approximated by the continuous prediction (3.50) (solid black curve) in which n is treated as a continuous variable, while for $P \gg 1$ all approaches tend to the simple scaling $n_c \sim (P/2)^{1/2}$, which is shown as the dashed line.

to the numerical results of fig. 3.4 and experimental results of Box *et al.* (2020). This erroneous prediction is obviously a result of the inconsistency of using a result determined at $\mathcal{O}(\epsilon)$ to make predictions about a correction at $\mathcal{O}(\epsilon^2)$.

To go beyond the linear theory we perform a weakly nonlinear analysis. From (3.49), we see that as the external pressure increases, the ring remains stable as long as $\sigma^2 \leq 0$ for all $n \geq 0$. Therefore the ring is stable only when $P \leq p_n$ for all $n \geq 2$. We note that $p_2 = 3$ is the first critical pressure above which the circular solution of the ring becomes unstable (Tadjbakhsh and Odeh, 1967). We are interested in the dynamic evolution of a critical mode n when the imposed pressure slightly exceeds the critical pressure p_n. To find this evolution, we introduce $\epsilon = \sqrt{P - p_n} \ll 1$ as a small parameter measuring how far the pressure is above the critical pressure for a given mode. Therefore, we introduce $P = n^2 - 1 + \epsilon^2$ in the equations that now depend explicitly on ϵ. Next, we expand all variables to third order in ϵ. For example, we write $u = u_0 + \epsilon u_1 + \epsilon^2 u_2 + \epsilon^3 u_3 + \mathcal{O}(\epsilon^4)$ with analogous expansions for the other variables v, κ, ϕ and λ. These expansions are substituted into (3.39)-(3.43) and the

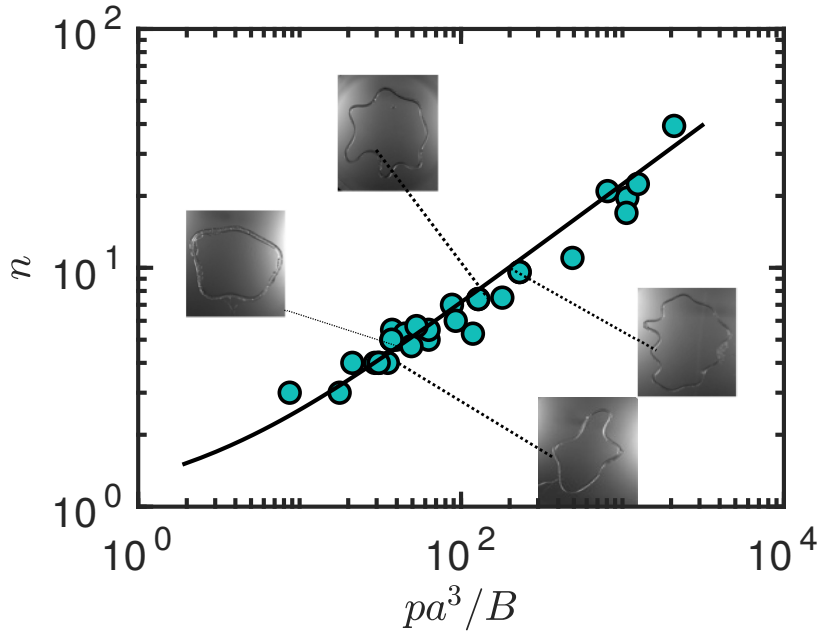

Figure 3.6: Experimentally observed mode numbers for dynamic buckling in a circular geometry. Experimental results for an elastic ring (points), together with the theoretical prediction found from the linear stability analysis of (3.50) (solid curve). Reprinted figure with permission from F. Box, O. Kodio, D. O'Kiely, V. Cantelli, A. Goriely and D. Vella (2020). 'Dynamic Buckling of an Elastic Ring in a Soap Film'. *Physical Review Letters* 124.19. DOI: `10.1103/physrevlett.124.198003`. Copyright 2020 by the American Physical Society.

resulting hierarchy of linear systems can be solved. This calculation is performed using MATHEMATICA.

At $\mathcal{O}(\epsilon)$, the solution is given by:

$$u_1 = \alpha_1 \sin(ns), \quad v_1 = -\frac{\alpha_1}{n}\cos(ns), \tag{3.51}$$

$$\kappa_1 = -\alpha_1\left(n^2-1\right)\sin(ns), \quad \phi_1 = \frac{\alpha_1\left(n^2-1\right)}{n}\cos(ns), \tag{3.52}$$

$$\lambda_1 = \frac{\alpha_1\left(n^2-1\right)\left(4n^2-P+2\right)}{n^2+1}\sin(ns), \tag{3.53}$$

where we have an arbitrary amplitude $\alpha_1(t)$, which depends on the long time scale.

At $\mathcal{O}(\epsilon^2)$, the solution is given by:

$$u_2 = \frac{\alpha_1^2\left(n^2-1\right)^2}{4n^2}, \quad v_2 = -\frac{\alpha_1^2\left(n^2-1\right)^2\sin(2ns)}{8n^3}, \tag{3.54}$$

$$\kappa_2 = -\frac{\alpha_1^2\left(n^2-1\right)^2\cos(2ns)}{4n^2}, \quad \phi_2 = -\frac{\alpha_1^2\left(n^2-1\right)^2\sin(2ns)}{8n^3}, \tag{3.55}$$

$$\lambda_2 = \frac{3\alpha_1^2\left(n^4-1\right)^2\cos(2ns)}{4n^2\left(n^2+1\right)}. \tag{3.56}$$

Note that in the above expressions the $\mathcal{O}(\epsilon^2)$ radial displacement, u_2, is uniform, independent of arclength s. At second order, therefore, the ring moves uniformly inwards, as is observed in the numerical simulations (Fig. 3.4).

The value of the amplitude α_1 as a function of time is determined by a multiple-time expansion to derive the so-called amplitude equation. This equation is obtained as a compatibility condition for the existence of bounded solutions (using the Fredholm Alternative) for the linear systems to third order, (see for example Lange and Newell, 1971) and Goriely *et al.* (2001). This condition reads

$$\frac{\mathrm{d}^2\alpha}{\mathrm{d}t^2} = \sigma^2\alpha - \mu\alpha^3, \tag{3.57}$$

with

$$\alpha = \epsilon\alpha_1, \quad \sigma^2 = \frac{n^2(n^2-1)}{n^2+1}(P-p_n), \quad \mu = \frac{3}{8}\frac{(n^2-1)^4}{n^2+1}. \tag{3.58}$$

If we neglect the non-linear term, $\mu\alpha^3$, we recover the results of the linear stability theory, as expected, since (3.58) gives the same linear growth rate σ as (3.49).

Equation (3.57) can be solved in terms of Jacobi elliptic functions, but that approach does not provide any particular insight; we therefore solve (3.57) numerically.

Since we may readily compute the amplitude α as a function of time, we are now in a position to compare directly the numerical solutions of the full system with the post-bifurcation solution to second-order. We study several aspects of the problem in turn:

Shape We compare the shape obtained by numerically solving the governing equations with that predicted by the multiple-scale solutions. To do this, we choose an initial magnitude of numerical noise (here $\alpha(0) = 0.01$) and then find the evolution of the amplitude by solving (3.57). Once this amplitude $\alpha(t)$ is known we use (3.54) to determine the corresponding profile. The result is shown in fig. 3.7 together with the shape from the full numerical solution, and shows very good agreement for $P = 3.5$ and $P = 8.7$, which correspond to the $n = 2$ and $n = 3$ modes, respectively. (Though we are only interested in the dynamic at moderate time after the onset of the buckling, during which the weakly nonlinear analysis makes sense; however, we note that for σ^2 and $\mu > 0$, the solution of the amplitude equation, (3.57), will oscillate for late times).

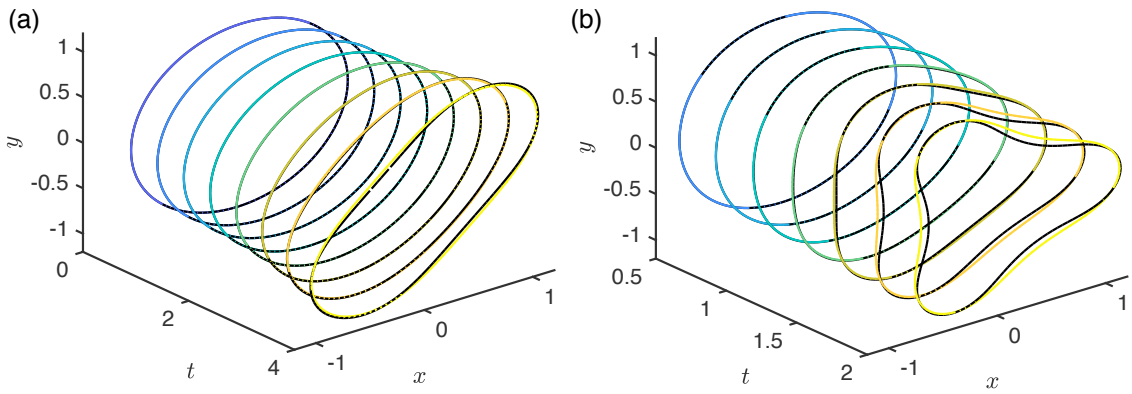

Figure 3.7: Comparison between the numerical solution (solid curves) and the weakly nonlinear solution (dotted curves) for (a) $P = 3.5$, corresponding to mode 2, and (b) $P = 8.7$, corresponding to mode 3. Shapes are shown at instants of time that start with $t = 0.5$ and increase at constant intervals of time δt; in (a) $\delta t = 0.5$ while in (b) $\delta t = 0.25$. Reprinted figure with permission from O. Kodio, A. Goriely and D. Vella (2020). 'Dynamic buckling of an inextensible elastic ring: Linear and nonlinear analyses'. *Physical Review E* 101.5. DOI: 10.1103/physreve.101.053002. Copyright 2020 by the American Physical Society.

Amplitude We compare the amplitude $\alpha(t)$ with that obtained from the numerical simulations. To do so, we compute numerically the function $u(s,t)$ and extract the amplitude of its first Fourier component:

$$\alpha_{\text{num}}(t) = \frac{1}{\pi}\left[\left(\int_0^{2\pi} u(s,t)\sin ns\,\mathrm{d}s\right)^2 + \left(\int_0^{2\pi} u(s,t)\cos ns\,\mathrm{d}s\right)^2\right]^{1/2}. \tag{3.59}$$

We see from Fig. 3.8 that the amplitude equation captures quantitatively the evolution of the $n = 2$ mode but only qualitatively captures the evolution of the $n = 3$ mode.

Area From the post-bifurcation solution to second order, we can compute the area of the ring including a perturbation of mode number n. We find that this area is

$$A_n(t) = \pi - \frac{(n^2-1)\pi}{2}\alpha(t)^2. \tag{3.60}$$

The change in area, $\Delta A(t) = A(0) - A_n(t) = \pi - A_n(t)$ and the relative change in area is

$$\frac{\Delta A(t)}{A(0)} = 1 - \frac{A_n}{\pi} = \frac{n^2-1}{2}\alpha(t)^2. \tag{3.61}$$

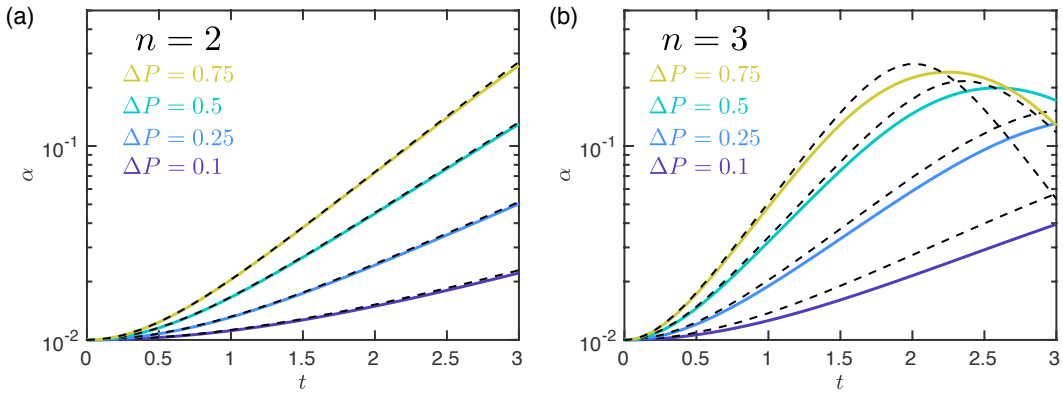

Figure 3.8: Evolution of the amplitude $\alpha(t)$ determined as a function of time from full numerical simulations, using (3.59) (solid curves) together the corresponding prediction of the amplitude equation (3.57) (dashed curves). Results are shown for (a) $n = 2$ and (b) $n = 3$ with pressures $\Delta P = P - p_c(n) = 0.1, 0.25, 0.5$ and 0.75 coded by colour, as in the legend. (Recall that the critical pressure at which mode n becomes unstable is $p_c(n) = n^2 - 1$.) Reprinted figures with permission from O. Kodio, A. Goriely and D. Vella (2020). 'Dynamic buckling of an inextensible elastic ring: Linear and nonlinear analyses'. *Physical Review E* 101.5. DOI: `10.1103/physreve.101.053002`. Copyright 2020 by the American Physical Society.

The plots in Fig. 3.9a show that the prediction of (3.61) is in good agreement with the detailed numerical simulations of the full problem for early times, while the plots in Fig. 3.9b show that at early times the relative change in area grows according to $\Delta A/A(0) \propto \exp(2\sigma t)$ with σ the growth rate of the linear instability. Finally, Fig. 3.9c shows that the error in the area change occurs at higher order in α than $\mathcal{O}(\alpha^2)$, confirming that the weakly nonlinear analysis presented here is correct to this order.

To further test our predictions we plot in fig. 3.10 the evolution of the experimentally measured relative area change reported by Box *et al.* (2020), together with numerical results and the prediction $\Delta A/A(0) \propto \exp(2\sigma t)$. Both experiments and numerical results show the growth rate expected from (3.60) at very early times, with higher pressures corresponding to faster growing instability and the earlier onset of nonlinear effects (signified by significant deviations from (3.60)).

Compressive force λ The amplitude equation can also be used to study the evolution of the compressive force λ within the ring: the predicted behaviour of $\lambda(s, t)$ can readily be computed once the amplitude equation for $\alpha(t)$, eqn(3.57), is solved numerically.

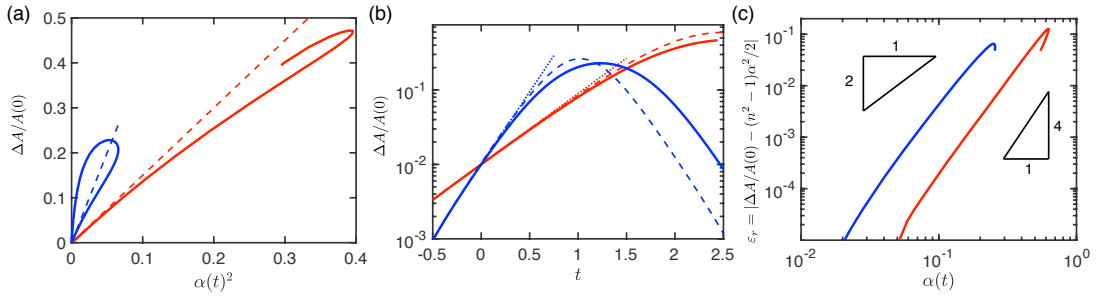

Figure 3.9: Comparison of the change in area enclosed by the ring computed numerically and that predicted from the weakly nonlinear analysis presented here. Throughout, results are shown for the $P = 3.5$, corresponding to $n = 2$, (red curves) and $P = 8.7$, corresponding to $n = 3$, (blue curves). (a) The relative area change, $\Delta A/A(0) = 1 - A(t)/A_0$ as a function of $\alpha(t)^2$ shows that for early times the results confirm the linear behaviour expected from (3.61), which become the dashed lines in this plot. Numerical results are shown as solid curves, together with the prediction of the weakly nonlinear analysis, (3.61) (dashed curves). (b) Plotting $\Delta A/A(0)$ as a function of t on semi-logarithmic axes shows that at early times the growth is exponential with growth rate 2σ (and σ as predicted from the linear analysis) — $\Delta A/A(0) \propto \exp(2\sigma t)$ as shown by the dotted lines. (c) A plot of the absolute numerical error, $\varepsilon_r = |\Delta A/A(0) - (n^2-1)\alpha^2/2|$, as a function of $\alpha(t)$ shows that this error occurs at higher order in $\alpha(t)$ — most likely $\varepsilon_r(t) \propto \alpha(t)^4$. Reprinted figures with permission from O. Kodio, A. Goriely and D. Vella (2020). 'Dynamic buckling of an inextensible elastic ring: Linear and nonlinear analyses'. *Physical Review E* 101.5. DOI: `10.1103/physreve.101.053002`. Copyright 2020 by the American Physical Society.

The comparison between the prediction of the weakly nonlinear analysis and full numerical simulations is shown in fig. 3.11. As with other variables, the comparison between numerics and the weakly nonlinear analysis is very good, particularly at early times. However, this plot of $\lambda(s,t)$ reveals two features that are not so readily observed in other variables: the oscillations in $\lambda(s,t)$ for a fixed time t are not up-down symmetric and, in particular, the crest of these oscillations splits in two, showing the importance of a higher frequency oscillation in the arclength s. Both of these features can be understood by observing from (3.54) that the prefactor of $\lambda_2 \sim n^4\alpha_1^2$ while (3.51) shows that the prefactor of $\lambda_1 \sim n^2\alpha_1$. As a result, λ_2 is able to compete with λ_1 despite being strictly at higher order in α: the $\cos(2ns)$ term in the expansion of $\lambda(s,t)$ can compete with the $\sin(ns)$ term, breaking up-down symmetry and leading to the splitting of the crests. This is not so apparent in other variables, since the higher order terms remain strictly sub-dominant for longer; for example, $\kappa_2 \sim \alpha_1^2 n^2$ while $\kappa_1 \sim \alpha_1 n^2$.

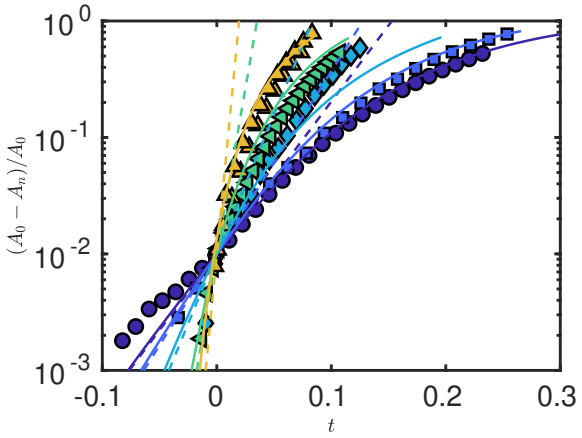

Figure 3.10: The growth rate of instability in an elastic ring is observed via the relative change of area, $\Delta A/A_0$, as a function of dimensionless time. Experimental data (points from Box *et al.* (2020)) and results of numerical simulations (solid curves) show that $\Delta A/A_0 \propto \exp(2\sigma_{\max} t)$ at early times (dashed lines), with $\sigma_{\max}$ determined from the linear stability analysis. Here different values of the dimensionless pressure $P = pa^3/B$ are shown by different symbols as follows: $P = 31$ ($\circ$), 37 ($\square$), 56 ($\diamond$), 132 ($\square$), 238 ($\triangle$). In each plot, the $\exp(2\sigma_{\max} t)$ behaviour is plotted based on the appropriate value of $\sigma_{\max}(P)$ and the origin of time is shifted so that $\Delta A(t = 0)/A_0 = 1\%$. (Two runs are shown for $P = 238$, to give an indication of the systematic error.)

The appearance of second-order variables with frequency $2n$ might suggest this as a precursor of a secondary bifurcation with frequency doubling. However, we note that, in fact, our numerical simulations show that the dynamic evolution of the shape does not reveal frequency doubling, but rather that lobes progressively disappear with time — the buckles coarsen rather than splitting. This is shown in the evolution of the shapes obtained with $P = 256$ (shown in the last panel of Fig. 3.4), where several events in which two crests merge into a single crest are shown. We hypothesize that this merger occurs via the 'snap-through' of the internal element, as observed in a simple elastic arch Pandey *et al.* (2014).

3.5 Effect of ramping

We use numerical simulations to investigate the effect of increasing the compressive force $\mathcal{F}$ dynamically in equation (3.1). The maximum growth rate from (3.2), $\sigma_{\max} = [\mathcal{F}^2/(4B\rho h)]^{1/2}$, shows that the intrinsic time scale of instability increases with applied load, so one might expect that at early times (small load) a low mode number would be excited, but grow slowly — by the time this mode had grown appreciably, the compression would have increased so that the instantaneously fastest growing mode

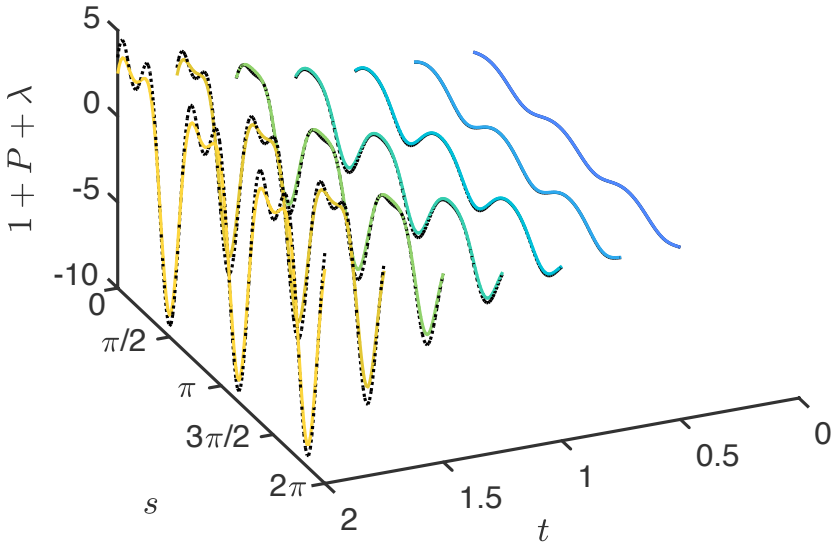

Figure 3.11: The evolution of the compressive stress within the ring, $\lambda(s,t)$, for an applied pressure $P = 8.7$, corresponding to mode 3 (as seen in Fig. 3.7b). The results of the numerical simulations (solid curves) agree well with the prediction of the multiple scale analysis (dotted black curves). Note, in particular, that at times $t = \mathcal{O}(1)$ the spatial oscillations with arclength s are not up-down symmetric and that the peaks have a noticeable splitting. These two effects are purely nonlinear effects and are predicted well by the weakly nonlinear analysis presented here. (Results are shown for $1/2 \leq t \leq 2$ at intervals of $\delta t = 1/4$, with colour indicating elapsed time.) Reprinted figure with permission from O. Kodio, A. Goriely and D. Vella (2020). 'Dynamic buckling of an inextensible elastic ring: Linear and nonlinear analyses'. *Physical Review E* 101.5. DOI: `10.1103/physreve.101.053002`. Copyright 2020 by the American Physical Society.

would be higher, and evolve faster, allowing it to overtake the earlier lower mode, ultimately reaching the nonlinear regime sooner. To test this possibility, we perform numerical simulations of the one-dimensional beam equation, (3.1), for a beam of length $L = 2\pi a$ with pinned boundary conditions, $w(\pm L/2, t) = w_{xx}(\pm L/2, t) = 0$), and a Gaussian initial condition, subject to a time-dependent dimensionless compressive force

$$\mathcal{F}(t) = \mathcal{F}_0 t^\beta, \tag{3.62}$$

We use the ramping exponent β as a parameter to describe the rate of loading: $\beta \to 0$ corresponds to the step-function loading assumed so far, while $\beta = 1$ corresponds to a constant loading rate. Numerical results for the mode number observed at $t = 1$ are shown in fig. 3.12 for a range of dimensionless maximum compressions $\mathcal{F}_0$ as a function of β. Since each value of $\mathcal{F}_0$ would give a different mode number if imposed as a step function ($\beta \to 0$) we normalize results by $n_{\max} = (\mathcal{F}_0/2)^{1/2}$ and

observe a good collapse, at least for small β.

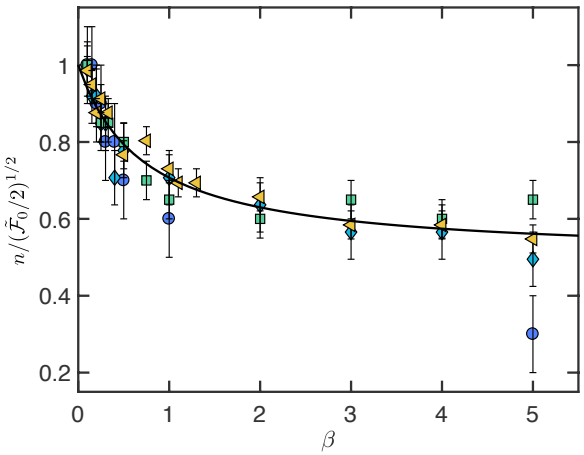

Figure 3.12: Mode numbers observed with different ramping exponents β and maximum loads $\mathcal{F}$. Here points represent the numerically observed mode number at time $t = 1$ for a loading of the form (3.62) with different exponents β and different maximum loading pressures: $\mathcal{F} = 200$ ($\circ$), 400 ($\diamond$), 800 ($\square$), 1500 ($\triangleleft$). The solid curve shows the prediction from balancing time scales, (3.64), with $c = 0.25$ (chosen to give a reasonable description of the data). Error bars denote the uncertainty associated with the discreteness of n.

To understand this behaviour qualitatively, we seek to estimate the dimensionless time, t_{form}, at which the pattern observed at $t = 1$ is formed; we do this by requiring the argument of the exponential in our linear perturbation at t_{form}, $\sigma[\mathcal{F}(t_{\text{form}})] \cdot t_{\text{form}}$, be comparable to that at the time of observation, $\sigma(\mathcal{F}_0) \cdot 1$, i.e.

$$(\mathcal{F}_0 t_{\text{form}}^{\beta}) \cdot t_{\text{form}} \sim \mathcal{F}_0. \tag{3.63}$$

Assuming a constant of proportionality c we find $t_{\text{form}} \sim c^{1/(\beta+1)}$ and, using $n \sim [\mathcal{F}(t_{\text{form}})]^{1/2}$,

$$n \sim c^{\beta/[2(\beta+1)]}. \tag{3.64}$$

The general form of this prediction is in reasonable agreement with the observations from numerical simulations (solid curve in fig. 3.12), with $c = 0.25$ chosen to give a reasonable description of the numerical results.

3.6 Conclusion

We have discussed both linear and weakly nonlinear analyses of the dynamic buckling of an elastic ring subject to a suddenly imposed external pressure, p. Returning to our initial discussion of the dynamic buckling of a beam under a compressive force $\mathcal{F}$,

we speculated that the same argument might hold for a ring under pressure $p = \mathcal{F}/a$ and, further, that this is the most important effect of the ring's curvature. This analogy is enough to reproduce the main results of the linear stability analysis for sufficiently large pressures, namely that

$$n_c \approx \left(\frac{pa^3}{2B}\right)^{1/2}, \tag{3.65}$$

which grows with dimensional growth rate

$$\sigma_{\max} \approx \frac{1}{2}\frac{pa}{(\rho A_\times B)^{1/2}}. \tag{3.66}$$

Detailed calculations show small variations from these results at moderate P (defined to be such that $n_c \leq 5$).

We note that while inertia is required to observe buckling at a high mode number, (3.65) shows that the mode number selected is independent of the inertia of the ring, $\rho A_\times$. Rather the inertia of the ring sets the time scale for the growth of instability, as shown in (3.66). The apparent contradiction that inertia is required to observe a high mode number but is not involved in the selection of a mode number is resolved by varying the loading rate to be below that in (3.66).

While a linear stability analysis is sufficient to understand the early stages of the dynamics, it does not provide any insight into how the instability develops further. In particular, the linear stability analysis shows that the area enclosed by the loop does not change to leading order; moreover, if one attempts to use its results at higher order, one comes to the erroneous conclusion that the enclosed area *increases* as instability proceeds. Therefore, we performed a weakly nonlinear analysis that allows us to show that the relative change in area $\Delta A/A(0)$ grows exponentially in time, with growth rate $2\sigma_{\max}$. The weakly nonlinear analysis is able to explain other features of our numerical simulations, including an apparent frequency doubling of the compressive force λ within the ring. While this might be expected to lead to an increase in the mode number with time, we note that our numerical simulations show that crests tend to merge with time, presumably due to the increase in confinement that they experience. The time scale of this coarsening remains to be understood.

Finally, we note that the ring geometry we have studied here may be a more promising paradigm within which to understand dynamic buckling instabilities in soft materials: while the uniaxial compression of a rod has often been studied (see Gladden *et al.*, 2005, for example), it can be difficult to impose a known force experimentally and the resulting instability is sensitive to the imposed boundary conditions. The

circular symmetry of the ring problem renders the latter issue irrelevant while our analysis has shown that, up to the instability, the ring curvature translates the normal force given by the applied pressure into a uniform in-plane compression.

3.A Numerical scheme: Inextensibility constraint

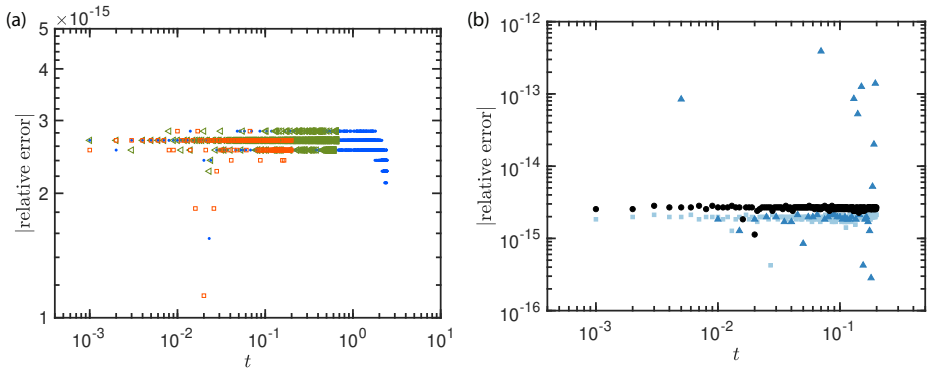

Figure 3.13: Evolution of the relative error in the total arc length of the ring, $\ell(t_j)$ (see (3.67)), in the numerical simulations presented in fig. 3.4. Here, we plot $|(\ell(t_j) - 2\pi)/2\pi|$ as a function of time. (a) With fixed resolutions, $\Delta t = 10^{-3}$ and $N = 256$: results are shown for $P = 8$ (dots), $P = 32$ (triangles) and $P = 128$ (squares). (b) Simulations for fixed pressure, $P = 128$, with different spatial and temporal resolutions: results with $N = 128$ and $\Delta t = 5 \times 10^{-3}$ (triangles), $N = 128$ and $\Delta t = 10^{-3}$ (squares), $N = 256$ $\Delta t = 10^{-3}$(dots). In all these simulations, the magnitude of the relative error is below 10^{-12}. Reprinted figures with permission from O. Kodio, A. Goriely and D. Vella (2020). 'Dynamic buckling of an inextensible elastic ring: Linear and nonlinear analyses'. *Physical Review E* 101.5. DOI: `10.1103/physreve.101.053002`. Copyright 2020 by the American Physical Society.

Here we discuss the constraint of inextensibility at each time step: we are interested in checking whether the total length of the ring is preserved over time during the integration. Indeed, we note that (3.16)-(3.17) are solved together with the remaining equations (3.18)-(3.23) at each time step. This ensures (in principle) that, at each time step, j, the inextensibility constraints *i.e.* (3.6)-(3.7) are automatically satisfied.

In the following we check the inextensibility constraints for the simulations reported in fig. 3.4. We determine the numerical arc length of the ring as

$$\ell(t_j) = \sum_{i=0}^{N} \left[(x_{i+1}^j - x_i^j)^2 + (y_{i+1}^j - y_i^j)^2 \right]^{1/2}. \tag{3.67}$$

In fig. (3.13), we plot the magnitude of the relative error in the total arc length of the ring, $|(\ell(t_j) - 2\pi)/2\pi|$, as a function of time for different values of pressures and spatio-temporal resolutions. Fig. (3.13a) shows simulations for different values of pressures, $P = 8, 32, 128$, at fixed value of the time step $\Delta t = 10^{-3}$. In contrast, Fig. (3.13b) shows the relative error for a fixed pressure $P = 128$, for different spatial and temporal resolutions. We see here that the ring maintains its length over time as guaranteed by our numerical scheme. The magnitude of the relative error of the total length for the simulations reported in fig. 3.4 is about 10^{-12}.

Finally, we discuss two limitations of our numerical scheme. First, the initial conditions we used, *i.e.* (3.24), contains a random noise at each spatial grid point. This means that the initial condition is mesh dependent. However during the simulations reported in fig. 3.4 we noticed that, at the first time step, the solutions initially converge to a circular ring shape, and then the fastest growing modes start emerging. This suggests that the observed instability is an intrinsic feature of the solutions of (3.6) -(3.10). Second, it is to be noted that since we have used a BDF2 (Backward Differential Formula) in (3.15) it follows that our scheme will be dissipative, and only accurate at $\mathcal{O}(\Delta t^2)$. This limitation implies that the solutions reported in this chapter cannot be expected to be accurate at very late time. Such limitation may be overcome by using a symplectic integrator or, in general, a geometric integrator.

Chapter 4

Dynamics of an elastic beam on a viscous layer

4.1 Introduction

The principal obstacle to a more detailed study of buckle coarsening in the previous two chapters was the presence of two time derivatives, which come from the crucial role of inertia. In this chapter, we consider a problem in which the coarsening of elastic wrinkles is controlled by viscous dissipation. This problem arises from experiments by Vandeparre *et al.* (2010) in which a Titanium-Polystyrene bilayer was heated above the glass transition temperature of Polystyrene. The different thermal expansion coefficients lead to relative compression of the Titanium which then wrinkles on the Polystyrene layer. As the experimental images in fig. 4.1 show, the wavelength of the wrinkles increases dynamically. As a model problem, we study the dynamic

Figure 4.1: Wrinkling and Coarsening of Titanium-Polystyrene bilayer: This illustrates coarsening as the images are shown for 1, 2 and 30 minutes at a temperature of 130°C from left to right respectively. The scale bar corresponds to $20\mu m$. Republished with permission of The Royal Society of Chemistry. Images from H. Vandeparre, S. Gabriele, F. Brau, C. Gay, K. K. Parker and P. Damman (2010). 'Hierarchical wrinkling patterns'. *Soft Matter* 6.22. DOI: 10.1039/c0sm00394h; permission conveyed through Copyright Clearance Center, Inc.

coarsening of wrinkles in an elastic sheet that is compressed while lying on a thin layer of viscous liquid. When the ends of the sheet are instantaneously brought together by a small distance, viscous resistance initially prevents the sheet from adopting a globally buckled shape (as would be the case in a purely elastic system). Instead, the sheet accommodates the compression by wrinkling as shown in 4.2. Previous scaling arguments by Vandeparre *et al.* (2010) suggested that a balance between the sheet's bending stiffness and viscous effects lead to a wrinkle wavelength λ that increases with time t according to $\lambda \propto t^{1/6}$. We show that taking proper account of the compression constraint leads to a logarithmic correction of this result, $\lambda \propto (t/\log t)^{1/6}$.

The essential mechanism behind coarsening is illustrated in fig. 4.2: an inextensible elastic sheet sits on a thin layer of a viscous liquid, of thickness h_0 (fig. 4.2a). When its two ends are brought together by a fixed distance δ (the end-shortening), the sheet buckles to maintain its natural length. However, adopting the Euler-buckling profile (fig. 4.2c) would require a great deal of viscous fluid to be brought into the system, which cannot happen instantaneously. Instead, the sheet adopts a wrinkled profile (fig. 4.2b), allowing the length constraint to be met with only minimal movement of viscous liquid. Over time, these wrinkles coarsen, until eventually the system does indeed adopt the expected Euler-buckling profile. Our aim in this chapter is to go beyond the scaling analysis presented previously (Leocmach *et al.*, 2015; Vandeparre *et al.*, 2010) and to account for the global nature of the constraint appropriately.

4.2 Theoretical formulation

We assume that the typical thickness of the viscous film, h_0, is small compared with the horizontal extent of the system, ℓ. Assuming also that the horizontal length scale on which the film thickness varies is large compared with the thickness (*i.e.* the angle of deflection of the beam is small), we may use the lubrication approximation (Leal, 2007) to describe the film thickness profile; in particular, assuming no-slip the solid surfaces the evolution of the film thickness $h(x,t)$ is related to the pressure profile within the film, $p(x,t)$, by Reynolds' equation (Leal, 2007)

$$\frac{\partial h}{\partial t} = \frac{1}{12\mu}\frac{\partial}{\partial x}\left(h^3\frac{\partial p}{\partial x}\right), \tag{4.1}$$

where μ is the viscosity of the liquid within the film. Assuming that motion occurs quickly enough that the beam is instantaneously in equilibrium (*i.e.* neglecting inertia) the pressure in the film is given by the beam equation (Landau and Lifshitz, 1970)

$$p = B\frac{\partial^4 h}{\partial x^4} + P\frac{\partial^2 h}{\partial x^2}, \tag{4.2}$$

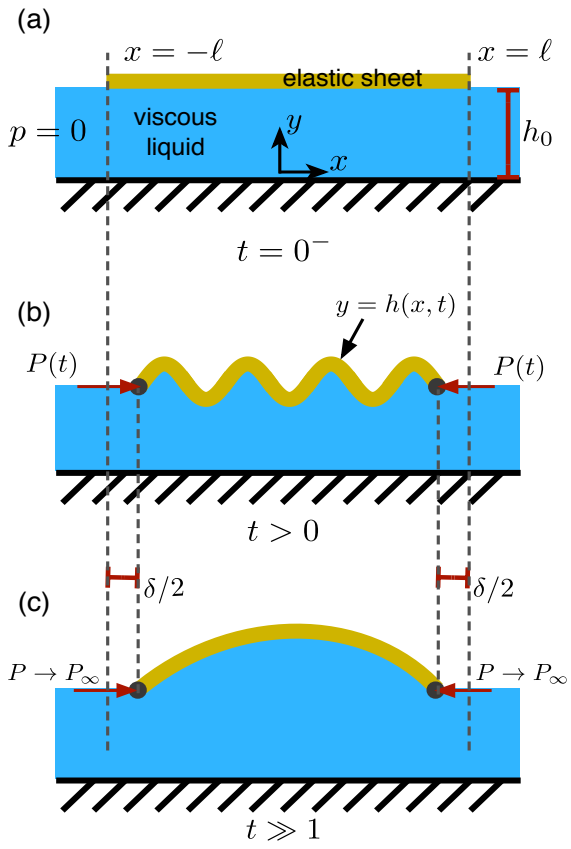

Figure 4.2: The dynamic wrinkling of an inextensible elastic sheet on a thin viscous film. (a) Initially an elastic sheet of length 2ℓ is supported on a viscous film of thickness h_0. (b) At time $t = 0^+$ an end-shortening $\delta/2$ is imposed (instantaneously) to each of the two ends, and maintained for all $t > 0$. (The imposed displacement requires a compressive force P, per unit width, to be applied at the ends; P is not known *a priori* and may evolve dynamically.) The sheet accommodates this displacement, while preserving its contour length by buckling. Relatively large amplitude displacements require viscous fluid to be drawn in, which is a slow process. At intermediate times, the sheet adopts a wrinkled profile, with fine wrinkles that coarsen as more liquid is sucked in. (c) Ultimately, the sheet adopts the lowest Euler-buckling mode consistent with the imposed boundary conditions. Reprinted with permission from O. Kodio *et al.* (2017). 'Lubricated wrinkles: Imposed constraints affect the dynamics of wrinkle coarsening'. *Physical Review Fluids* 2.1, p. 014202. DOI: 10.1103/PhysRevFluids.2.014202. Copyright 2017 by the Americal Physical Society.

where $B = Eh_b^3/[12(1-\nu^2)]$, is the bending stiffness of the beam (with E its Young's modulus, h_b its thickness, and ν its Poisson ratio), while P is the compressive force applied at the ends of the beam. The compressive force P is homogeneous, i.e. $P = P(t)$: variations in P with x arise from viscous stresses but are negligible. To see this, we use a horizontal force balance, which gives $\partial P/\partial x = \mu \partial u/\partial y|_{y=h}$ where u is the horizontal velocity in the fluid, with y the vertical coordinate. Since the flow is Poiseuille, we have $\partial P/\partial x \approx (\mathrm{d}p/\mathrm{d}x)h/2 \sim h_0 \Delta p/\ell$, where Δp is the typical hydrodynamic pressure difference over the length of the beam. Hence the typical change in the compressive force within the sheet due to fluid shear stresses is $\Delta P \sim h_0 \Delta p$. The typical pressure change in the viscous film $\Delta p \sim B h_0/\ell_*^4$, so that $\Delta P \sim B h_0^2/\ell_*^4$ (here ℓ_* is a relevant horizontal length scale, which may change during the evolution but will always satisfy $\ell_* \lesssim \ell$). Finally, we note that the balance between the first and second terms on the RHS of (4.2) suggests that $P \sim B/\ell_*^2$, and so we conclude that $\Delta P \sim B h_0^2/\ell_*^4 \ll B/\ell_*^2 \sim P$ by virtue of the thin-layer approximation $h_0/\ell \ll 1$. As a result we conclude that spatial variations in the compressive force P may be neglected, so that $P(x,t) \approx P(t)$. We note that in neglecting spatial variations in P, our approach differs from previous numerical work by Huang and Im

(2006), Huang and Suo (2002) and Im and Huang (2005).

We therefore find that the film thickness is governed by

$$\frac{\partial h}{\partial t} = \frac{B}{12\mu}\frac{\partial}{\partial x}\left[h^3\left(\frac{\partial^5 h}{\partial x^5} + \frac{P}{B}\frac{\partial^3 h}{\partial x^3}\right)\right], \tag{4.3}$$

for $t > 0$, $-\ell < x < \ell$. Our equation (4.3) is different to those studied by Huang and Im (2006) who considered coupled PDEs for the evolution of the in-plane and out-of-the-plane displacements. However, in the absence of compression, $P = 0$, our equation (4.3) reduces to that studied by Flitton and King (2004).

The motion studied here is driven by an imposed end-shortening δ. Assuming that the beam is inextensible which corresponds to an assumption of being sufficiently slender, (Landau and Lifshitz, 1970; Pandey *et al.*, 2014), this end–end compression imposes an integral constraint on the problem. With the approximation of small slopes, this constraint may be written (see, for example Brau *et al.*, 2013)

$$\frac{1}{2}\int_{-\ell}^{\ell}\left(\frac{\partial h}{\partial x}\right)^2 \mathrm{d}x = \delta. \tag{4.4}$$

4.3 Initial and boundary conditions

The problem (4.3) subject to the constraint (4.4) requires an initial condition, $h(x, 0)$, and six boundary conditions. We denote the initial shape of the beam by

$$h(x, t = 0) = f(x), \tag{4.5}$$

for some given function $f(x)$. We also assume that the film thickness is prescribed at the edges, giving the boundary conditions

$$h(x = -\ell, t) = h(x = \ell, t) = h_0. \tag{4.6}$$

Various further boundary conditions are possible for beams (e.g. no shear force, no torque, or clamped). For simplicity, we shall assume that no moment is applied to the beam at its ends (so that h_{xx} vanishes there) and that the pressure is atmospheric (without loss of generality zero) there too; because of the beam equation (4.2), this guarantees that $h_{xxxx} = 0$ at these edges. We therefore have

$$h_{xx}(x = -\ell, t) = h_{xx}(x = \ell, t) = 0, \tag{4.7}$$

$$h_{xxxx}(x = -\ell, t) = h_{xxxx}(x = \ell, t) = 0. \tag{4.8}$$

4.4 Non-dimensionalization

It is natural to scale the film profile h with the value that it takes at the edges, h_0. There is no preferred horizontal length scale, we therefore introduce an arbitrary horizontal scale, x_* (which can be set equal to h_0). This leads to natural time and force scales

$$t_* = \frac{12\mu x_*^6}{Bh_0^3}, \quad P_* = \frac{B}{x_*^2}. \tag{4.9}$$

Introducing dimensionless variables

$$\tilde{t} = t/t_*, \quad \tilde{x} = x/x_*, \quad \tilde{h} = h/h_*, \quad \tilde{P} = P/P_*, \tag{4.10}$$

(and immediately dropping tildes) we find that (4.3) becomes

$$\frac{\partial h}{\partial t} = \frac{\partial}{\partial x}\left[h^3\left(\frac{\partial^5 h}{\partial x^5} + P\frac{\partial^3 h}{\partial x^3}\right)\right], \tag{4.11}$$

for $t > 0$, $-L < x < L$, where $L = \ell/x_*$.

In the problem as currently specified, there are two sources of nonlinearity. The first is the integral constraint corresponding to the imposed end-shortening, (4.4). This nonlinearity arises from the geometry, and so we shall refer to it as the *geometric nonlinearity*. The second source of nonlinearity is the nonlinear permeability that arises from Reynolds' equation, *i.e.* the h^3 term in (4.11); we refer to this as the *hydrodynamic nonlinearity*. In what follows it will be useful for us to be able to isolate the effect of the geometric, rather than hydrodynamic, nonlinearity. To facilitate this, we let $h = 1 + u(x,t)$ so that the leading-order equation for u when $|u| \ll 1$ is a linear PDE, subject to a nonlinear constraint. With this substitution the fully nonlinear problem reads

$$\frac{\partial u}{\partial t} = \frac{\partial}{\partial x}\left(h^3\frac{\partial^5 u}{\partial x^5}\right) + P(t)\frac{\partial}{\partial x}\left(h^3\frac{\partial^3 u}{\partial x^3}\right), \tag{4.12}$$

$$\frac{1}{2}\int_{-L}^{L}\left(\frac{\partial u}{\partial x}\right)^2 \mathrm{d}x = \Delta, \tag{4.13}$$

$$u(x, t=0) = u_0(x), \tag{4.14}$$

$$u(x=-L,t) = u(x=L,t) = 0, \tag{4.15}$$

$$u_{xx}(x=-L,t) = u_{xx}(x=L,t) = 0, \tag{4.16}$$

$$u_{xxxx}(x=-L,t) = u_{xxxx}(x=L,t) = 0. \tag{4.17}$$

Here the dimensionless end-shortening $\Delta = \delta x_*/h_0^2$.

Similarly, the linear problem reads

$$\frac{\partial u}{\partial t} = \frac{\partial^6 u}{\partial x^6} + P(t)\frac{\partial^4 u}{\partial x^3}, \tag{4.18}$$

$$\frac{1}{2}\int_{-L}^{L}\left(\frac{\partial u}{\partial x}\right)^2 \mathrm{d}x = \Delta, \tag{4.19}$$

$$u(x, t=0) = u_0(x), \tag{4.20}$$

$$u(x=-L, t) = u(x=L, t) = 0, \tag{4.21}$$

$$u_{xx}(x=-L, t) = u_{xx}(x=L, t) = 0, \tag{4.22}$$

$$u_{xxxx}(x=-L, t) = u_{xxxx}(x=L, t) = 0. \tag{4.23}$$

4.5 Unconfined evolution

To gain some understanding of the evolution of the film thickness $h(x,t) = 1+u(x,t)$, as described by (4.12) and (4.13), we begin by neglecting the compressive force, *i.e.* we set $P(t) \equiv 0$. For simplicity we consider that the horizontal extent is infinitely large compared to the thickness *i.e.* we set $L = \infty$. For small variations of the film thickness from the uniform value $h_0 = 1$, we have

$$\frac{\partial u}{\partial t} = \frac{\partial^6 u}{\partial x^6}. \tag{4.24}$$

This linear equation has similarity solutions, (Arutkin *et al.*, 2016; Flitton and King, 2004; Tulchinsky and Gat, 2016) in which the horizontal length scale $x \propto t^{1/6}$. We therefore anticipate that the observed wrinkle wavelength should grow with time according to

$$\lambda(t) \sim c\, t^{1/6}, \tag{4.25}$$

where c is a constant prefactor. The scaling relation (4.25) is identical to that given by energy considerations (Vandeparre *et al.*, 2010).

To understand the behaviour of the wavelength properly, however, we need to find the profile of the beam, particularly at intermediate and late times. From this profile we will be able to determine the wavelength λ and, indeed, discuss whether it is appropriate to attribute a wavelength to the profile.

The linearity of (4.24) ensures that the solution $u(x,t)$ may be written as the convolution of the initial condition, $u_0(x)$ with the fundamental solution (Green's function), $g(x,t)$. In the following we are interested in the shape of the fundamental solution $g(x,t)$. To determine this shape, we adopt the following definition of the Fourier Transform:

$$\hat{u}(k,t) = \frac{1}{\sqrt{2\pi}}\int_{-\infty}^{\infty} u(x,t)\mathrm{e}^{-ikx}\,\mathrm{d}x, \tag{4.26}$$

so that the appropriate Inversion Theorem is

$$u(x,t) = \frac{1}{\sqrt{2\pi}} \int_{-\infty}^{\infty} \hat{u}(k,t) \mathrm{e}^{ikx} \, \mathrm{d}k. \tag{4.27}$$

Taking the Fourier transform of equation (4.24) gives

$$\frac{d\hat{u}}{\mathrm{d}t} = -k^6 \hat{u}, \tag{4.28}$$

and integrating with respect to time gives

$$\hat{u}(k,t) = \hat{u}_0(k) \exp(-k^6 t), \tag{4.29}$$

where $\hat{u}_0(k)$ denotes the Fourier transform of the initial condition $u_0(x)$. To find the fundamental solution we note that for $u_0(x) = \delta(x)$, $\hat{u}_0(k) = \frac{1}{\sqrt{2\pi}}$, where here $\delta(x)$ denotes the Dirac delta function. The fundamental solution is then obtained by taking the inverse Fourier transform of (4.29) and is given by

$$g(x,t) = \frac{1}{2\pi} \int_{-\infty}^{\infty} \exp(-k^6 t + ikx) \mathrm{d}k. \tag{4.30}$$

We are interested in the behaviour of $g(x,t)$ and will investigate its asymptotic behaviour using the method of steepest descents in the limit of large $x/t^{1/6}$. To do this, we let $k = (\frac{x}{6t})^{1/5} z$ in (4.30), which allows us as to express $g(x,t)$ as:

$$g(x,t) = \frac{1}{2\pi} \left(\frac{x}{6t}\right)^{1/5} \mathcal{F}(q), \tag{4.31}$$

$$\mathcal{F}(q) = \int_{-\infty}^{+\infty} \mathrm{e}^{-q\varphi(z)} \mathrm{d}z, \tag{4.32}$$

where $\varphi(z) = \frac{1}{6} z^6 - iz$, and $q = \left(\frac{x}{(6t)^{1/6}}\right)^{6/5}$. We may compute $\mathcal{F}(q)$ by steepest descents for large values of q, *i.e.* for large values of the similarity variable $x/t^{1/6}$.

For large values of q the largest contributions to $\mathcal{F}$ come from the contributions that are in the vicinity of maxima of $\varphi(z)$. The extrema are solutions of $z_m^5 - i = 0$, namely, z_m are the 5th roots of i. The points of steepest descent are $z_m \in \{i, \mathrm{e}^{\frac{i\pi}{10}}, -\mathrm{e}^{-\frac{i\pi}{10}}\}$.

The contribution to the integral from each extremum is given by (Ablowitz, 2003)

$$\mathrm{e}^{-q\varphi(z_m)} \sqrt{\frac{2\pi}{q\varphi''(z_m)}}, \tag{4.33}$$

where, $\varphi(z_m) = -\frac{5}{6} i z_m$ and $\varphi''(z_m) = 5\frac{i}{z_m}$. We may readily see the path of steepest descents by plotting the paths of stationary phase on top of the contour of the real part of $\varphi(z)$ as illustrated in fig. 4.3.

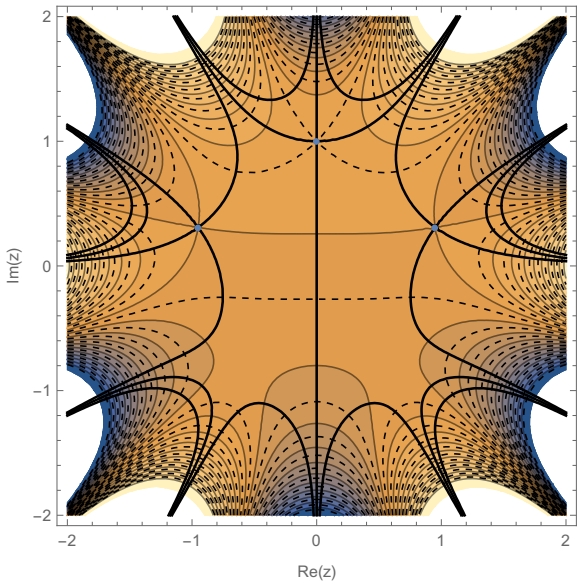

Figure 4.3: Stationary paths plotted on top of the contour of the real part of $\varphi(z)$: The black curves are the paths of stationary phase and the three blue dots are the points providing the largest contribution to the integral.

Indeed, to see the steepest descent path, it is simpler to plot contours of the real part of $\varphi(z)$ (see fig. 4.3). Using Cauchy's Theorem, the integration contour may be deformed to pass through the points of steepest descent. Summing all of these contributions, gives

$$\mathcal{F}(q) \sim \mathrm{e}^{-\frac{5}{6}q}\sqrt{\frac{2\pi}{5q}}\left\{1+2\mathrm{e}^{\frac{5}{6}q(1-\sin\frac{\pi}{10})}\cos\left[\left(\frac{5}{6}q\cos\frac{\pi}{10}\right)-\frac{\pi}{5}\right]\right\}. \tag{4.34}$$

Therefore, as $q=\left(\frac{x}{(6t)^{1/6}}\right)^{6/5}\to\infty$, the Green's function is given by:

$$g(x,t) \sim \frac{1}{2\pi}\left(\frac{x}{6t}\right)^{1/5}\mathrm{e}^{-\frac{5}{6}q}\sqrt{\frac{2\pi}{5q}}\left\{1+2\mathrm{e}^{\frac{5}{6}q(1-\sin\frac{\pi}{10})}\cos\left[\left(\frac{5}{6}q\cos\frac{\pi}{10}\right)-\frac{\pi}{5}\right]\right\}. \tag{4.35}$$

By maximizing the cosine term of (4.34), the evolution in time of the distance between adjacent peaks, x_n, is found to be

$$x_n = 6\left(\frac{\frac{\pi}{5}+2n\pi}{5\sqrt{\frac{5+\sqrt{5}}{8}}}\right)^{5/6} t^{1/6}, \tag{4.36}$$

where we have recall that

$$\begin{cases}\cos\frac{\pi}{10}=\sqrt{\frac{5+\sqrt{5}}{8}},\\ \sin\frac{\pi}{10}=\frac{1}{4}(\sqrt{5}-1).\end{cases}$$

The equation (4.36) implies that the response to a very localized initial condition evolves into an oscillatory function with each peak spreading outwards as $t^{1/6}$. However, since the position x_n of the peaks is not linear in n there is no true wavelength. Instead, we note that the smallest distance between peaks is $\lambda = 12\left(\frac{\frac{\pi}{5}}{\sqrt[5]{\frac{5+\sqrt{5}}{8}}}\right)^{5/6} t^{1/6}$.

The resulting equation (4.34) is interesting because it clearly shows the oscillatory character of the solution in the far field. This solution (4.34) is related to the solution derived by Tulchinsky and Gat (2016) in their study motivated impact on a thin layer. In their problem a localized external pressure is applied to an elastic membrane sitting on a thin viscous film of liquid. The geometry considered is axisymmetric, but if we simplify their problem to one dimension, *i.e.*, a beam, then, the relation given in (4.34) gives the shape of the beam far from the point of application of the external pressure.

Furthermore, Tulchinsky and Gat (2016) analysis gives the Green's function in axisymmetry in terms of a sum of hypergeometric functions. In one dimension, the corresponding Green's function is obtained by direct inversion of (4.30) which gives (using MAPLE or MATHEMATICA)

$$g(x,t) = \frac{1}{2\pi} t^{-1/6}\left[2\Gamma(7/6)\,{}_0F_4\left(;\frac{1}{3},\frac{1}{2},\frac{2}{3},\frac{5}{6};-\frac{x^6}{6^6 t}\right) - \frac{\sqrt{\pi}}{6}\left(\frac{x}{t^{1/6}}\right)^2 {}_0F_4\left(;\frac{2}{3},\frac{5}{6},\frac{7}{6},\frac{4}{3};-\frac{x^6}{6^6 t}\right)\right] \tag{4.37}$$
$$+\, t^{-1/6}\left[\frac{\Gamma(-1/6)}{2\times 6^3}\left(\frac{x}{t^{1/6}}\right)^4 {}_0F_4\left(;\frac{7}{6},\frac{4}{3},\frac{3}{2},\frac{5}{3};-\frac{x^6}{6^6 t}\right)\right].$$

The solution obtained from direct inversion, (4.37), and our derived asymptotic profile (4.35) are illustrated in fig. 4.4 where we may see that the asymptotic solution gives an insight on the oscillatory nature of the fundamental solution.

In the next section we will solve the full constrained problem numerically, taking into account the compressive force, and then extract the time evolution of the wavelength. While in the unconstrained problem there is a similarity solution, demonstrating that there is no true wavelength. In the following we shall talk of a mean wavelength $\bar{\lambda} = 2L/n$ with n the number of peaks in the profile.

4.6 Numerical results

We now move to the constrained problem ($P \neq 0$). To gain insight, we begin by discussing a numerical scheme to solve the problem specified in equations (4.12)–(4.17) using the method of lines (Wouwer *et al.*, 2014). We discretize the spatial

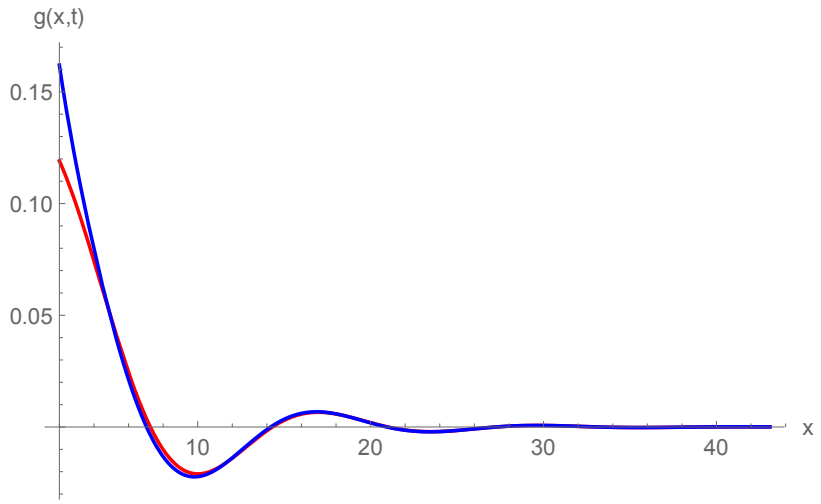

Figure 4.4: Illustration of the Green's function obtained by direct inversion and the asymptotic profile. The blue line is the solution obtained by direct inversion given by (4.37). The red line is the asymptotic solution obtained from (4.35). (Here $t = 100$). This shows that for late times, the solution of (4.24) will exhibit a corrugated/wrinkle profile, which is not, *a priori*, obvious.

variable, x, in grid points x_i, $1 \leq i \leq N+1$, in a way that conserves the flux on the interval $[(x_1 + x_2)/2, (x_N, x_{N+1})/2]$. The end points are x_1 and x_{N+1} and there are $N-1$ unknowns, $u_i = u(x_i)$, for $i = 2, \ldots, N$. This leads to a series of ordinary differential equations for the evolution of $u_i(t) = u(x_i, t)$:

$$\frac{\mathrm{d}u_i}{\mathrm{d}t} = a_i p_{i+1} - (a_i + b_i)p_i + b_i p_{i-1}, \tag{4.38}$$

$$p_i = \kappa_{i+1} - 2\kappa_i + \kappa_{i-1} + P\kappa_i, \tag{4.39}$$

$$\kappa_i = u_{i+1} - 2u_i + u_{i-1}, \tag{4.40}$$

$$a_i = \frac{1}{\Delta x^6}[1 + (u_{i+1} + u_i)/2]^3, \tag{4.41}$$

$$b_i = \frac{1}{\Delta x^6}[1 + (u_i + u_{i-1})/2]^3, \tag{4.42}$$

subject to the imposed constraint (4.13), which becomes

$$\Delta = \frac{1}{2\Delta x}\sum_{i=1}^{N}(u_{i+1} - u_i)^2. \tag{4.43}$$

Here, κ_i denotes the approximation to the curvature and p_i the hydrodynamic pressure at x_i. In order to obtain (4.43), the integrand of the constraint, (4.13), is computed using finite differences, centred at the half points $(x_i + x_{i+1})/2$.

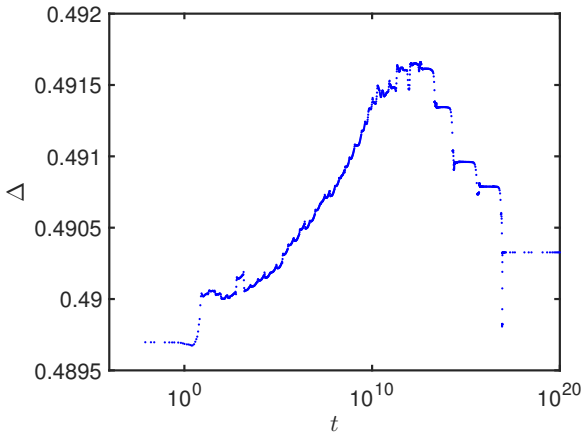

Figure 4.5: Evolution of the end-shortening Δ for the numerical data presented in fig.4.8 (a localized, Gaussian initial condition). The initial value of the end shortening is $\Delta(t=0) = 0.4897$ and the maximum drift is 2×10^{-3}.

The system (4.38)–(4.43) is a differential algebraic equation (DAE) of index 2. We decrease its index to 1 by differentiating the constraint. The resulting system is a differential algebraic equation that may be integrated in time using the MATLAB routine ode15s (ode15s is able to handle a DAE of index 1 automatically). The solution of this DAE conserves the value of Δ of the initial condition to within 1% in the simulations reported here.

In the simulations reported here we use a dimensionless system $L = 1000$ and $N = 1024$ uniformly distributed grid points. The numerical scheme implemented in this way runs quickly on a laptop computer (simulations reported here typically complete in a few minutes).

Throughout the simulations, we use two types of initial conditions. The first type is a fully random noise that is uniformly distributed. This initial condition is then of the form

$$u(x_i, 0) = u_0(x_i) = \mathcal{R}_i, \tag{4.44}$$

where the $\mathcal{R}_i$ are randomly drawn from the uniform distribution $[-\varepsilon, \varepsilon]$. The second type of initial condition is localized, and of the form $u(x_i, 0) = \varepsilon e^{-x_i^2}$. In both cases, we typically take $\varepsilon = 10^{-2}$ here. The value of the end-shortening constraint at later times is imposed to be that of the initial condition after using (4.43) to calculate Δ.

Indeed we did not reinforce the original constraint directly but instead checked afterwards that the drift in the value of Δ was less than 1% of its original value. In fig. 4.5 we show the evolution of the end shortening Δ for a localized initial condition with $\Delta(t=0) = 0.4897$; note that the change in Δ is at most 2×10^{-3}.

The key quantity of interest in this study is the evolution of the average wrinkle wavelength, $\bar{\lambda}(t)$. Here we measure $\bar{\lambda}$ in a way that mimics experimental procedures (Huang and Im, 2006): the number of peaks in the instantaneous beam profile, $n(t)$, is counted so that, by definition, $\bar{\lambda}(t) = 2L/n(t)$. We prefer this technique to others (such as discrete Fourier Transforms) since have seen in the similarity solution that there is not a true wavelength (in the sense of a length scale over which the pattern repeats).

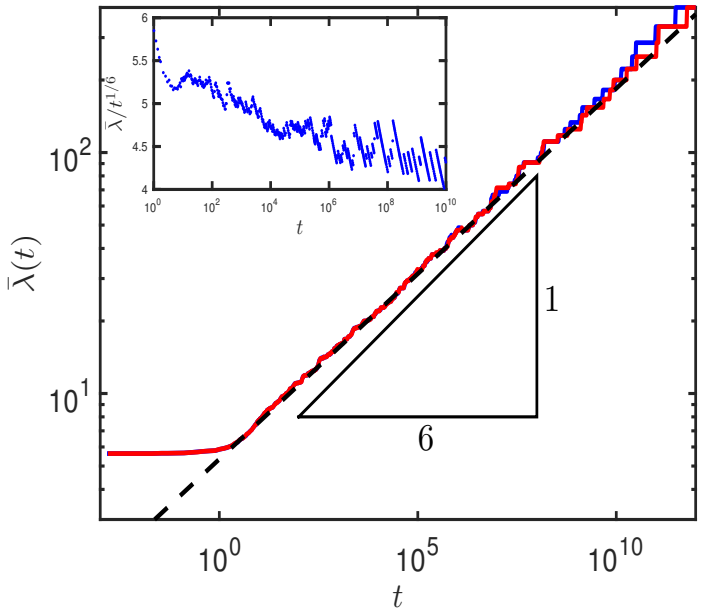

Figure 4.6: Evolution of the mean wrinkle wavelength, $\bar{\lambda}(t)$, as a function of time, determined from the numerical solution of (4.12)-(4.17), and (4.18)-(4.23). Main figure: The mean wavelength as determined in both the fully nonlinear system, (4.12)-(4.17), (see, blue curve), and the linearized system, (4.18)-(4.23)(see, red curve). For times $1 \lesssim t \lesssim 10^{10}$ the behaviour appears to follow a power-law relationship, but with $\bar{\lambda} \propto t^{0.153}$ (black dashed line), which is subtly different from the power law $\lambda \sim t^{1/6}$ suggested previously (Vandeparre *et al.*, 2010). Inset: A compensated plot of the evolution of $\bar{\lambda}/t^{1/6}$ shows a systematic drift from the scaling $\lambda \sim t^{1/6}$. Here, the wavelength is determined by counting the number of peaks in the profile at any instant, $n(t)$, so that $\bar{\lambda}(t) = 2L/n(t)$. In these simulations, $L = 1000$, $\Delta = 17.7 \times 10^{-3}$ and $N = 1024$ grid points. The initial condition is $h(x, 0) = 1 + u_0(x)$ with $-\varepsilon \leq u_0(x) \leq \varepsilon$ a uniformly distributed random number at each point and $\varepsilon = 10^{-2}$; the same random condition is used for both sets of simulations. Reprinted figure with permission from O. Kodio *et al.* (2017). 'Lubricated wrinkles: Imposed constraints affect the dynamics of wrinkle coarsening'. *Physical Review Fluids* 2.1, p. 014202. DOI: 10.1103/PhysRevFluids.2.014202. Copyright 2017 by the Americal Physical Society.

The evolution of the mean wavelength is shown in fig. 4.6. Despite the expectations

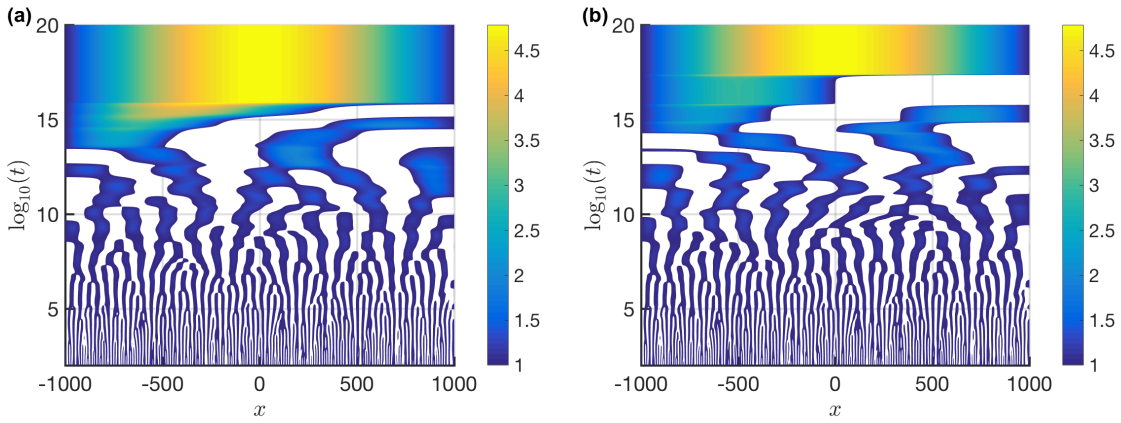

Figure 4.7: Comparison of the evolution of the beam deflection (and hence film thickness) observed in (a) fully nonlinear case, (4.12)-(4.17), and (b) hydrodynamically linear case, (4.18)-(4.23). Colours represent the value of the film thickness, $h = 1 + u(x,t)$, at each point of (x,t)-space, according to the colour bar on the right of each plot. (Note that to emphasize wrinkles, regions with $h < 1$ are whited-out.) In each case, we observe qualitatively similar coarsening, motivating a more detailed analytical study of the linear problem. In these simulations, $L = 1000$, with $N = 1024$ grid points and $\Delta = 17.7 \times 10^{-3}$. The initial condition $u(x,0)$ is drawn randomly from a uniform distribution on $[-\varepsilon, \varepsilon]$ with $\varepsilon = 10^{-2}$; the same random initial condition is used in both (a) and (b). Reprinted figure with permission from O. Kodio *et al.* (2017). 'Lubricated wrinkles: Imposed constraints affect the dynamics of wrinkle coarsening'. *Physical Review Fluids* 2.1, p. 014202. DOI: `10.1103/PhysRevFluids.2.014202`. Copyright 2017 by the Americal Physical Society.

based on the unconfined evolution that $\bar{\lambda} \propto t^{1/6}$, over the long duration shown in our numerical experiments we observe a significant (and systematic) deviation from this scaling law (see the inset of fig. 4.6). For the data range shown in this figure a more appropriate power law appears to be $\bar{\lambda} \propto t^{0.153}$. However, the precise value of this alternative exponent depends on the interval of time that is considered, suggesting that the true behaviour may not quite be a power law at all.

The $\bar{\lambda} \sim t^{1/6}$ scaling predicted in (4.25) was based on a simple, linearized balance between the terms in the governing nonlinear PDE. We therefore ask whether this discrepancy is a result of one of the two nonlinearities in the system. To address this question, we consider numerically the hydrodynamically linear (geometrically nonlinear) PDE that is obtained by setting $h \approx 1$ in (4.12). The evolution of $\bar{\lambda}(t)$ in this linear case is identical to the hydrodynamically nonlinear problem, at least for early and intermediate times.

The close correspondence between the linearized, (4.18)-(4.23), and nonlinear problems, (4.12)-(4.17), can also be seen in the evolution of the film thickness $h(x,t)$,

for each case, shown in fig. 4.7. In particular, both the nonlinear and linearized problems show a smoothening of the initial condition with time, and a coarsening of the wrinkles. The similarity between the nonlinear and linearized problems suggests that the anomalous behaviour in the wrinkle wavelength is due to the geometric nonlinearity (the integral constraint), and not the hydrodynamic nonlinearity due to Reynolds' equation, (4.12). To gain some insight into the role that this geometrical nonlinearity plays, we therefore focus on the linearized case, (4.18)-(4.23), *i.e.* when the term h^3 in (4.12) is approximated by unity. We expect that this approximation will be valid when $u = h - 1 \ll 1$, though we note that this condition may not necessarily remain valid throughout the evolution of the system (since, as the wrinkles coarsen, u increases). Incidentally, as the displacement increases in time, one may wonder whether the phenomenon of *pinch off* may occur (see for examples Bertozzi, 1996; Carlson and Mahadevan, 2015; Peschka *et al.*, 2010). However in the simulations we performed, we have not observed a pinch off.

4.7 Effect of confinement

Our numerical solution of the linearized problem (shown in fig. 4.7) shows that this problem also demonstrates the wrinkle coarsening behaviour that is of interest here. More quantitatively, we have already seen that the numerically determined mean wrinkle wavelength varies with time in a very similar way (at least for small and intermediate times) in both the linearized and nonlinear problems. In particular, the linear problem also shows that the wrinkle wavelength does not obey the expected $\bar{\lambda} \propto t^{1/6}$ behaviour. In this section we analyze the linearized problem to gain some understanding of the origin of this discrepancy.

4.7.1 Fourier Transform

To simplify the problem, we consider the spatial domain to be infinite, i.e. $L = \infty$, which we expect to be relevant before the wrinkles feel the effect of the edges (We consider the effect of finite length L in §4.10). We then have the following linear system (albeit with a nonlinear integral constraint) for $u(x,t)$ and the compressive force $P(t)$:

$$\frac{\partial u}{\partial t} = \frac{\partial^6 u}{\partial x^6} + P(t)\frac{\partial^4 u}{\partial x^4}, \tag{4.45}$$

with initial condition

$$u(x, t = 0) = u_0(x), \tag{4.46}$$

boundary conditions at $x = \pm\infty$

$$u = \frac{\partial^2 u}{\partial x^2} = \frac{\partial^4 u}{\partial x^4} = 0 \tag{4.47}$$

and the constraint

$$\frac{1}{2}\int_{-\infty}^{\infty} \left(\frac{\partial u}{\partial x}\right)^2 \, \mathrm{d}x = \Delta. \tag{4.48}$$

Given that the boundary conditions are now imposed at infinity, and that the governing partial differential equation is linear, it is natural to take the Fourier transform of equation (4.45).

Taking the Fourier Transform of (4.45) yields

$$\frac{\partial \hat{u}}{\partial t} = k^4[P(t) - k^2]\hat{u}, \tag{4.49}$$

which may be integrated to give

$$\hat{u}(k,t) = \hat{u}_0(k)\exp[-k^6 t + \Pi(t)k^4], \tag{4.50}$$

where $\hat{u}_0(k)$ is the Fourier Transform of the initial condition and

$$\Pi(t) = \int_0^t P(s)\,\mathrm{d}s. \tag{4.51}$$

Inverting the Fourier transform of the profile by substituting (4.50) into (4.27), we find that the solution of the problem may be expressed as

$$u(x,t) = \frac{1}{\sqrt{2\pi}}\int_{-\infty}^{\infty} \hat{u}_0(k)\exp[-k^6 t + \Pi(t)k^4]\mathrm{e}^{\mathrm{i}kx} \, \mathrm{d}k. \tag{4.52}$$

We note that if the compressive force P were constant then we would expect from eqn (4.50) that the solution would consist of waves with wavenumber $k = k_c = (2/3)^{1/2}P^{1/2}$, which corresponds to the fastest growing linear mode (Biot, 1957). However, in this problem $P(t)$ evolves with time and, further, $P(t)$, and hence $\Pi(t)$, are not known *a priori*. Physically, $P(t)$ is determined by the constraint (4.48), which may be rewritten in terms of $\hat{u}(k,t)$ using the Parseval–Plancherel Theorem (Carleman, 1944),

$$\frac{1}{2}\int_{-\infty}^{\infty} k^2|\hat{u}|^2 \, \mathrm{d}k = \Delta, \tag{4.53}$$

and must hold for all time. Substituting the general solution (4.50) into the constraint (4.53), we have

$$\frac{1}{2}\int_{-\infty}^{\infty} k^2|\hat{u}_0(k)|^2 \exp\left[-2(k^6 t - \Pi(t)k^4)\right] \, \mathrm{d}k = \Delta. \tag{4.54}$$

4.7.2 Asymptotic evaluation of the compressive force P

In the following we seek to determine the late-time[1] behaviour of the compressive force $P(t)$ and the profile $u(x,t)$. Defining

$$\sigma(t) = \Pi(t)^3/t^2,$$

and letting $k = t^{-1/6}\sigma(t)^{1/6}z$ then (4.54) becomes

$$\sigma^{1/2} I(\sigma;t) = 2t^{1/2}\Delta, \tag{4.55}$$

where

$$I(\sigma;t) = \int_{-\infty}^{\infty} z^2 \left|\hat{u}_0\left(z\sigma^{1/6}t^{-1/6}\right)\right|^2 \mathrm{e}^{-2\sigma(z^6-z^4)}\,\mathrm{d}z. \tag{4.56}$$

The natural scaling suggested in §4.5 predicts that $P \propto t^{-1/3}$, $\Pi \propto t^{2/3}$ as $t \to \infty$. However, this implies that σ and I both tend to constants as $t \to \infty$. This would cause the LHS of (4.55) to be constant, which is inconsistent with the diverging RHS. We therefore conclude that $\sigma \to \infty$ as $t \to \infty$, and hence that $P(t)$ must decay more slowly than $t^{-1/3}$. The quantity σ therefore gives a measure of how far the compressive force P is from the $P \sim t^{-1/3}$ behaviour required for self-similarity. To quantify the actual behaviour, however, we need to understand the asymptotic behaviour of the integral $I(\sigma;t)$ when $t \gg 1$. This integral can be evaluated using Laplace's method, (see Ablowitz, 2003); our analysis follows the analysis of a related problem by Budd and Peletier (2000).

In applying Laplace's method, we find that the dominant contribution to the integral arises when the exponent is stationary, *i.e.* when $z = z_\pm = \pm\sqrt{2/3}$. We must therefore evaluate $\hat{u}_0\left(z\sigma^{1/6}t^{-1/6}\right)$ at $z = z_\pm$. If the quantity σ/t were to grow without bound then $\hat{u}_0\left(\sigma^{1/6}t^{-1/6}z_\pm\right) \to \hat{u}_0(\infty)$, which, according to the Riemann-Lebesgue Lemma is zero assuming $u_0(x)$ is integrable. It is also not possible that σ/t tends to a constant other than zero, by considering the constraint (4.55) directly. We therefore see that dominant contribution to the integral arises from $k \approx 0$ and approximate $\hat{u}_0(k) \approx \hat{u}_0(0)$. (Here, we assume that $\hat{u}_0(0) \neq 0$; at the end this section we extend the following analysis to the case $\hat{u}_0(0) = 0$.)

We find that

$$I(\sigma;t) \sim \sqrt{\frac{\pi}{3}}|\hat{u}_0(0)|^2\sigma^{-1/2}\mathrm{e}^{\frac{8\sigma}{27}} \text{ as } \sigma, t \to \infty. \tag{4.57}$$

and hence, upon substituting (4.57) into (4.56), that

$$\Delta \sim \tfrac{1}{2}\sqrt{\frac{\pi}{3}}|\hat{u}_0(0)|^2 t^{-1/2} \exp\left(\frac{2^3}{3^3}\sigma\right). \tag{4.58}$$

[1] before the solutions feel the boundary conditions and become discrete.

Inverting (4.58) we find that

$$\sigma \sim \frac{3^3}{2^3}\left[\tfrac{1}{2}\log(t/t_c)\right], \tag{4.59}$$

where

$$t_c = \frac{\pi}{12}\frac{|\hat{u}_0(0)|^4}{\Delta^2}. \tag{4.60}$$

The initial condition enters the asymptotic prediction (4.59) only through $\hat{u}_0(0)$ in the time scale t_c. Since $\hat{u}_0(0) = \frac{1}{\sqrt{2\pi}}\int_{-\infty}^{\infty} u_0(x)\,\mathrm{d}x$ this quantity represents the excess (or deficit) of fluid that is introduced in the initial condition.

The relative error in the leading-order expression (4.57) may be calculated using standard arguments (Bender and Orsag, 1999). We find that this correction, R, is given by

$$R = \frac{9}{64\sigma}\left[1 + \frac{2}{3}(\sigma/t)^{1/3}\frac{\hat{u}_0''(0)}{\hat{u}_0(0)}\right], \tag{4.61}$$

and so conclude that for our asymptotic analysis to be valid ($R \ll 1$), we must have

$$\sigma \gg 9/64, \tag{4.62}$$

and

$$t^{1/3}\sigma^{2/3} \gg \frac{3}{32}\frac{\hat{u}_0''(0)}{\hat{u}_0(0)}. \tag{4.63}$$

As a consequence, our late-time analysis is valid for a symmetric localized initial condition of typical width L_0, when $\log(t/t_c) \gg 1/12$ and $t^{1/6}(\log t)^{1/3} \gg L_0/3^{1/2}2^{7/6}$. The first condition, (4.62), shows that t_c gives the time scale over which the system 'forgets' the initial condition, $u_0(x)$; we shall comment on the physical significance of the second condition, (4.63), later.

From the expression (4.59), we may deduce that

$$\Pi(t) \sim \frac{3}{2}t^{2/3}\left[\tfrac{1}{2}\log\left(t/t_c\right)\right]^{1/3}. \tag{4.64}$$

Note that this asymptotic behaviour of $\Pi(t)$ is close to the $t^{2/3}$ scaling that would have been anticipated from the analyis in §4.5 but includes a logarithmic correction.

With $\Pi(t)$ determined asymptotically, we can now determine the asymptotic behaviour of the compressive force, $P(t)$, by differentiating (4.64); we find that

$$P(t) \sim \left[\frac{\log\left(t/t_c\right)}{2t}\right]^{1/3}. \tag{4.65}$$

Furthermore, for $t \gg t_c$, the leading-order result is

$$P(t) \sim 2^{-1/3}\left(\frac{\log t}{t}\right)^{1/3}. \tag{4.66}$$

4.7.3 Late time evolution of the profile $u(x,t)$ and its wavelength $\lambda(t)$

The effect of the constraint on the dynamics of wrinkling is embodied in the relationship (4.65) for the compressive force that must be applied to impose the given end-shortening (after all, without this force, there is no imposed end-shortening). However, what interests us most is the mean wavelength of the buckling pattern; to understand this, we now turn to the profile of the beam itself.

The inverse Fourier transform of the profile, (4.52), may be written as

$$u(x,t) = \frac{1}{\sqrt{2\pi}} \frac{\sigma^{1/6}}{t^{1/6}} U_\sigma(\xi, t), \tag{4.67}$$

where

$$U_\sigma(\xi,t) = \int_{-\infty}^{\infty} \hat{u}_0 \left(\frac{\sigma^{1/6}}{t^{1/6}} z \right) \exp\left[-\sigma(z^6 - z^4) \right] \mathrm{e}^{\mathrm{i}\xi z} \, \mathrm{d}z, \tag{4.68}$$

and $\xi = x(\sigma/t)^{1/6}$. From equation (4.64) we may infer the late-time behaviour of the new variable ξ, which is given by $\xi \sim \sqrt{\frac{3}{2}}\, x/(2t/\log(t/t_c))^{1/6} \sim x\sqrt{3P/2}$ as $t \to \infty$.

To evaluate $U_\sigma(\xi,t)$ for large σ, we again use Laplace's method; as in the evaluation of the integral in (4.56) we find that the integral is dominated by the behaviour around $z = z_\pm = \pm\sqrt{2/3}$. Making the usual approximation of the integrand for $z \approx z_\pm$, we find that

$$U_\sigma(\xi,t) \sim \sqrt{\frac{3\pi}{2}} \hat{u}_0(0) \frac{\exp\left(\frac{4}{27}\sigma - \frac{3}{32}\frac{\xi^2}{\sigma} \right)}{\sigma^{1/2}} \cos(\sqrt{\tfrac{2}{3}}\xi), \tag{4.69}$$

for $\sigma \gg 1$ and hence that the long-time behaviour of the profile may be written

$$u(x,t) \sim A_0 \exp\left(-\frac{3}{32}\frac{\xi^2}{\sigma} \right) \cos\left(\sqrt{\tfrac{2}{3}}\xi \right), \tag{4.70}$$

where $A_0 \sim \pm 2^{5/6} 3^{-1/4} \pi^{-1/4} \Delta^{1/2} (\log t)^{-1/3} t^{1/12}$. In (4.70), the positive sign for A_0 corresponds to the case of a profile that has an initial excess of fluid, while the negative sign corresponds to the case of a profile with an initial deficit of fluid. Having determined the asymptotic relationship (4.70), we note two interesting features of this result. Firstly, for late times the $u(x,t) \propto t^{1/12}$ (ignoring logarithmic terms), following what would be expected from the scaling analysis discussed in §4.5. Secondly, the initial condition $u_0(x)$ does not appear explicitly in the result (4.70): the only feature of the initial condition that is 'remembered' at very late times is the imposed end-shortening, Δ. We can now also interpret the second condition for the validity of the asymptotic expression, (4.63), as the time over which the width of the exponential

envelope in (4.70) becomes larger than the typical width of the initial condition, as might intuitively be expected.

The late-time profile (4.70) also shows that the asymptotically correct shape of the deformed beam does *not* adopt a self-similar shape: having introduced a similarity-like variable, ξ, in (4.70), we see that there remains some (albeit weak) time dependence in the exponential term that cannot be removed by rescaling.

Finally, we note that the profile in (4.70) takes the form of a spatial oscillation that is modulated by an exponential decay. As such, the wrinkle pattern is not perfectly periodic and does not have a true wavelength. Nevertheless, wrinkles are observed and a natural measure of this wrinkle pattern is the distance between consecutive zeros of the cosine, Δx, which is given for late times by

$$\Delta x \sim 2^{1/6}\pi \left[\frac{t}{\log(t/t_c)}\right]^{1/6}. \tag{4.71}$$

We estimate the apparent wavelength $\bar{\lambda}$ as twice the distance between zeros, hence

$$\bar{\lambda} \sim 2^{7/6}\pi \left[\frac{t}{\log(t/t_c)}\right]^{1/6}, \tag{4.72}$$

which for late times, $t \gg t_c$, reads

$$\bar{\lambda} \sim 2^{7/6}\pi \left(\frac{t}{\log t}\right)^{1/6}. \tag{4.73}$$

4.7.4 Extension to the case of $\hat{u}_0(0) = 0$

The asymptotic analysis presented in so far relied on the assumption that $\hat{u}_0(0) \neq 0$, i.e. that the initial condition contains an excess (or deficit) of fluid since $\int_{-\infty}^{\infty} u_0(x)\,\mathrm{d}x = \sqrt{2\pi}\hat{u}_0(0) \neq 0$.

Now, we consider the case in which the initial condition has no deficit or excess of liquid so that $\hat{u}_0(0) = 0$. This may happen for example with a perfectly anti-symmetric initial condition. The analysis follows through in much the same steps from equation (4.57) to equation (4.73) but this time with $\hat{u}_0(k) \approx k\hat{u}_0'(0)$ for $k \ll 1$ where

$$\hat{u}_0'(0) = -\frac{\mathrm{i}}{\sqrt{2\pi}} \int_{-\infty}^{\infty} u_0(x)x\,\mathrm{d}x \tag{4.74}$$

(so that it is the dipole moment of the initial condition that dominates). We find that $\sigma \sim \frac{3^3}{2^3}\log[(t/t_c)^{5/6}]$ at late times, where now $t_c = \left(\sqrt{3\pi}|\hat{u}_0'(0)|^2/9\Delta\right)^{6/5}$ and so the late-time behaviour of the compressive force is

$$P(t) \sim \left(\tfrac{5}{6}\right)^{1/3} \left(\frac{\log t}{t}\right)^{1/3}. \tag{4.75}$$

Note that the prefactor in this new late-time behaviour of the compressive force (4.75) is $(5/6)^{1/3} \approx 0.941$, compared to $(1/2)^{1/3} \approx 0.794$ for an initial condition with an excess or deficit, $\hat{u}_0(0) \neq 0$.

At late times, the beam profile is given by

$$u(x,t) \sim A_1 \exp\left(-\frac{3}{32}\frac{\xi^2}{\sigma}\right) \sin\left(\sqrt{\tfrac{2}{3}}\xi\right), \tag{4.76}$$

where $A_1 = \pm 2^{1/2} 3^{-1/4} \pi^{-1/4} \Delta^{1/2} t^{1/12} (\log t^{5/6})^{-1/3}$, where again $\xi = x(\sigma/t)^{1/6}$. Note that in this case, the mean wavelength is unchanged fro the expressions given in (4.73)

4.8 Comparison with numerical results

Having determined asymptotic predictions for the evolution of the compressive force and the mean wavelength for late times, we now turn to compare these results with numerical simulations of the fully nonlinear problem, (4.12)–(4.17).

4.8.1 A localized symmetric initial condition

The asymptotic analysis relies on the initial condition being localized (for the error in the application of Laplace's method to be small). In fig. 4.8 we therefore show numerical results for a localized initial condition, $u_0(x) = \varepsilon e^{-x^2}$ with $\varepsilon = 10^{-2}$. One might expect such an initial condition to yield a single bump spreading outwards; instead, the space–time plot of fig. 4.8a shows that wrinkles form on either side of the bump, resulting in a spreading corrugated pattern a wavelength that increases with time. When the wrinkles reach the boundary this continuous gradual coarsening is replaced by quick jumps between the quasi-static Euler-buckling modes as the number of wrinkles decreases towards the final Euler-buckled state. We see in fig. 4.8b that the compressive force $P(t)$ follows the asymptotic prediction (4.65) well, until the system starts to feel its size: the compressive force P then gets temporarily 'stuck' at a value that corresponds to one of the appropriate Euler-buckling modes. The system then transitions quickly to the next Euler buckling mode, as signified by a sudden decrease in P. The values of P selected by our simulations at these very late times appears to depend on the symmetry of the initial condition: the symmetric initial condition used leads to values of P close to those of the symmetric Euler buckling modes (i.e. $LP^{1/2} = (n + 1/2)\pi$, with n an integer) until a single bump remains. We consider the study of these discrete modes in 4.10.

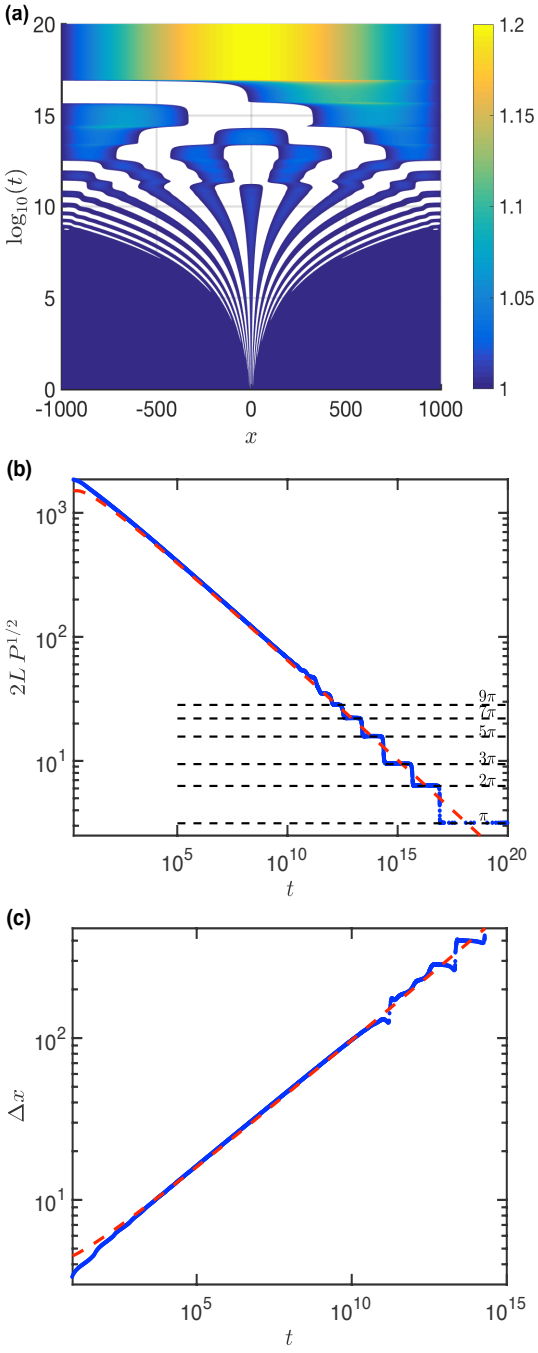

Figure 4.8: Numerical solution of the fully nonlinear system (4.12)–(4.17) subject to a localized initial condition $u_0(x) = \varepsilon e^{-x^2}$. (a) The profile quickly develops wrinkles that eventually fill the entire domain before individually being squeezed out to give the final Euler-buckled mode. Colours represent the value of the film thickness, h, at each point of (x, t)-space, according to the colour bar on the right of the plot. Note that to highlight wrinkles, regions with $h(x, t) < 1$ are whited-out. (b) The compressive force evolves according to the prediction of the linearized analysis (4.65) but ultimately breaks down when the presence of the boundaries becomes important. For very late times the compressive force steps through periods where it is approximately constant, taking values close to the eigenvalues of the corresponding Euler-buckling problem, $2LP^{1/2} = (2n + 1)\pi$ for $n = 0, 1, 2, \ldots$ (indicated by horizontal dashed lines). (c) The numerically determined distance between the first and the second zeros (points) is consistent with the asymptotic prediction (4.71) (dashed line). For very late times ($t \gtrsim 10^{15}$) only a few, larger bumps remain; at this stage the effect of the edges become important and the asymptotic result breaks down. In all simulations reported here, $L = 1000$, $N = 1024$, $\Delta = 4.9 \times 10^{-5}$ and $\varepsilon = 10^{-2}$. Reprinted figure with permission from O. Kodio *et al.* (2017). 'Lubricated wrinkles: Imposed constraints affect the dynamics of wrinkle coarsening'. *Physical Review Fluids* 2.1, p. 014202. DOI: 10.1103/PhysRevFluids.2.014202. ©2017 American Physical Society.

4.8.2 A localized anti-symmetric initial condition

With an anti-symmetric initial condition the prefactor in the late-time behaviour of the compressive force eqn (4.75) is $(5/6)^{1/3} \approx 0.941$, compared to $(1/2)^{1/3} \approx 0.794$ for an initial condition with an excess or deficit, $\hat{u}_0(0) \neq 0$. To appreciate this difference

between the two cases, the inset of fig. 4.9 shows this difference via a compensated plot of the evolution of $P(t)$ in the two cases.

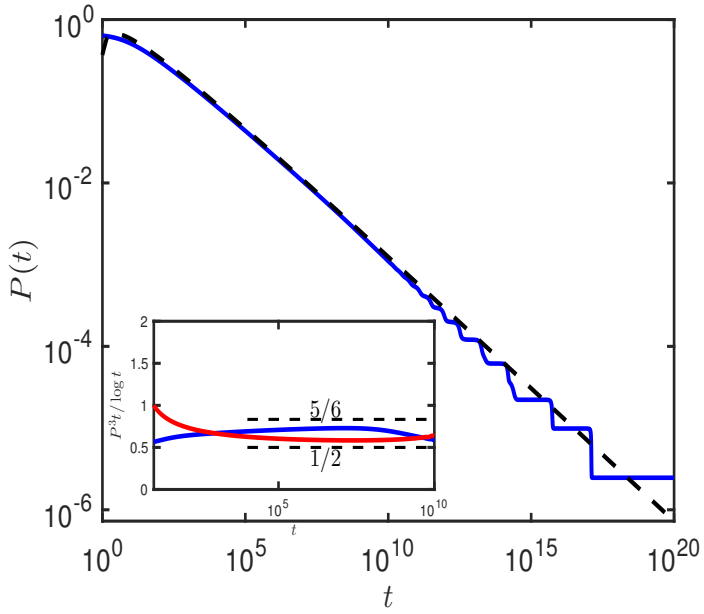

Figure 4.9: Validation of the asymptotic predictions for the case of no excess or deficit fluid, $\hat{u}_0(0) = 0$. Numerical results are obtained by solving equations (4.12)–(4.17). The blue curve represents the numerically determined compressive force, $P(t)$, and the dashed black line is the asymptotic prediction (4.75). The inset illustrates the compensated plot $P^3t/\log t$ which approaches the expected value of 5/6 for the anti-symmetric case (blue curve) and 1/2 for the symmetric case (red curve, data from fig. 4.8). The deviation at late times is due to the finite size of the domain. Here the anti-symmetric initial condition is $u(x,0) = \varepsilon x \exp(-x^2/4)$. The simulation is performed with $L = 1000$, $N = 1024$, $\varepsilon = 10^{-2}$, $\Delta = 5 \times 10^{-5}$. Reprinted with permission from O. Kodio *et al.* (2017). 'Lubricated wrinkles: Imposed constraints affect the dynamics of wrinkle coarsening'. *Physical Review Fluids* 2.1, p. 014202. DOI: `10.1103/PhysRevFluids.2.014202`. ©2017 Americal Physical Society.

4.8.3 A random initial condition

It is also informative to examine data for the average wavelength in the fully nonlinear system with a random initial condition. A direct comparison of this numerical data and the corresponding asymptotic prediction (4.73) is shown in fig. 4.10. Again, this shows good agreement between the fully nonlinear problem and the linear analysis, at least until the wrinkles fill the domain. This is somewhat surprising since the initial condition used here is random and hence may not have a Fourier Transform that is dominated by the value of $\hat{u}_0(0)$, as is required for the late-time analysis to

hold. This good agreement suggests that the existence of local inhomogeneities in the initial condition may be important in determining the evolution of the coarsening of wrinkles, as has been observed in elastocapillary aggregation (Singh *et al.*, 2013). As expected, the higher-order correction offered by including t_c improves the agreement between the asymptotic and numerical results (fig. 4.10).

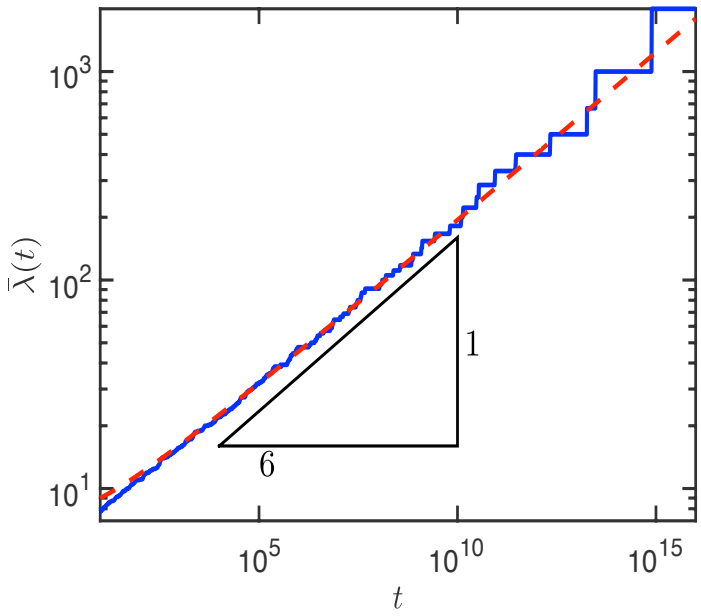

Figure 4.10: Wrinkle coarsening from a random initial condition appears to be governed by the evolution of localized bumps. Here the fully nonlinear problem is solved numerically with a randomized initial condition. The mean wrinkle wavelength ($\bar{\lambda} = 2L/n(t)$) evolves according to the long-time asymptotic prediction of the linearized problem with a localized initial condition, (4.73), which is shown as the dash–dotted curve. The numerical results presented here are obtained with $L = 1000$, $N = 1024$, $\Delta = 17.7 \times 10^{-3}$ and a random initial condition drawn from the uniform distribution on $[-\varepsilon, \varepsilon]$ with $\varepsilon = 10^{-2}$. Note that at very late times the system is temporarily attracted to Euler-buckled modes but illustrates sudden jumps between them; this accounts for the sudden large jumps in $\bar{\lambda}$ that are observed at late times. This apparition of jumps is qualitatively similarly to those occurring with a localized initial condition, see 4.8(c); and these jumps will be studied in details in §4.10. Reprinted figure with permission from O. Kodio *et al.* (2017). 'Lubricated wrinkles: Imposed constraints affect the dynamics of wrinkle coarsening'. *Physical Review Fluids* 2.1, p. 014202. DOI: 10.1103/PhysRevFluids.2.014202. ©2017 Americal Physical Society.

4.9 Comparison with previous experiments

Having thoroughly investigated the evolution of the mean wrinkle wavelength using numerical simulations and a linearized analysis, we now return to reconsider the earlier experiments of Vandeparre *et al.* (2010) that initially motivated this chapter. In their experiments, Vandeparre *et al.* (2010) studied the evolution of a thin titanium sheet (thickness $h_{\mathrm{Ti}} = 15$ nm, and Young's modulus $E_{\mathrm{Ti}} = 10^{11}$ Pa) above a thin substrate of polystyrene (thickness $h_0 = 250$ nm). The titanium–polystyrene composite is prepared as a solid and then heated above the glass transition temperature of the polystyrene. At early times, the system wrinkles with a wavelength determined purely by the elastic properties of the system (Stafford *et al.*, 2004). At later times the polystyrene relaxes viscously and the wavelength starts to grow as a function of time (all while the temperature remains fixed). Using different temperatures above the glass transition temperature allows the effective viscosity of the polystyrene to be varied, and hence the time scale of the evolution to be varied too. However, the results as presented by Vandeparre *et al.* (2010) are shifted to obtain a master curve at a temperature close to 120°C using the WLF time–temperature superposition.

Motivated by our asymptotic analysis, we re-examine the experimental data presented by Vandeparre *et al.* (2010). In the inset of fig. 4.11 we show a compensated plot of t/λ^6 versus t (on a semi-logarithmic scale). This shows, firstly, that there is a systematic difference between experiments and the $\lambda \sim t^{1/6}$ behaviour expected from the naive scaling analysis (though we note that calculating λ^6 is likely to accentuate errors). Secondly, plotted in this way, the experimental data suggest the presence of a $\log t$ behaviour, as predicted by our theory (4.73). The noise inherent in the data make it difficult to infer an effective value of t_c, and there are not sufficient experimental details to compute t_c. Nevertheless, the time scale t_c is the time at which t/λ^6 vanishes on a semi-logarithmic plot (see inset of fig 4.11). Here, we estimate this value to be $t_c = 0.0837$ s from a best fit of all experimental data. We therefore non-dimensionalize times with a time scale $t_0 = t_c$ and note that this corresponds to a length scale $\lambda_0 = [Bh_0^3 t_0/(12\mu)]^{1/6}$. The length scale λ_0 can only be estimated once the viscosity μ is known. However, for the range of temperatures studied experimentally, estimates of μ vary in the range $10^5 - 10^6$ Pa s (Plazek and Rourke, 1971). We therefore use the viscosity μ as a (the only) fitting parameter, finding that $\mu = 2 \times 10^5$ Pa s (consistent with previous published data Plazek and Rourke (1971)); using standard values for titanium this gives that $\lambda_0 \approx 0.16$ μm.

In figure 4.11 we compare the evolution of the wrinkle wavelength measured experimentally by Vandeparre *et al.* (2010) with the long-time asymptotic behaviour predicted here, (4.73). We see that the asymptotic prediction (4.73) gives extremely good agreement with experiments, particularly for $t/t_0 \gg 1$. We emphasize that in plotting fig. 4.11 we have fitted only one parameter (the liquid viscosity μ), with the same value used to plot all data sets. Of particular interest is that for the time scales of experimental interest, the difference between the scaling prediction $t^{1/6}$ of Vandeparre *et al.* (2010) and our result $(t/\log t)^{1/6}$ is relatively large: the line of best fit suggested previously (Vandeparre *et al.*, 2010) corresponds to an exponent ≈ 0.133. As a result we conclude that the refined theory presented here is likely to be of considerable use for understanding the moderate time scales that are accessible experimentally, for which the variation due to the $\log t$ is large enough to be observable.

4.10 Temporal cascade: relaxation of the Euler buckling modes

While the analysis thus far allows us to understand the relatively late stages of the experiments of Vandeparre *et al.* (2010), our numerical solutions reveal a new regime as the wavelength of wrinkles, λ, becomes comparable to the size of the system L: as we saw in fig. 4.8(b) and in fig. 4.9, for extremely late times, boundary effects start to dominate, and there is the appearance of discrete modes that transit from one to another. These discrete modes are actually the Euler buckling mode as the compressive, force, $P(t)$, remains approximately constant and is equal to the eigenvalues of the Euler buckling problem (see fig 4.8(b)).

Interestingly, in this regime the dynamics is relatively slow with the system remaining for long periods in one mode before rapidly switching to another. Here we investigate this transition between discrete modes during the coarsening. In particular, we are interested in the time the system spends in each mode as well as the rapid transition to the next one.

The question is to analyse the (hydrodynamically) linear problem, namely (4.18)-(4.23), in situations where the boundary effects start to dominate. Here we note that because the compressive force, $P(t)$, depends on time, the standard method (separating variables and then solving a resulting Sturm-Liouville type problem) is not applicable. Instead, we decompose the vertical deflection, $u(x,t)$, in a basis of

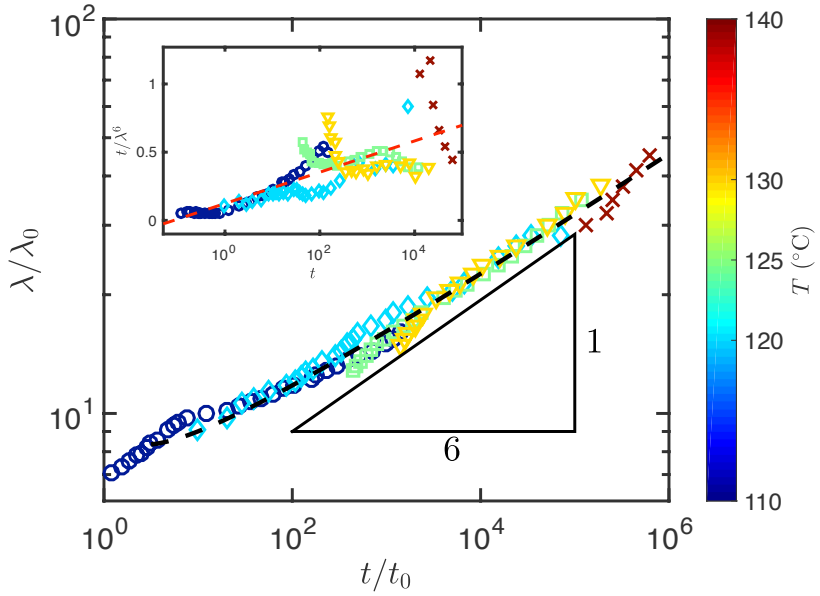

Figure 4.11: Comparison of previous experimental data (Vandeparre *et al.*, 2010) (points, courtesy of Pascal Damman) with the asymptotic prediction (4.73) (dashed curve). Inset: Compensated plot of t/λ^6 which increases as a function of time instead of being a constant, as predicted by the naive scaling. Our model suggests that $t/\lambda^6 \propto \log t/t_c$. We extract t_c as the value of the time t for which the best fit of t/λ^6 vanishes (red dashed line in the inset), giving $t_c = 0.0837$ s. In the main figure we non-dimensionalize time by $t_0 = t_c$ and lengths by $\lambda_0 = [Bh_0^3 t_0/(12\mu)]^{1/6} \approx 0.16$ μm where μ is used as a fitting parameter (within the limits given previously Plazek and Rourke (1971)). Experiments at different temperatures are signified by different colours (as in the colour bar), and also using symbols: $T = 110$°C (circles), $T = 120$°C (diamonds), $T = 125$°C (squares), $T = 130$°C (triangles) and $T = 140$°C (crosses). These results have been shifted to a single effective temperature of ≈ 120°C using the WLF time–temperature superposition. Reprinted figure with permission from O. Kodio *et al.* (2017). 'Lubricated wrinkles: Imposed constraints affect the dynamics of wrinkle coarsening'. *Physical Review Fluids* 2.1, p. 014202. DOI: `10.1103/PhysRevFluids.2.014202`. ©2017 Americal Physical Society.

the static solutions with time dependent coefficients. (We will assume this basis of static solutions to be complete.)

To start, we note that when $u(x,t) = u_e(x)$ does not evolve in time, the governing equations, (4.45)–(4.48), reduce to

$$\frac{\mathrm{d}^6 u_e}{\mathrm{d}x^6} + P_e \frac{\mathrm{d}^4 u_e}{\mathrm{d}x^4} = 0, \tag{4.77}$$

with boundary conditions:

$$u_e = \frac{\mathrm{d}^2 u_e}{\mathrm{d}x^2} = \frac{\mathrm{d}^4 u_e}{\mathrm{d}x^4} = 0 \tag{4.78}$$

at $x = \pm L$ and the constraint:

$$\frac{1}{2}\int_{-L}^{L}\left(\frac{\mathrm{d}u}{\mathrm{d}x}\right)^2 \mathrm{d}x = \Delta. \tag{4.79}$$

Now the general solution of (4.77) is given by:

$$u_e(x) = c_1 + c_2 x + c_3 x^2 + c_4 x^3 + c_5 \sin\sqrt{P_e}x + c_6 \cos\sqrt{P_e}x. \tag{4.80}$$

By imposing the boundary conditions, (4.78), we find a system of 6 homogeneous linear equations in the 6 unknowns, $(c_1 \cdots c_6)$, which has a non trivial solution if and only if the resulting determinant vanishes. Using standard techniques, we obtain that the static boundary value problem has a solution if

$$\cos(L\sqrt{P_e})\sin(L\sqrt{P_e}) = 0, \tag{4.81}$$

which is equivalent to $\sin(2L\sqrt{P_e}) = 0$ and shows that

$$L\sqrt{P_e} = n\pi/2, \text{ with } n \in \mathbb{N}. \tag{4.82}$$

By using (4.82), it is possible to show that $c_1 = c_2 = c_3 = c_4 = c_6 = 0$ when n is even, and $c_1 = c_2 = c_3 = c_4 = c_5 = 0$ when n is odd. Therefore the general solution to the static problem may be written

$$u_e(x) = a_n \sin\left(n\pi\tfrac{x}{L}\right) + a_{n-1/2}\cos\left[(n-\tfrac{1}{2})\pi\tfrac{x}{L}\right].$$

It is also interesting to note that the product, (4.81), vanishes when $\cos(L\sqrt{P_e}) = 0$ xor $\sin(L\sqrt{P_e}) = 0$ — the two factors in (4.81) cannot both vanish at the same time (hence the exclusive or). Hence, we find that if the sine term vanishes then the solution is even, otherwise it is odd. From this we anticipate that the system may alternate between an anti-symmetric mode (from the sine term), and a symmetric mode (the cosine). However, the system may also transit from one mode of a given symmetry to the next one of the same symmetry. For example, if the system evolves from an initial condition which is perfectly symmetric, *e.g.* a Gaussian, we might expect the system to select only symmetric modes.

Having identified the general solution to the static problem, we return to the dynamic problem, and write

$$u(x,t) = \sum_{n\geq 1} a_n(t)\sin\left(n\pi\tfrac{x}{L}\right) + a_{n-1/2}(t)\cos\left[(n-\tfrac{1}{2})\pi\tfrac{x}{L}\right]. \tag{4.83}$$

Substituting (4.83) into (4.77) and (4.79), and using the standard orthogonality properties of the cosine and sine, we obtain the governing equations for the amplitudes as:

$$\frac{\mathrm{d}a_n}{\mathrm{d}\bar{t}} = \left(-n^6 + \bar{P}n^4\right) a_n, \text{ for } n = 1, 2, 3, \cdots \tag{4.84}$$

$$\frac{\mathrm{d}a_{n-1/2}}{\mathrm{d}\bar{t}} = \left[-(n-\tfrac{1}{2})^6 + \bar{P}(n-\tfrac{1}{2})^4\right] a_{n-1/2}, \text{ for } n = 1, 2, 3, \cdots \tag{4.85}$$

where $\bar{t} = \left(\frac{\pi}{L}\right)^6 t$, $\bar{P} = PL^2/\pi^2$. These equations are to be solved subject to the constraint

$$\sum_{n\geq 1} n^2 a_n^2 + (n-\tfrac{1}{2})^2 a_{n-1/2}^2 = \bar{\Delta}, \tag{4.86}$$

where $\bar{\Delta} = L\Delta/\pi^2$.

To progress further, we consider the case in which $u(x,t)$ consists of two adjacent modes in the dynamics, of amplitude a_n and a_m, respectively. Here the next adjacent mode to n is either $m = n - \frac{1}{2}$ of amplitude $a_{n-1/2}$, or $m = n - 1$ of amplitude a_{n-1}. When the equations (4.45)–(4.48), are solved starting with a random noise as the initial condition, then both symmetric and anti-symmetric modes are equally present. In general the next lower adjacent mode to an n^{th} mode is the following anti-symmetric mode. Even with a symmetric initial condition, the system may transit, through some anti-symmetric modes, because the initial amplitude of the anti-symmetric modes might not be identically zero due to numerical noise, see fig 4.8(b).

Therefore, we consider the transitioning of an n^{th} to the following m^{th} mode. The governing equations for those adjacent modes are then:

$$\frac{\mathrm{d}a_n}{\mathrm{d}\bar{t}} = -n^6 a_n + \bar{P}n^4 a_n, \tag{4.87}$$

$$\frac{\mathrm{d}a_m}{\mathrm{d}\bar{t}} = -m^6 a_m + \bar{P}m^4 a_m, \tag{4.88}$$

$$n^2 a_n^2 + m^2 a_m^2 = \bar{\Delta}. \tag{4.89}$$

By taking the derivative of (4.89) and using, (4.87) and (4.88), it is possible to calculate the compressive force $\bar{P}$ as

$$\bar{P} = \frac{n^8 a_n^2 + m^8 a_m^2}{n^6 a_n^2 + m^6 a_m^2}. \tag{4.90}$$

Now we multiply (4.87) and (4.88) by a_n and a_m, respectively so that the resulting equations involve only the square amplitude of the modes, which we denote by $\mathrm{X} = a_n^2$ and $\mathrm{Y} = a_m^2$. We focus on X (since $\mathrm{Y} = (\bar{\Delta} - n^2\mathrm{X})/m^2$ from (4.89)), which satisfies:

$$1 = \frac{1}{2(m^2 - n^2)} \left[\frac{1}{n^4} \frac{1}{\mathrm{X}} \frac{\mathrm{dX}}{\mathrm{d}\bar{t}} + \frac{n^2}{m^6} \frac{1}{\bar{\Delta} - n^2\mathrm{X}(t)} \frac{\mathrm{dX}}{\mathrm{d}\bar{t}} \right]. \tag{4.91}$$

Eq. (4.91) can be immediately integrated, to give the time to transition from $\mathrm{X}(t_0)$ to $\mathrm{X}(\bar{t})$

$$\bar{t} - t_0 = \frac{1}{2(m^2 - n^2)} \left[\frac{1}{n^4} \log \left| \frac{\mathrm{X}(\bar{t})}{\mathrm{X}(t_0)} \right| - \frac{1}{m^4} \log \left| \frac{\bar{\Delta} - n^2\mathrm{X}(t)}{\bar{\Delta} - n^2\mathrm{X}(t_0)} \right| \right]. \tag{4.92}$$

This equation can be seen as an analytical solution of the amplitude, $a_n(t)$, for the n^{th} mode. Indeed when $\mathrm{X}(t_0) \neq 0$, the Implicit Function Theorem guarantees that we can always infer $\mathrm{X}(\bar{t})$ from (4.92) for any finite time. Here (4.92) can be simplified further as:

$$\mathrm{X}(\bar{t}) = \mathrm{X}(t_0) \left[\frac{\bar{\Delta} - n^2\mathrm{X}(\bar{t})}{\bar{\Delta} - n^2\mathrm{X}(t_0)} \right]^{\left(\frac{n}{m}\right)^4} \exp\left[2(m^2 - n^2)n^4(\bar{t} - t_0) \right]. \tag{4.93}$$

To check the evolution of the analytical solution for the amplitude we solve numerically, the equations (4.87)–(4.90); this shows a very good agreement (see fig. 4.13). Here the equations are solved starting from $t_0 = 0$, with $\bar{\Delta} = 1$, $\mathrm{X}(t_0) = (\bar{\Delta} - \epsilon)/n^2$, $\epsilon = 10^{-10}$, $n = 1$.

We estimate the time over which most of the energy has been transferred from the higher mode to the lower, as follows. First, we notice that when there is only the highest mode present in the dynamics then its amplitude must satisfy $n^2\mathrm{X} = \bar{\Delta}$ from (4.89). We therefore choose, $n^2\mathrm{X}(t_0) = \bar{\Delta} - \epsilon$. In this way, ϵ represents the contribution coming from the remaining modes. The time taken for a particular mode to transition from an amplitude $\mathrm{X}(t_0) = (\bar{\Delta} - \epsilon)/n^2$ to an amplitude $\mathrm{X}(\bar{t}_{\mathrm{c}}) = \epsilon/n^2$ is given by

$$\bar{t}_c - t_0 = \frac{1}{2n - \frac{1}{2}} \left[\frac{1}{n^4} + \frac{1}{(n - \frac{1}{2})^4} \right] \log\left(\frac{\bar{\Delta} - \epsilon}{\epsilon} \right). \tag{4.94}$$

Here $\bar{t}_c$ is analogous to a correlation time, as it is the time over which the presence of the n^{th} mode will be felt during the dynamics.

With the parameters in fig. 4.13, this correlation time is $\bar{t}_c = 260.9596$.

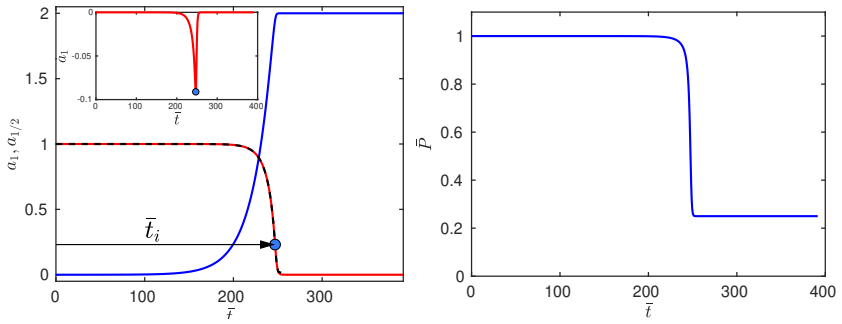

Figure 4.12: Evolution of two adjacent Euler buckling modes, as a function of time. Left: Here the amplitude of the anti-symmetric mode a_1, (solid blue) decreases as the amplitude of the lowest symmetric mode, $a_{1/2}$, (solid red) starts to grow. This illustrates the transfer of energy from the higher mode to the lower mode. The dashed black curve corresponds to the analytical solution (4.92). The dot corresponds to the inflection point calculated from the analytical solution (4.97). Inset: The derivative of a_1 showing the inflection. Right: Evolution of the compressive force, $P(\bar{t})$ as a function of time. Here, the compressive force decreases from $P(\bar{t}) = 1$ for a_1, to $P(\bar{t}) = 1/4$ for $a_{1/2}$. The solid lines correspond to the numerical solution of (4.87)–(4.90) for the following parameters: $t_0 = 0$, $\bar{\Delta} = 1$, $a_1(t_0) = \sqrt{(\bar{\Delta} - \epsilon)/n^2}$, with $\epsilon = 10^{-10}$, $n = 1$ and $m = \frac{1}{2}$.

However, we see that this definition of the correlation time is weakly sensitive to the initial size of the next mode, ϵ, via a $\log \epsilon$ term. A better definition of this correlation time is to choose the inflection point $t = t_i$, where $a_n(\bar{t})$ changes its concavity, this condition is given by $\ddot{a}_n(t_i) = 0$ or

$$\dot{\mathrm{X}}^2(\bar{t}_i) = 2\mathrm{X}(\bar{t}_i)\ddot{\mathrm{X}}(\bar{t}_i). \tag{4.95}$$

Solving (4.95) using the analytical solution of (4.92) gives the inflection point $\mathrm{X}(\bar{t}_i)$ as

$$\mathrm{X}(\bar{t}_i) = \frac{\bar{\Delta}}{n^2} \frac{2m^4 + n^4 - \sqrt{n^8 + 8n^4m^4}}{2(m^4 - n^4)}. \tag{4.96}$$

Now, using (4.96) in (4.92), we obtain the corresponding inflection time, $\bar{t}_i$ as

$$\bar{t}_i = \frac{1}{2(m^2 - n^2)} \left[\frac{1}{n^4} \log \left| \frac{2m^4 + n^4 - \sqrt{n^8 + 8n^4m^4}}{2(m^4 - n^4)} \right| - \frac{1}{m^4} \log \left| \frac{3n^4 - \sqrt{n^8 + 8n^4m^4}}{2(m^4 - n^4)} \right| \right]. \tag{4.97}$$

This inflection time provides a good account of the period over which a given mode will be present during the dynamics, see fig. 4.12.

As an extension of this idea, one may allow a large number of modes together with a set of amplitudes $a_n(\bar{t})$ such $a_N(t_0) = \sqrt{1 - \varepsilon}/N$ and $a_n(t_0) = \sqrt{\varepsilon}/n$ for

$n = 1...N-1$. This is more complicated and so can only be solved numerically. The numerical solution generates a compelling cascade of the compressive force as a function of time, as shown in fig. 4.14 for $N = 100$ anti-symmetric modes.

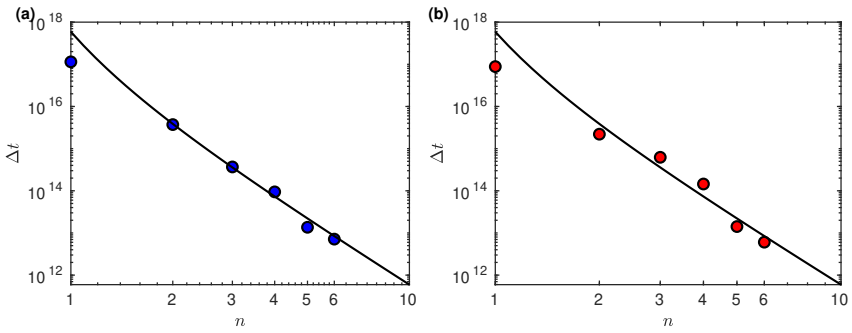

Figure 4.13: Transition time between modes as a function of the mode number n for the linear(a) and nonlinear (b) cases. The black solid curve is the prediction from modal decomposition eq. (4.94). The dots are the results from numerical solution of the full problem (4.13) -(4.17). In these simulations $L = 10^3$, $N = 512$ grid points. The initial condition $u(x, 0)$ is drawn randomly from a uniform distribution on $[-\varepsilon, \varepsilon]$ with $\varepsilon = 10^{-3}$; the same random noise is used in both (a) and (b).

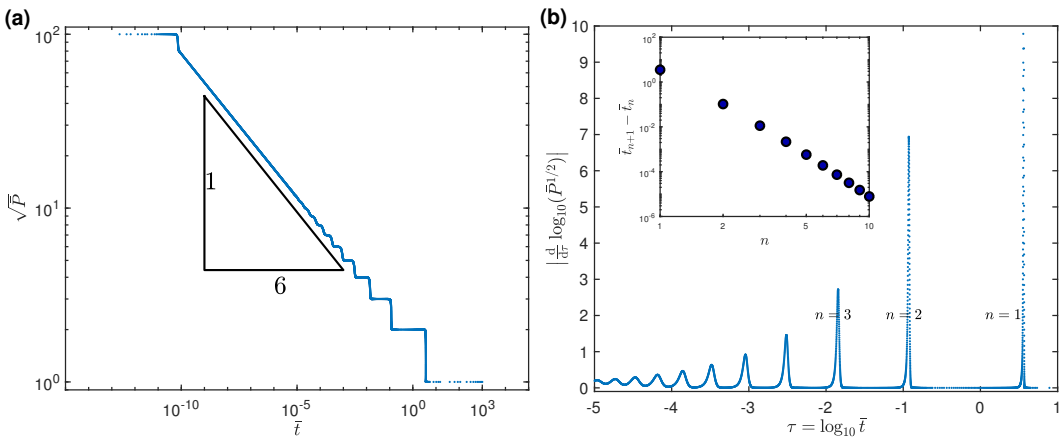

Figure 4.14: (a) Cascade of the compressive force for $N = 100$ modes obtained by numerically solving (4.84)–(4.86) with $n = 1, 2, \cdots N = 100$. (b) Illustration of the cascade time scale: The peaks represents each jump of the compressive force. Inset: time taken to transition between two consecutive antisymmetric modes, $n + 1 \to n$.

4.11 Conclusion

We have studied in detail the coarsening of wrinkles in a thin inextensible elastic beam sitting on a thin viscous layer and subject to a constant imposed end-shortening.

Using a combination of numerical and asymptotic techniques we have shown that the nonlinear constraint of a fixed end–end compression modifies the behaviour of the system in important ways. Rather than a horizontal length scale $\propto t^{1/6}$, as has been frequently observed in analogous, unconstrained problems, (Huang and Im, 2006; Tulchinsky and Gat, 2016), we observe that the appropriate length scale $\propto (t/\log t)^{1/6}$. This logarithmic correction means that the evolution is no longer self-similar, though we are able to express the evolution of the beam profile in a form that is close to self-similar in the long-time limit. This logarithmic correction results from the asymptotic evaluation of the constraint integral (see (4.58)) and so, to our knowledge, cannot be rationalized by means of a simple scaling argument. Nevertheless, we suggest that previous experimental measurements of an effective wavelength in fact show a discrepancy with the expected $t^{1/6}$ behaviour that is consistent with our prediction of $(t/\log t)^{1/6}$ behaviour. As a result, even though logarithmic corrections are often ignored, they may be especially noticeable on the intermediate time scales of evolution that are accessible experimentally. Finally, we have shown as the mean wrinkle wavelength reaches the system size, the coarsening proceeds via a slow relaxation interspaced with rapid transitions between modes.

4.A The breakdown of similarity solutions

From the simple scaling law presented previously (Vandeparre *et al.*, 2010) it is natural to assume that the partial differential equation (4.45) subject to the constraint (4.48) should have a similarity solution in which $x \sim t^{1/6}$, $u \sim t^{1/12}$, and $P \sim t^{-1/3}$. This expectation is further reinforced by the calculation of such similarity solutions for the unconstrained problem (Tulchinsky and Gat, 2016). However, we see from the asymptotic solution (4.70) that the true long-time solution for $u(x,t)$ cannot be expressed in similarity form. For another perspective on why this approach does not work for the constrained problem considered here, we follow the approach of Budd and Peletier (2000) in a related problem and make the similarity ansatz

$$\eta = x/t^{1/6}, \quad u(x,t) = t^{1/12} f(\eta), \quad P = t^{-1/3} Q. \tag{4.98}$$

Substituting this into (4.48), we find that the governing partial differential equation becomes

$$\frac{\mathrm{d}^6 f}{\mathrm{d}\eta^6} + Q\frac{\mathrm{d}^4 f}{\mathrm{d}\eta^4} = \frac{1}{12} f - \frac{1}{6}\eta\frac{\mathrm{d}f}{\mathrm{d}\eta}, \tag{4.99}$$

which is to be solved with the integral constraint

$$\frac{1}{2}\int_{-\infty}^{\infty}(f')^2\,\mathrm{d}\eta = \Delta. \tag{4.100}$$

To see why the constraint (4.100) is incompatible with the similarity problem (4.99), we examine the behaviour of $f(\eta)$ as $\eta \to \infty$. This is most readily done by examining the $\omega \to 0$ limit of the Fourier Transform of $f(\eta)$, denoted $\hat{f}(\omega)$; we find that $\hat{f}(\omega) \propto \omega^{-3/2}$ as $\omega \to 0$. However, in Fourier space, the constraint (4.100) reads

$$\tfrac{1}{2}\int_{-\infty}^{\infty}\omega^2\hat{f}^2\,\mathrm{d}\omega = \Delta. \tag{4.101}$$

Since $\hat{f}(\omega) \propto \omega^{-3/2}$ as $\omega \to 0$, the integral on the LHS of (4.101) does not converge; we conclude that the solution of the similarity equation (4.99) is not sufficiently well behaved as $\eta \to \pm\infty$ (corresponding to $\omega \to 0$) for the integral on the LHS of (4.100) to converge.

4.B Generalization of the asymptotic analysis

The technique used to find the late-time profile in §4.7 may readily be applied to a larger class of partial differential equations (PDEs) with a global algebraic constraint of the same form. We therefore consider the PDE

$$\frac{\partial u}{\partial t} = (-1)^{n+1}\left(\frac{\partial^{2n}u}{\partial x^{2n}} + P(t)\frac{\partial^{2n-2}u}{\partial x^{2n-2}}\right), \tag{4.102}$$

$$\tag{4.103}$$

subject to the constraint

$$\frac{1}{2}\int_{-\infty}^{+\infty}\left(\frac{\partial u}{\partial x}\right)^2\mathrm{d}x = \Delta(t). \tag{4.104}$$

In (4.102), $n \geq 2$ is an integer. This problem encompasses different limits of physical interest including a beam embedded in a viscous fluid, $n = 2$, (Biot, 1957; Budd and Peletier, 2000), and a beam above a lubricated layer, $n = 3$, which we considered in §4.7.

Repeating the analysis of §4.7, we find that the time behaviour of the compressive force $P(t)$ is given by the relation

$$P(t) \sim \frac{n-1}{n}\left[\frac{1}{\beta_n}\left(\log\Delta + \frac{3\log t}{2n}\right)\frac{1}{t}\right]^{1/n}, \tag{4.105}$$

where $\beta_n = 2\frac{1}{n}(\frac{n-1}{n})^{(n-1)}$.

Likewise the late time profile may be computed using the same standard application of Laplace's method to be

$$u(x,t) \sim 2P^{1/2} \mathrm{e}^{\frac{\sigma}{n-1}} \sqrt{\frac{\pi}{2\sigma n}} \mathrm{e}^{-Px^2/(8\sigma n)} \cos(\sqrt{P}x), \tag{4.106}$$

where $\sigma = \frac{1}{2}(n-1)(\log \Delta + \frac{3\log t}{2n})$. We therefore see that the profile is approximately self similar, up to a logarithmic correction with an apparent wavelength given by:

$$\bar{\lambda}_n(t) \sim 2\pi \left(\frac{n}{n-1}\right)^{1/2} \left(\beta_n \frac{2n}{3} \frac{t}{\log t}\right)^{1/(2n)}. \tag{4.107}$$

The relation (4.107) suggests that the logarithmic correction to the wavelength is a generic signature of the global constraint (4.104) for all PDEs of the form (4.102).

Chapter 5

Conclusion

5.1 Summary of the thesis

In this thesis we have studied how dynamic buckling affects the spontaneous pattern selection in a number of model problems. These model problems have different geometries and involve different material constitutive relations. Nevertheless from the detailed study of these examples, a number of common themes has emerged. The main contributions of this thesis are summarized as follows:

5.1.1 Effect of curvature:

Dynamic buckling in circular geometries with an external pressure can be understood relatively easily by using results derived for a one-dimensional beam scenario; the leading-order effect of the ring curvature is to translate a normal pressure difference into a tangential compression (via Laplace's law). The results that are derived from these simple arguments can be observed in detailed numerical simulations, and are recovered from more detailed linear stability analyses in the limit of large instability mode number.

5.1.2 Effect of inertia

We have shown that a thin ring made of either a viscous liquid or an elastic solid buckles dynamically when subject to a sudden applied pressure, p. In the case of a viscous ring the dynamically selected mode number, n, is found to grow as $n \sim P^{1/6}$ while in the case of an elastic ring this behaviour is instead $n \sim P^{1/2}$. (Here, P is a dimensionless pressure whose definition depends on the problem studied; in each case $P \propto p$). We found that, for an elastic ring subject to an instantaneous loading, inertia is required to select non trivial modes (*i.e.* modes others than $n =$

2). Surprisingly, however, the mode selected is independent of the ring inertia (in particular its density). We have explained this apparent paradox by comparing the time scale of ramping of the pressure to the time scale of the fastest growing mode in the simpler case of an elastic beam. This allowed us to show that loading too slowly induces selection of lower mode numbers.

In contrast to the case of an elastic ring suddenly subjected to a pressure (where the selected mode is independent of inertia) we found that, for a viscous ring, inertia is important: the selected mode *does* depend on the density of the liquid. Mathematically, this is because there is an additional time derivative in the constitutive equation of a liquid compared to that of an elastic. So inertia does not uniquely set a time scale.

For an elastic ring, we have computed analytically the time evolution of the post-buckled shape of the profile through with a weakly nonlinear analysis. This allowed us to find an expression for the evolution of the enclosed area, which compares well with both numerical and experimental data. At later stages, buckles merge — the wrinkle pattern coarsens. To understand this coarsening we turned to a viscous setting (leading to a lower differential index).

5.1.3 Coarsening:

By considering the model problem of a beam on a lubricated layer, we have explained how wrinkle coarsening can occur as the result of wave dispersion. To quantify coarsening, we presented an asymptotic analysis of how wrinkle coarsening occurs. Through this calculation, we have precisely found how the profile and the wavelength behave at late time when a confinement is imposed. The effect of confinement is to slow down the coarsening and we show that the dominant wavelength, λ, grows according to $\lambda \propto (t/\log t)^{1/6}$. Here the inextensibility of the elastic beam yields an integral constraint that leads to a logarithmic correction that can be important in experimental observations of coarsening[1]. Furthermore, our numerical solutions revealed a new regime as the wavelength of wrinkles, λ, becomes comparable to the size of the system L. Interestingly, in this regime the dynamics is relatively slow with the system remaining for long periods with one particular mode before rapidly switching to another.

[1]We have also generalized the analysis to certain classes of constrained PDE and have found that the late time behaviour for the compressive force and the profile, and in these cases too, the logarithmic correction persists see §4.B

5.2 Discussion and future work

The research performed in this thesis, and the analytical methods devised to gain insights on the resulting formed pattern, may be useful in the broader scientific context. Indeed we discuss below three broader questions that may be tackled with the sorts of methods developed in this thesis.

• **Topological defects:** Recently, it has been drawn to our attention that the effect of the rate of ramping on pattern selection in dynamic buckling may be analogous to problems in other branches of physics. Moreover, the analysis of §4.B may be useful in the study of non-equilibrium phase transitions and the emergence of topological defects (Stoop *et al.*, 2015). In this case, our compressive force, $P(t)$ can play the role of a different physical control parameter. More precisely the idea is to introduce a *generalized Swift-Hohenberg* (Cross and Hohenberg, 1993) equation such as

$$\frac{\partial u}{\partial t} = \alpha(t)u + \beta(t)\frac{\partial^2 u}{\partial x^2} + \gamma(t)\frac{\partial^4 u}{\partial x^4} + \delta(t)\frac{\partial^6 u}{\partial x^6} + \cdots , \tag{5.1}$$

with α, β, γ, δ all functions of time (in principle).

The question is then to understand how the overall pattern formed depends on the temporal dependence of the coefficients. Indeed, this may potentially provide some insight into seemingly different physical phenomena. For example, $\alpha(t)$ can be thought of as a time-dependent Winkler foundation and $\beta(t)$ as a quenching temperature.

• **Inertial wrinkling:** A thin floating elastic sheet wrinkles dynamically when impacted by small sphere (Box *et al.*, 2019). Crucially, the wrinkles coarsen with time (and more rapidly than in the viscous case of chapter 4 — here the typical wavelength doubles in a fraction of second). A simple scaling for this problem, suggests the wavelength increases as function of time as $\lambda \sim t^{2/5}$. While this result is consistent with experiments (Box *et al.*, 2019), more detailed numerics (O'Kiely *et al.*, 2020) suggest a correction of this scaling. While this correction is not understood, it might suggests be possible to infer the asymptotic behaviour of the dominant wavelength and the leading-order correction due to the global inextensibility constraint. A preliminary heuristic calculations suggest the dominant wavelength to grow as

$$k_{\mathrm{dom}} \sim \left(\frac{3}{4\sqrt{6}}\frac{\log t}{t}\right)^{2/5} . \tag{5.2}$$

This results seems to capture the late time behaviour of the observed wavelength. Similar calculations along the lines of §4.B may be used to control the imposed constraint as a route for tuning the selected dominant wavelength.

• **Spatial coarsening in wrinkles** We think that our approach of §4.B might yield new insights into the generic features of wrinkled solutions of the Föppl-von Karman equation in the large-strip limit (Love, 1959). Many experiments have shown that wrinkles may split via a cascade as a boundary is approached (Davidovitch, 2009). For example, wrinkling in a curtain. Depending on the sign of the applied longitudinal tension, the Föppl von Karman equation for the curtain changes its nature from hyperbolic to elliptic. It is not surprising that the different analytical and numerical methods used in this thesis may readily be applicable to hyperbolic-type equations too. To describe the coarsening of the wrinkled solution, we propose to deal with this as follow: instead of naively treating one of the spatial co-ordinates as time, we perform the following transformation (analogous to Wick rotation) where replace the spatial co-ordinate along which coarsening happens, by an imaginary time. A preliminary calculation along these lines gives the dominant wavelength as

$$k_{\mathrm{dom}}(y) \sim \frac{1}{2}\left(\frac{\log y}{y}\right)^{1/2}, \tag{5.3}$$

which adds a logarithmic correction to the accepted scaling of Vandeparre *et al.* (2011).

Bibliography

Ablowitz, M. J. (2003). *Complex Variables*. Cambridge University Press.

Antman, S. S. (2005). *Nonlinear Problems of Elasticity*. Springer.

Arutkin, M., Ledesma-Alonso, R., Salez, T. and Raphaël, E. (2016). 'Elastohydrodynamic wake and wave resistance'. *Preprint*, pp. 1–14. arXiv: 1607.07816.

Audoly, B. and Pomeau, Y. (2010). *Elasticity and Geometry, From Hair Curls to the Non-linear Response of Sheels*. Oxford: Oxford University Press.

Bender, C. M. and Orsag, S. A. (1999). *Advanced Mathematical Methods for Scientists and Engineers, Asymptotic Methods and Peturbation Theory*. Springer.

Bertozzi, A. L. (1996). 'Symmetric singularity formation in lubrication-type equations for interface motion'. *SIAM Journal on Applied Mathematics* 56.3, pp. 681–714.

Biot, M. A. (1957). 'Folding instability of a layered viscoelastic medium under compression'. *Proceedings of the Royal Society London. Series A, Mathematical and Physical Sciences*.

Biot, M. A. (1965). *Mechanics of incremental deformation*. Vol. 32. 4. Wiley.

Box, F., Kodio, O., O'Kiely, D., Cantelli, V., Goriely, A. and Vella, D. (2020). 'Dynamic Buckling of an Elastic Ring in a Soap Film'. *Physical Review Letters* 124.19. DOI: 10.1103/physrevlett.124.198003.

Box, F., O'Kiely, D., Kodio, O., Inizan, M., Castrejón-Pita, A. A. and Vella, D. (2019). 'Dynamics of wrinkling in ultrathin elastic sheets'. *Proceedings of the National Academy of Sciences* 116.42.

Brau, F., Damman, P., Diamant, H. and Witten, T. A. (2013). 'Wrinkle to fold transition: influence of the substrate response'. *Soft Matter* 9.34, p. 8177. DOI: 10.1039/c3sm50655j.

Buckmaster, J. D., Nachman, A. and Ting, L. (1975). 'The buckling and stretching of a viscida'. *Journal of Fluid Mechanics* 31.2, pp. 157–168. DOI: 10.1093/qjmam/31.2.157.

Budd, C. J. and Peletier, M. A. (2000). 'Approximate Self-Similarity in Models of Geological Folding'. *SIAM Journal on Applied Mathematics* 60.3.

Burchard, A. and Thomas, L. E. (2003). 'On the Cauchy problem for a dynamical Euler's elastica'. *Communications in Partial Differential Equations* 28.1-2, pp. 271–300.

Carleman, T. (1944). *L'Intégrale de Fourier et questions qui s'y rattachent*. Uppsala, Sweden: Almqvist Wiksells.

Carlson, A. and Mahadevan, L. (2015). 'Similarity and singularity in adhesive elastohydrodynamic touchdown'. *Physics of fluids* 28.1, pp. 1–6. DOI: 10.1063/1.4938115. arXiv: 1507.03912.

Chen, J. S. and Tsao, H. W. (2014). 'Dynamic snapping of a hinged extensible elastica under a step load'. *International Journal of Non-Linear Mechanics* 59.

Chen, Y. C. and Fried, E. (2014). 'Stability and bifurcation of a soap film spanning a flexible loop'. *Journal of Elasticity* 116.1. DOI: 10.1007/s10659-013-9458-x.

Chung, T. J. (2002). *Computational Fluid Dynamics*. Cambridge University Press.

Cross, M. C. and Hohenberg, P. C. (1993). 'Pattern formation outside of equilibrium'. *Reviews of Modern Physics* 65.3.

Davidovitch, B. (2009). 'Period fissioning and other instabilities of stressed elastic membranes'. *Physical Review E - Statistical, Nonlinear, and Soft Matter Physics* 80.2, pp. 1–4. DOI: 10.1103/PhysRevE.80.025202. arXiv: 0901.2719v1.

Euler, L. (1744). 'De Curvis Elasticis, Additamentum Methodus Inveniendi Lienas Curvas Maximi Minimive Proprietate Gaudentes'. *(See the English translation by Oldfather et al. entitled "Leonhard Euler's Elastic Curves" in Chicago Journals)*.

Flaherty, J. E., Keller, J. B. and Rubinow, S. I. (1972). 'Post Buckling Behavior of Elastic Tubes and Rings with Opposite Sides in Contact'. *SIAM Journal on Applied Mathematics* 23.4, pp. 446–455. DOI: 10.1137/0123047.

Flitton, J. C. and King, J. R. (2004). 'Moving-boundary and fixed-domain problems for a sixth-order thin-film equation'. *European Journal of Applied Mathematics* 15.6, pp. 713–754. DOI: 10.1017/S0956792504005753.

Gauthier, L. (1969). 'Sur le flambement et les questions d'instabilité'. *Applied Mechanics, Proceedings of the Twelfth International Congress of Applied Mechanics, Stanford University, August 26–31, 1968*. Ed. by M. Hetényi and W. G. Vincenti. Springer-Verlag Berlin Heidelberg, pp. 13–42. DOI: 10.1007/978-3-642-85640-2_2.

Giomi, L. and Mahadevan, L. (2012). 'Minimal surfaces bounded by elastic lines'. *Proceedings of the royal society A* 468. DOI: 10.1098/rspa.2011.0627.

Gladden, J. R., Handzy, N. Z., Belmonte, A. and Villermaux, E. (2005). 'Dynamic Buckling and Fragmentation in Brittle Rods'. *Physical Review Letters* 94. DOI: 10.1103/PhysRevLett.94.035503.

Goriely, A., Nizette, M. and Tabor, M. (2001). 'On the dynamics of elastic strips'. *Journal of Nonlinear Science* 11.1. DOI: 10.1007/s003320010009.

Goriely, A. (2017). *The Mathematics and Mechanics of Biological Growth*. Springer.

Griffiths, I. M. (2007). 'Mathematical Modelling of Non-axisymmetric Glass Tube Manufacture'. PhD thesis. University of Oxford.

Griffiths, I. M. and Howell, P. D. (2009). 'The Surface-Tension-Driven Retraction of a Viscida'. *SIAM Journal on Applied Mathematics* 70.5, pp. 1453–1487. DOI: 10.1137/090746318.

Hoppe, R. (1871). 'Vibrationen eines Ringes in seiner Ebene.' *Journal fur die Reine und Angewandte Mathematik* 1871.73, pp. 158–170. DOI: 10.1515/crll.1871.73.158.

Howell, P. D. (1994). 'Extensional thin layer flows'. PhD thesis. University of Oxford.

Howell, P., Kozyreff, G. and Ockendon, J. (2009). *Applied solid mechanics*. Cambridge University Press. DOI: 10.1007/978-1-4419-7646-8.

Huang, R. and Im, S. H. (2006). 'Dynamics of wrinkle growth and coarsening in stressed thin films'. *Physical Review E - Statistical, Nonlinear, and Soft Matter Physics* 74.2. DOI: 10.1103/PhysRevE.74.026214.

Huang, R. and Suo, Z. (2002). 'Wrinkling of a compressed elastic film on a viscous layer'. *Journal of Applied Physics* 91.3, p. 1135. DOI: 10.1063/1.1427407.

Im, S. H. and Huang, R. (2005). 'Evolution of Wrinkles in Elastic-Viscoelastic Bilayer Thin Films'. *Transaction of the AMSE* 72. DOI: 10.1115/1.2043191.

Karagiozova, D. and Alves, M. (2008). 'Dynamic elastic-plastic buckling of structural elements: A review'. *Applied Mechanics Reviews* 61. DOI: 10.1115/1.2939481.

Kodio, O., Goriely, A. and Vella, D. (2020). 'Dynamic buckling of an inextensible elastic ring: Linear and nonlinear analyses'. *Physical Review E* 101.5. DOI: 10.1103/physreve.101.053002.

Kodio, O., Griffiths, I. M. and Vella, D. (2017). 'Lubricated wrinkles: Imposed constraints affect the dynamics of wrinkle coarsening'. *Physical Review Fluids* 2.1, p. 014202. DOI: 10.1103/PhysRevFluids.2.014202.

Landau, L. D. and Lifshitz, E. M. (1970). *Course of Theoretical Physics Volume 7: Theory of Elasticity*. 2nd ed. Vol. 7. Oxford: Pergamon Press, p. 44.

Lange, C. and Newell, A. (1971). 'The post-buckling problem for thin elastic shells'. *SIAM Journal on Applied Mathematics* 21.4.

Le Merrer, M., Quéré, D. and Clanet, C. (2012). 'Buckling of viscous filaments of a fluid under compression stresses'. *Physical Review Letters* 109.6. DOI: 10.1103/PhysRevLett.109.064502.

Leal, L. (2007). *Advanced transport phenomena: fluid mechanics and convective transport processes*. Cambridge University Press.

Leocmach, M., Nespoulous, M., Manneville, S. and Gibaud, T. (2015). 'Hierarchical wrinkling in a confined permeable biogel'. *Science Advances* 1.9. DOI: 10.1126/sciadv.1500608.

Lindberg, H. (2003). 'Little Book of Dynamic Buckling'. *LCE Science/Software, Penn Valley CA* September.

Love, A. (1959). *A Treatise On the Mathematical Theory of Elasticity*. 4th ed. Cambridge University Press.

Marston, J. O., Mansoor, M. M., Truscott, T. T. and Thoroddsen, S. T. (2015). 'Buckling instability of crown sealing'. *Physics of Fluids* 27.9. DOI: 10.1063/1.4931097.

Marston, J. O., Truscott, T. T., Speirs, N. B., Mansoor, M. M. and Thoroddsen, S. T. (2016). 'Crown sealing and buckling instability during water entry of spheres'. *Journal of Fluid Mechanics* 794. DOI: 10.1017/jfm.2016.165.

Maxwell, J. C. (1899). *Theory of heat*. New York and Bombay: Longmans, Green, and co.

Mumford, D. (1994). 'Elastica and Computer Vision'. *Algebraic geometry and its applications*.

Neukirch, S., Frelat, J., Goriely, A. and Maurini, C. (2012). 'Vibrations of post-buckled rods: The singular inextensible limit'. *Journal of Sound and Vibration* 331.3, pp. 704–720. DOI: 10.1016/j.jsv.2011.09.021.

O'Kiely, D. (2017). 'Mathematical models for the glass sheet redraw process'. PhD thesis.

O'Kiely, D., Box, F., Kodio, O., Whiteley, J. and Vella, D. (2020). 'Impact on floating thin elastic sheets: A mathematical model'. *Physical Review Fluids* 5.1. DOI: 10.1103/PhysRevFluids.5.014003.

Pandey, A., Moulton, D. E., Vella, D. and Holmes, D. P. (2014). 'Dynamics of snapping beams and jumping poppers'. *EPL (Europhysics Letters)* 105.2. DOI: 10.1209/0295-5075/105/24001. arXiv: 1310.3703v1.

Peschka, D., Münch, A. and Niethammer, B. (2010). 'Thin-film rupture for large slip'. *Journal of Engineering Mathematics* 66.1, pp. 33–51. DOI: 10.1007/s10665-009-9342-7.

Plazek, D. and Rourke, O. (1971). 'Viscoelastic Behavior of Low Molecular Weight Polystyrene'. *Journal of Polymer Science: Part A-2* 9. DOI: 10.1002/pol.1971.160090202.

Reis, P. M. (2015). 'A Perspective on the Revival of Structural (In) Stability With Novel Opportunities for Function: From Buckliphobia to Buckliphilia'. *Journal of Applied Mechanics* 82.11. DOI: 10.1115/1.4031456.

Roman, B., Gay, C. and Clanet, C. (2004). 'Pendulum , Drops and Rods : a physical analogy'. *Preprint*.

Santillan, S. T. (2007). 'Analysis of the Elastica With Applications To Vibration Isolation'. PhD thesis. Duke University.

Silveira, R. da, Chaieb, S. and Mahadevan, L. (2000). 'Rippling Instability of a Collapsing Bubble'. *Science* 287. DOI: 10.1126/science.287.5457.1468.

Singh, H. and Hanna, J. A. (2019). 'On the Planar Elastica, Stress, and Material Stress'. *Journal of Elasticity* 136.1, pp. 87–101. DOI: 10.1007/s10659-018-9690-5. arXiv: 1706.03047.

Singh, K., Lister, J. R. and Vella, D. (2013). 'A fluid-mechanical model of elastocapillary coalescence'. *Journal of Fluid Mechanics* 745. DOI: 10.1017/jfm.2014.102. arXiv: 1310.4530v2.

Slim, A. C., Teichman, J. and Mahadevan, L. (2012). 'Buckling of a thin-layer Couette flow'. *Journal of Fluid Mechanics* 694. DOI: 10.1017/jfm.2011.437.

Stafford, C. M., Harrison, C., Beers, K. L., Karim, A., Amis, E. J., VanLandingham, M. R., Kim, H. C., Volksen, W., Miller, R. D. and Simonyi, E. E. (2004). 'A buckling-based metrology for measuring the elastic moduli of polymeric thin films'. *Nature Materials* 3.8. DOI: 10.1038/nmat1175.

Stoop, N., Lagrange, R., Terwagne, D., Reis, P. M. and Dunkel, J. (2015). 'Curvature-induced symmetry breaking determines elastic surface patterns'. *Nature Materials* 14.3. DOI: 10.1038/nmat4202.

Tadjbakhsh, I. and Odeh, F. (1967). 'Equilibrium states of elastic rings'. *Journal of Mathematical Analysis and Applications* 18. DOI: 10.1016/0022-247X(67)90182-5.

Taylor, G. I. (1969). 'Instability of jets, threads, and sheets of viscous fluid'. *Applied Mechanics, Proceedings of the Twelfth International Congress of Applied Mechanics, Stanford University, August 26–31, 1968*. Ed. by M. Hetényi and W. G. Vincenti. Springer-Verlag Berlin Heidelberg, pp. 382–388. DOI: 10.1007/978-3-642-85640-2_30.

Teichman, J. A. (2002). 'Wrinkling and sagging of viscous sheets'. PhD thesis. MIT.

Tulchinsky, A. and Gat, A. D. (2016). 'Transient dynamics of an elastic Hele-Shaw cell due to external forces with application to impact mitigation'. *Journal of Fluid Mechanics* 800, pp. 517–530. DOI: 10.1017/jfm.2016.418.

Vandeparre, H., Gabriele, S., Brau, F., Gay, C., Parker, K. K. and Damman, P. (2010). 'Hierarchical wrinkling patterns'. *Soft Matter* 6.22. DOI: 10.1039/c0sm00394h.

Vandeparre, H., Piñeirua, M., Brau, F., Roman, B., Bico, J., Gay, C., Bao, W., Lau, C. N., Reis, P. M. and Damman, P. (2011). 'Wrinkling hierarchy in constrained thin sheets from suspended graphene to curtains'. *Physical Review Letters* 106.22. DOI: 10.1103/PhysRevLett.106.224301.

Vella, D., Ajdari, A., Vaziri, A. and Boudaoud, A. (2011). 'Wrinkling of pressurized elastic shells'. *Physical Review Letters* 107.17. DOI: 10.1103/PhysRevLett.107.174301.

Wah, T. (1970). 'Dynamic buckling of thin circular rings'. *International Journal of Mechanical Sciences* 12.2. DOI: 10.1016/0020-7403(70)90014-7.

Wouwer, A. V., Saucez, P. and Vilas, C. (2014). *Simulation of ODE/PDE models with MATLAB, OCTAVE and SCILAB: Scientific and engineering applications*. Springer. DOI: 10.1007/978-3-319-06790-2.